SAND REPORT

SAND2001-2959
Unlimited Release
Printed September 2001

Advanced Signal Processing for Thermal Flaw Detection

Michael T. Valley, Bruce D. Hansche, Thomas L. Paez, Angel Urbina,
D. Michael Ashbaugh

Prepared by
Sandia National Laboratories
Albuquerque, New Mexico 87185 and Livermore, California 94550

Sandia is a multiprogram laboratory operated by Sandia Corporation,
a Lockheed Martin Company, for the United States Department of
Energy under Contract DE-AC04-94AL85000.

Issued by Sandia National Laboratories, operated for the United States Department of Energy by Sandia Corporation.

Available to DOE and DOE contractors from
U.S. Department of Energy
Office of Scientific and Technical Information
P.O. Box 62
Oak Ridge, TN 37831

Telephone: (865)576-8401
Facsimile: (865)576-5728
E-Mail: reports@adonis.osti.gov
Online ordering: http://www.doe.gov/bridge

Available to the public from
U.S. Department of Commerce
National Technical Information Service
5285 Port Royal Rd
Springfield, VA 22161

Telephone: (800)553-6847
Facsimile: (703)605-6900
E-Mail: orders@ntis.fedworld.gov
Online order: http://www.ntis.gov/ordering.htm

SAND2001 – 2959
Unlimited Release
Printed September 2001

Advanced Signal Processing for Thermal Flaw Detection

Michael T. Valley, Bruce D. Hansche
Advanced Diagnostics and Production Testing Dept.

Thomas L. Paez, Angel Urbina
Validation and Uncertainty Quantification Dept.

D. Michael Ashbaugh
Airworthiness Assurance Dept.

Sandia National Laboratories
P.O. Box 5800
Albuquerque, NM 87185-0555

Abstract

Dynamic thermography is a promising technology for inspecting metallic and composite structures used in high-consequence industries. However, the reliability and inspection sensitivity of this technology has historically been limited by the need for extensive operator experience and the use of human judgment and visual acuity to detect flaws in the large volume of infrared image data collected. To overcome these limitations new automated data analysis algorithms and software is needed. The primary objectives of this research effort were to develop a data processing methodology that is tied to the underlying physics, which reduces or removes the data interpretation requirements, and which eliminates the need to look at significant numbers of data frames to determine if a flaw is present. Considering the strengths and weakness of previous research efforts, this research elected to couple both the temporal and spatial attributes of the surface temperature. Of the possible algorithms investigated, the best performing was a radiance weighted root mean square Laplacian metric that included a multiplicative surface effect correction factor and a novel spatio-temporal parametric model for data smoothing. This metric demonstrated the potential for detecting flaws smaller than 0.075" in inspection areas on the order of one square foot. Included in this report is the development of a thermal imaging model, a weighted least squares thermal data smoothing algorithm, simulation and experimental flaw detection results, and an overview of the *ATAC* (Automated Thermal Analysis Code) software that was developed to analyze thermal inspection data.

CONTENTS

EXECUTIVE SUMMARY 10

1.0 INSPECTION PROCESS OVERVIEW AND PROBLEM STATEMENT 11

1.1 Inspection System Configuration 11
1.2 Inspection System Operation 11
1.3 Inspection Challenges 12

2.0 INSPECTION SYSTEM MODELING 13

2.1 Image Noise Sources 14
2.1.1 Camera Noise Characterization 14
2.1.2 Surface Artifact Noise 16
2.2 Thermal Imaging Model 18
2.2.1 Thermal Image Noise Model 19
2.3 Finite Element Modeling 20
2.4 Thermal Finite Element Model Results 21
2.4.1 Case 1: Unpainted Aluminum Plate With Flat Bottom Holes 22
2.4.2 Case 2: Painted (5 mil) Aluminum Plate With Flat Bottom Holes 23
2.4.3 Case 3: Painted (10 mil) Aluminum Plate With Flat Bottom Holes 24
2.4.4 Case 4: Unpainted Aluminum Plate With Hemispherical Holes 25
2.4.5 Case 5: Painted (5 mil) Aluminum Plate With Hemispherical Holes 27
2.4.6 Case 6: Painted (10 mil) Aluminum Plate With Hemispherical Holes 28
2.4.7 Case 7: Bonded Aluminum Plate With Circular Disbonds 29

3.0 IMAGE ANALYSIS 30

3.1 Thermal Theory and Analytical Solutions 30
3.2 Conventional Signal-Processing 33
3.3 Parametric Model for Spatio-Temporal Smoothing of Image Data 39

4.0 DATA ANALYSIS RESULTS 44

4.1 Energy Balance Metric 45
4.2 Flaw Detection Results Using Finite Element Data 47
4.3 Flaw Detection Results Using Experimental Data 53
4.3.1 Flaw Detection Metric Comparison 54
4.3.2 Experimental Results: Radiance Weighted RMS Laplacian Metric 64
4.4 Surface Effects 68
4.4.1 Surface Effects Correction Factor 72
4.4.2 Paint Thickness Effects On Flaw Detection 76

5.0 CONCLUSIONS AND RECOMMENDATIONS 80

6.0 REFERENCES 82

APPENDIX A: ATAC THERMAL IMAGING ANALYSIS SOFTWARE 85

A.1 The Main Menu Screen 85
A.2 The Load Data Menu 86

A.3 THE VISUALIZE MENU 87
A.4 THE ANALYZE MENU 90
A.5 THE VIEW RESULTS MENU 95

FIGURES

Figure 1. Temporal noise for an image of an unheated aluminum plate. 15
Figure 2. Thermal images of an unheated aluminum plate. 16
Figure 3. Flaw evolution in the presence of surface induced noise. 17
Figure 4. Surface noise latency. 17
Figure 5. Sample thermal image with contrast enhancement. 33
Figure 6. Sample results using edge detection filters. 34
Figure 7. Sample results for diagonal edge detection filters. 35
Figure 8. Sample results for a Sobel filter. 35
Figure 9. Sample results using Laplace filters. 36
Figure 10. Sample results using a relief filter. 37
Figure 11. Sample results using a sequential filter. 37
Figure 12. Sample results using a sequential derivative filter. 37
Figure 13. Sample results for a difference of Gaussians filter with Rayleigh equalization... 38
Figure 14. Sample results using a Frei and Chen filter. 38
Figure 15. Simulated thermal image of an aluminum plate with a flat bottom hole. 48
Figure 16. Composite temporal derivative images. 49
Figure 17. Composite Laplacian images using grayscale data. 50
Figure 18. Composite Laplacian image using approximate temperature data. 51
Figure 19. Composite Laplacian image for a painted specimen. 51
Figure 20. Composite Laplacian images for hemispherical and flat bottom holes. 52
Figure 21. Composite Laplacian image for a simulated adhesive disbond. 53
Figure 22. F-15 composite rudder specimen flaw design. 54
Figure 23. Composite Laplacian image for an F-15 rudder. 54
Figure 24. Composite radiance image. 58
Figure 25. Composite temporal first derivative image. 59
Figure 26. Composite temporal second derivative image. 59
Figure 27. Composite spatial Laplacian image – variant 1. 60
Figure 28. Composite spatial Laplacian image – variant 2. 61
Figure 29. Composite radiance weighted Laplacian image – variant 1. 61
Figure 30. Composite temperature weighted Laplacian image – variant 2. 62
Figure 31. Composite temporal derivative weighted Laplacian image. 63
Figure 32. Composite temporal second derivative weighted Laplacian image. 63
Figure 33. 0.1” diameter flaw detection results. 64
Figure 34. Multiply flawed test specimen detection results. 65
Figure 35. 0.475” flaw detection example. 66
Figure 36. 0.225” flaw detection example. 66
Figure 37. Composite doubler example. 67
Figure 38. Sample image: Minimal surface energy storage example. 68
Figure 39. Temporal cooling plots: minimal surface energy storage example. 69
Figure 40. Sample image: Significant surface energy storage example. 70
Figure 41. Temporal cooling plots: anomalous surface effects example. 71
Figure 42. Temporal surface cooling plots with preflash image subtraction. 72
Figure 43. Temporal surface cooling plots with a multiplicative surface correction factor. . 73
Figure 44. Surface emissivity variation correction analysis example. 74
Figure 45. Surface emissivity variation correction analysis example number 2. 75

Figure 46. 0.075” flaw detection with the application of a surface correction factor..... 76
Figure 47. Painted test specimen design. 77
Figure 48. Paint thickness test specimen composite results. 78
Figure A-1. ATAC Main Menu Window. 86
Figure A-2. Error message displayed if a function is selected before a datacube is loaded.. 86
Figure A-3. Load Data menu. 87
Figure A-4. Datacube compression warning message. 87
Figure A-5. Visualizer tool window. 88
Figure A-6. Data visualization example. 90
Figure A-7. Analyze Menu: Input Parameters Tab. 91
Figure A-8. Analyze Menu: Analysis Method Tab. 94
Figure A-9. Analysis status window. 95
Figure A-10. Warning message when no data is available for display. 96
Figure A-11. View Results menu window with sample results. 97

EXECUTIVE SUMMARY

Dynamic thermography is a nondestructive technique that uses an infrared camera to measure the thermal response of a structure to heating. The presence of an internal defect such as corrosion, cracks, or disbonds perturbs the normal heat flow in a manner that can be detected in an infrared image of the specimen surface. The defect signature varies with the loading mechanism (e.g., pulsed heating, periodic heating, heating profile), the defect location, the material properties and configuration of the inspected structure, and the thermal parameter measured. Dynamic thermography is a proven method for inspecting metallic and composite structures used in high-consequence industries. This technology has demonstrated the ability to detect, identify, and quantify hidden flaws at levels that often dramatically exceeds the capabilities of competing nondestructive testing technologies. However, the reliability of this technology is limited by the need for extensive operator experience and the use of human judgment and visual acuity to detect flaws in the large volume of infrared image data collected. The inspection speed, reliability, sensitivity, and cost effectiveness of dynamic thermography can be significantly improved with advanced signal-processing algorithms.

Operationally, the inspection systems typically flash heat an inspection surface and monitor the surface temperature over time with an infrared camera. Internal anomalies perturb heat conduction by increasing the local storage or transmission of energy as heat. These perturbations induce local spatial temperature gradients on the inspection surface that are imaged by the infrared camera. However, since surface features (e.g., emissivity variations) can also create apparent spatial gradients, the temporal image characteristics must be used to distinguish between true internal flaws and surface artifacts. Further, infrared image data contains both spatial and temporal noise that challenges classical signal processing methods.

This report presents the results from a project to develop automated data analysis algorithms and software for dynamic thermography inspection systems. The developed software package, *ATAC* (Automated Thermal Analysis Code), processes thermography datacubes (temporal sequence of infrared images) to produce a composite image highlighting suspected internal anomalies. The software relies on metrics that consider the spatial and temporal physics of the thermal detection process and an automated noise mitigation algorithm. Multiple flaw detection algorithms and digital signal processing (DSP) operators are provided in the *ATAC* software. Of the algorithms included in *ATAC*, the best performing is a surface radiance weighted root mean square Laplacian operator.

An important feature of the *ATAC* software is a process that mitigates spatial and temporal image noise and variations in the surface properties (principally emissivity). The measured image data (surface radiance) is first multiplied by a spatially variable correction factor that normalizes spatial emissivity differences. This corrected data is then smoothed using a statistical method that fits local data subsets to an 18-parameter spatio-temporal trivariate quadratic polynomial. The fitting is performed by the weighted least squares identification of the polynomial model parameters with temporal weighting. Each local polynomial model is used to estimate the radiance and partial derivatives at the data window center as a function of (x, y, t) along the inspection surface. The model parameter outputs replace the image data and directly feed the developed DSP flaw detection operators. The result from this process is a composite image that highlights locations that have a high probability of containing flaws.

1.0 INSPECTION PROCESS OVERVIEW AND PROBLEM STATEMENT

Dynamic thermography is a diagnostic method with demonstrated inspection capabilities on metallic and composite structures. General capabilities include detection of disbonds (air gaps) in bonded and inhomogeneous metallic structures, hidden corrosion detection with a demonstrated sensitivity below 3% material loss, detection of composite interply delaminations, detection of composite impact damage, mechanical integrity measurements (e.g., weld inspection), material alloy anomaly detection, and fluid ingress detection. However, as will be discussed in section 1.3, the inspection sensitivity and reliability are limited by a protracted and subjective analysis process and various noise sources.

1.1 Inspection System Configuration

Dynamic thermography systems can be configured in a variety of ways. However, the basic elements consist of a thermal source to heat the inspection area, an infrared camera to monitor the surface thermal emissions, and a computer to control the data acquisition, reduction, and display. The system used to support the research presented in this report was a Thermal Wave Imaging system manufactured by TWI, Inc. The inspection system hardware includes the following:

1. Two linear Xenon flashtubes with variable power output up to 6 KJ each. The pulse width produced by these flashtubes is approximately 5 msec.
2. Balcar power supplies.
3. Amber Galileo infrared focal plane array camera. The detector material is Indium Antimonide and operates at 3 – 5 μm. A Stirling closed cycle system is used to cool the detector array. The detector pitch is 30 μm. This camera has adjustable integration time and frame rate with a maximum frame rate of 1000 Hz. The detector array size is 256 x 256 pixels, though windowing is required to operate the camera at speeds faster than 130 Hz. The windowing options are 256 x 256, 127 x 124, and 64 x 64. Pixel Nonuniformity Correction tables are generated during calibration. The acquired images have 12 bit radiometric resolution.
4. Pentium 2 computer with 512 MB RAM. All images are captured in RAM. This limits the maximum number of frames that can be captured.
5. Aluminum shroud that houses the flashtubes and encloses the inspection area to contain the flash.

Inspection system calibration was performed with an Omega model BB701 blackbody. This blackbody has a ±0.1°C stability, a cavity emissivity of 0.98 to 0.99, and a temperature operating range from –4 to 300 °F.

1.2 Inspection System Operation

The inspection process is initiated by irradiating the specimen surface with a high intensity, short duration flash lamp pulse. The absorbed energy conducts laterally and longitudinally away from the heated region at a rate governed by the local temperature gradient and the specimen thermal diffusivity. Localized internal or back surface anomalies produce regions of differing thermal diffusivity that affect the global heat conduction process. These

anomalous regions can act as insulators that slow the heat transport, heat sinks that store and reradiate energy, or conductors that increase the rate of heat diffusion. In each of these instances the perturbations to the heat conduction create transient changes in the temperature distribution that are visualized with infrared images of the specimen surface.

1.3 Inspection Challenges

Though dynamic thermography has shown great promise, commercial systems have demonstrated questionable reliability because of their reliance on human judgement for flaw detection. The acquired temporal datacube is visually interpreted frame by frame to detect flaws. Given that more than 1000 images are often taken during a single data acquisition cycle, this is a labor-intensive and often unreliable process. Also, since the acquired images are 12 to 16 bit and the monitor display is 8 bit, the system operator must select which eight bits to display or rely on automated histogram based methods for selecting the displayed data bits. Further, there is a typically a large dynamic range in each image, and "hot spots" often dominate the contrast enhanced image and hide flaws. Additionally, this time consuming subjective analysis process must deal with a variety of other issues, including the following:

The acquired thermal images are temporally and spatially noisy (digital and specimen induced noise such as emissivity variations). Sequential frame averaging, image filtering, and other conventional image processing methods can reduce this noise and enhance flaw visualization. However, image processing can also hide flaws which are small or that have a low signal to noise ratio. Data noise must be statistically characterized and mitigation algorithms developed.

The initial surface heating is rarely uniform and can create thermal images that are dominated more by the initial absorbed heat distribution than by flaw induced effects. Subtraction of the initial image from subsequent images can help flaw visualization, though high contrast surface artifacts can still dominate the thermal images. Further, the natural diffusion effects of the transient heat conduction limit the utility of baseline image subtraction to early time images. Subtraction of the initial image from late time images can induce artifacts associated with surface features rather than internal flaws. More sophisticated processing techniques must be used to accommodate heating nonuniformities.

Thermal images are inherently low contrast and human judgement of the displayed grayscale images is used for flaw detection. The analyst must both visualize the anomaly and determine if it is a flaw, an artifact produced by the specimen surface features (e.g., paint variations, surface roughness, foreign bodies such as grease, dirt or insulation), or structural conditions (e.g., presence of local heat sinks or material property differences). Human judgment can be unreliable since the character of the displayed images is directly controlled by user specified image display parameters. Algorithms are needed to objectively analyze the full 16 bit temporal datacube.

Thermal reflections (principally from the flash tubes) can generate hot spots that locally saturate the camera or that produce signal strengths that obscure the

presence of flaws when automated contrast adjustment methods are applied. Fortunately, thermal reflections typically only occur if the surface is highly specular or has a shape that tends to image the lamps onto the detector. Coating the inspection surfaces with a removable wax or water based paint that makes the surfaces more diffuse can reduce these reflections. When the surface coating or rearrangement of the imaging configuration does not reduce the thermal reflection enough, other methods such as signal processing may be needed. Though little work has been done in this area, it may be possible to apply a homomorphic filter may reduce these effects.

Optical system effects (i.e., optical aberrations – principally distortion) are very common in thermal infrared imaging systems and can reduce the accuracy of spatial measurements. In principle these effects can be avoided with a well corrected optical system. However, the high cost of infrared optics makes this a cost prohibitive options. Instead, it may be better to do post-processing to correct for the image distortion.

To date there have been no successful attempts to develop generalized algorithms to analyze acquired thermal datacubes for the presence of flaws. Flaw detection currently requires that the user observe a grayscale variation in the temporally and radiometrically subsampled 16 bit images. The only software currently fielded with commercial inspection systems to address this challenge is conventional post-processing noise smoothing filters, frame subtraction software for comparing images, and first derivative approximation software which relies on a linear approximation to the temporal temperature change at a given image position. These simplistic algorithms operate quickly and can be used to improve the visibility of an image region with a visually apparent flaw. However, they do not provide reliable flaw detection capabilities.

The governing physics of transient heat conduction can be used to establish metrics that highlight the presence of a flaw. Both the transient lateral and longitudinal diffusive effects produce thermal signatures that highlight the temporal initiation of the flaw perturbation effects. In addition to flaw detection, a useful byproduct of the detection of the temporal heat perturbation is flaw quantification. The data acquired at this time slice should have the minimum amount of diffusive artifacts and thereby provide an accurate indication of the flaw depth and lateral size.

2.0 INSPECTION SYSTEM MODELING

When there is visual or a priori evidence of the presence of a flaw, image processing can be successfully used to enhance the contrast or desired features in an infrared image. However, when such information is lacking, blind application of signal processing techniques rarely result in success when applied to dynamic thermography performed on complex structures. As such, when it is possible, data analysis algorithms should be tailored to the physics of the inspection process and should be robust in the presence of noise. Therefore, a natural place to begin the development of data analysis algorithms is an investigation of the noise environment and creation of an inspection system model.

2.1 Image Noise Sources

Flaw visualization, whether performed interactively or with automated analysis software, is impacted by multiple noise sources. These sources include emissivity variations across the inspection surface, non-uniform surface heating, thermal reflections (mostly from the flash tubes), optical system effects (e.g., detector noise, optical aberrations – mainly distortion), spatial variations in paint thickness, and complex system structures that create the presence of strong thermal insulators or heat sinks. Each of these factors can produce spatially varying image intensities that contribute to the obscuration of hidden flaws. Proper calibration of the inspection system and judicious selection of the inspection geometry can reduce the impact of some of these noise sources, but complete noise elimination is not possible.

2.1.1 Camera Noise Characterization

Under ideal conditions the inspection system performance is limited by the camera detector noise. For purposes of this project an Amber Galileo camera was used to perform the thermal inspections. The manufacturer advertises the following camera specifications:

Detector Material: InSb
Focal Plane Array Size: 256 x 256 pixels
Pixel Size: 30 x 30 microns
Sensitive Flux Range: 10^{13} to 10^{15} photons/cm^2-sec (nominal $2x10^{14}$ photons/cm^2-sec)
Charge Handling Capacity: 10^6 electrons
Noise Equivalent Flux Density (NEQ): $2x10^{11}$ photons/cm^2-sec in 3-5 micron waveband
Frame Rate: Variable to 1400 Hz with detector array windowing
Dynamic range: 12 bit (4096 grayscales)
Integration Time: Variable from 10 microseconds to 8.6 msec (1.38 msec was used for the noise tests)
Noise Equivalent Temperature Difference (NETD): Rated at less than 0.025 K at 23 °C with a standard deviation to mean ratio less than 0.1%.

From a noise standpoint, the NETD establishes the temperature difference needed to generate a signal to noise ratio of one. The performance of the camera used in this project was measured at 15 °C, 25 °C, 30 °C, and 40 °C. Using a two-point calibration process to perform pixel nonuniformity corrections (NUC), the camera demonstrated a measured mean NETD of 0.0155 K with a standard deviation of 0.002 K. The measured temporal fluctuation magnitude was 0.051%. Typically the spatial variations after applying the NUC are ± 0.010-0.015 K. These values establish the calibrated capabilities of the system in a controlled laboratory using a blackbody source. In practice the system is usually not optimally calibrated and the imaged structures are not blackbodies. As such, the achievable flaw induced temperature rise detection capabilities are typically well above the laboratory NETD. The "in-field" measurement sensitivity and noise levels depend on the character of the inspected structure (both surface and subsurface), the ambient environment, and the detector calibration. Though the inspected surface and environmental noise levels cannot be bounded a priori, it has been shown that without calibration and pixel nonuniformity corrections the detector root mean square spatial noise (standard deviation/mean) is typically 1.5 to 2%.

To investigate the noise that may be more typical of levels experienced in field use, tests were run using a quasi-isothermal aluminum plate at room temperature. Two data sets consisting of 669 image frames (256 x 256 pixels) were acquired at camera frame rates of 15 Hz, 30 Hz, 60 Hz, and 120 Hz. The camera was not calibrated prior to this data acquisition, though it had been calibrated months earlier. The average signal standard deviation/mean for the full data sets varied from 8.7% to 9.1%. However, a temporal evaluation of 64 image points (see sample plots in figure 1) demonstrated that the major fluctuations were not temporal in nature, though some minor plate cooling appeared to be occurring (possibly conduction into the concrete floor the plate was placed on). The temporal fluctuations at the 64 evaluated points varied from a low of 0.043% to a high of 0.077%. Considering the quantization level for the 12 bit camera system and the 16 bit image file (data quantized into 4 grayscale increments), this fluctuation level corresponded to the minimum grayscale change and was consistent with the blackbody calibrated fluctuation level that was later measured at 0.051%. As a result, the large data set variations tended to be more from surface variations (possibly small spatial thermal or emissivity variations) and it was concluded that temporal detector noise fluctuations would not be a significant noise source for data analysis. Further, there was no evidence of frame rate dependent effects. However, in these tests the same camera integration time was used for each frame rate. It is possible that with significantly increased frame rates that noise levels could increase and sensitivity decrease because of the need to reduce the detector integration time. Figure 2 contains an image of the test article with the grayscales adjusted to display the spatial variations. The total signal range for the images represents a ± 1% variation in signal strength relative to the mean.

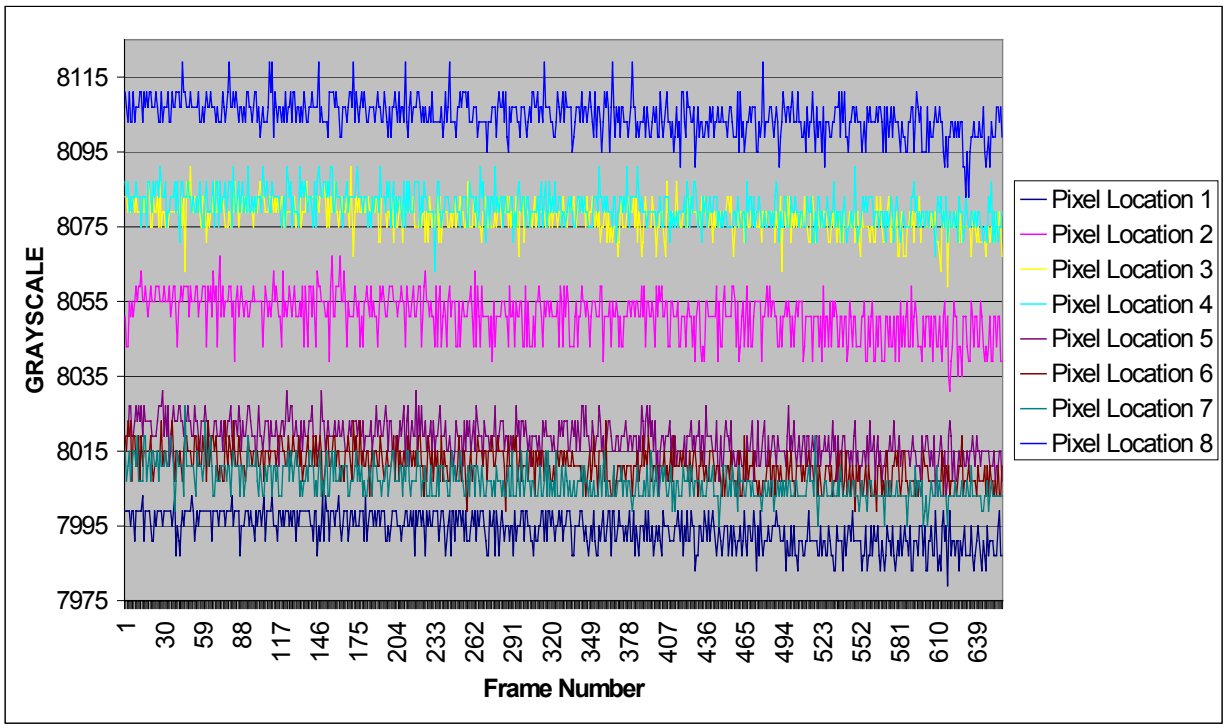

Figure 1. Temporal noise for an image of an unheated aluminum plate.

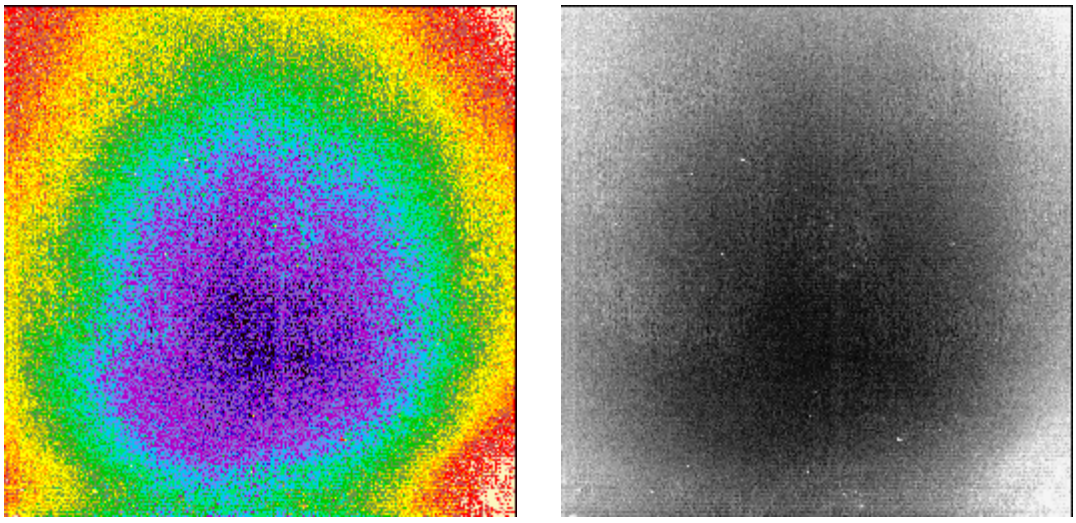

Figure 2. Thermal images of an unheated aluminum plate.

2.1.2 Surface Artifact Noise

Section 2.1.1 considered the ideal condition where the image noise is camera limited. In reality, the surface and near surface induced noise is typically the dominant noise source for infrared inspection systems. This noise can be caused by surface contamination (e.g., grease, dirt), emissivity variations (e.g., contamination, differing materials), unplanned material thickness variations (e.g., paint thickness deviations), or surface reflections. Since surface reflections can typically be handled with the proper selection of the inspection configuration or through post–processing, it will not be considered further.

Consider the sequence of post-flash heating images presented in figure 3. These pictures display the infrared images of a 10”x10”x”0.060” aluminum plate with a 0.475” diameter flat bottom hole that were acquired at frames 21, 23, 25, 27, and 73 after the flash for a camera operating at 476 frames per second. In each frame the gray scale histogram was used to automatically enhanced the image and improve the flaw visibility. This type of contrast enhancement works well when the flaw is the primary source of “hot spots” in the image, but performs poorly when there are other causes for the apparent high temperature regions. Designed or unplanned material property variations can have differing thermal properties, causing selected image regions to conduct energy much slower than surrounding regions. In these cases the hotter region may not be indicative of a flaw, but it can obscure lower signal strength flaws that are located in the cooler image regions. Also, differing materials may have dissimilar emissivity values that create the false appearance of temperature variations.

In figure 3 the mottled appearance in frames 21-27 is caused by surface paint thickness variations in the thin layer of water based black Crayola paint that was applied to the inspection surface with a roller. This removable paint is often applied to an inspection surface to increase the coupling of the thermal energy from the flash tubes and to reduce specular reflections. Though the paint thickness variations were not quantified, they were probably on the order of 1 mil. As shown in the images, paint variations are highly visible despite the relatively small amount of paint applied to the inspection surface. This occurs

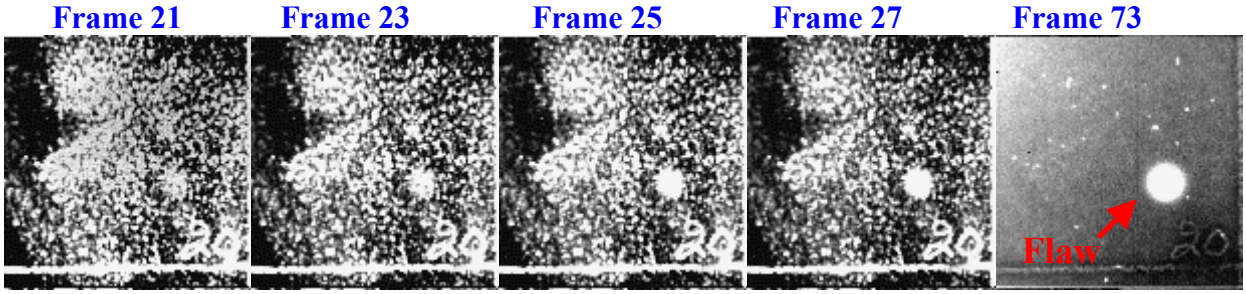

Figure 3. Flaw evolution in the presence of surface induced noise.

because small variations in paint thickness are magnified in comparison to aluminum because of the large difference in thermal properties. Fortunately these surface artifacts diminish with time as shown in frame 73 (far right image). However, as shown in these images, the circular flaw becomes visible before the surface effects disappear. In these images the flaw has large signal strength and good latency. Unfortunately this is not always the case. As such, algorithms developed for automated flaw detection should be robust in the presence of the noise levels displayed in figure 3.

As a second example of surface noise latency, consider the post-flash contrast enhanced image sequence and the corresponding signal strength plots provided in figure 4. These infrared images are of a 10”x10”x0.060” aluminum plate with a 0.5” diameter flat bottom hole that were acquired at 476 frames per second. The three images displayed are for frames 19, 24, and 70. As with the test case displayed in figure 1, the flaw had excellent visibility and latency. Here the surface paint variation effects were significantly reduced by frame 24 and were virtually nonexistent at frame 70.

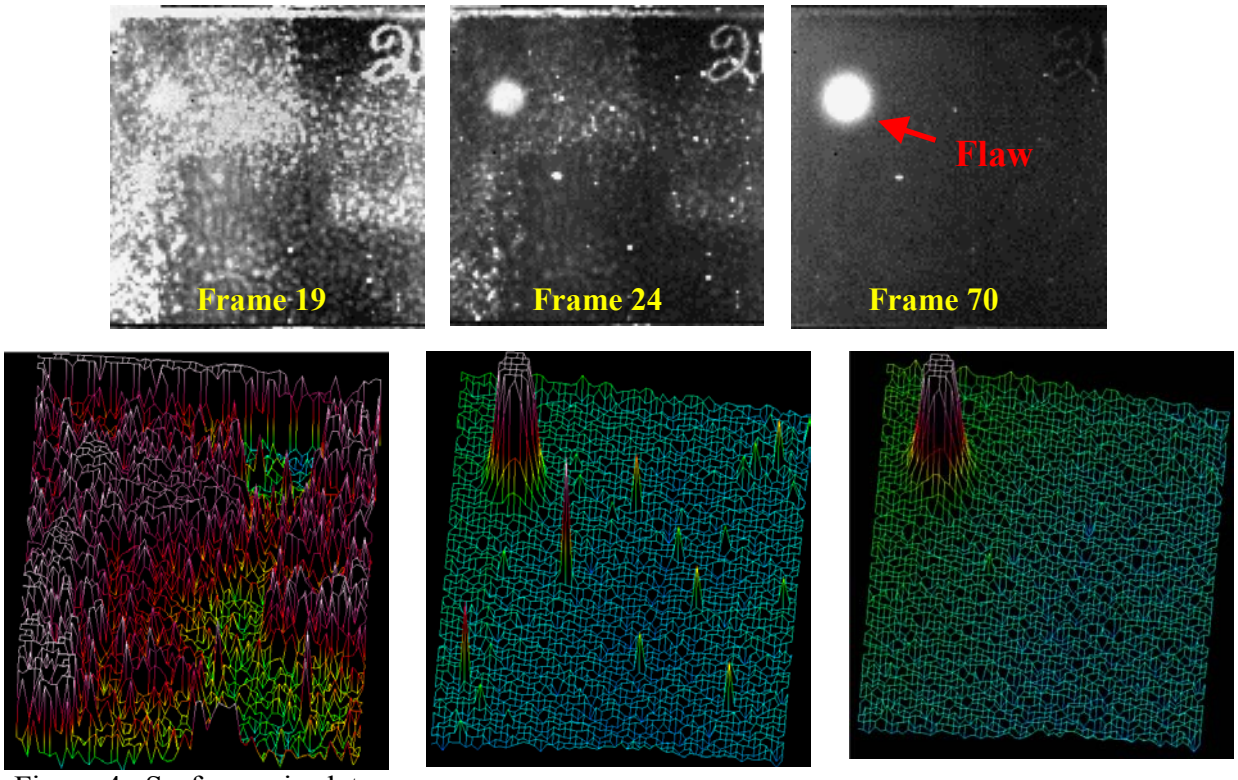

Figure 4. Surface noise latency.

In the test cases illustrated in figures 3 and 4, the noise overwhelmed the flaw signal during the early frames but decayed long before the flaw signature started to fade. In these instances advanced signal processing for flaw detection is rarely needed. The challenge is to detect small flaws with short latency or near surface flaws when significant thermal noise is present.

2.2 Thermal Imaging Model

Finite element model results provide temporal surface temperature profiles that can be used to predict surface temperatures in support of flaw detection algorithm development. However, though the thermal imaging system is sensitive to surface temperature, what is actually captured is energy radiated from the inspection surface. As a result, the simulated surface temperatures must be transformed into the image grayscales induced by the thermal radiation (flux exitance). This is accomplished by converting the temperature dependent surface radiated energy into irradiance on the detector.

The total flux exitance from the modeled inspection surface is computed by integrating the expression for spectral photon flux exitance for a graybody over the camera spectral operating range. This exitance, together with the optical system transmission and F/#, defines the image plane irradiance (flux density) that would be produced by the simulated inspection surface. The computed image plane irradiance can be converted to image grayscales using the known detector noise equivalent photon flux and sensitive flux range.

Image plane irradiance is defined by the expression

$$(1) \qquad E_d = \frac{\pi L_s T_r}{4(F_{eff}^{\#})^2} = \frac{M_s T_r}{4(F_{eff}^{\#})^2}$$

where,

E_d = incident photon flux density on detector plane,
L_s = photon flux radiance emitted from inspection surface,
M_s = photon flux exitance,
T_r = lens transmission,
$F_{eff}^{\#}$ = optical system effective F/number.

Further, the spectral photon flux exitance M_λ for a blackbody is defined by the equation

$$(2) \qquad M_\lambda = \frac{2e^8 \pi c}{\lambda^4 \left\{ e^{\frac{hc}{\lambda kT}} - 1 \right\}} \quad \frac{photons}{sec - cm^2 - \mu m}$$

where,

λ = wavelength (microns),
h = Planck's constant = 6.626176 x 10^{-34} W/sec^2,
c = speed of light = 2.99792438 x10^{14} microns/sec,
k = Boltzmann's constant = 1.380662 x 10^{-23} W/(sec-K),
T = surface temperature (K).

Though the inspection surface does not approximate a blackbody, we can assume it is a graybody (constant emissivity ε) for the temperatures and spectral band of interest. As a result, the total photon exitance M_s from the surface at temperature T can be computed by integrating the blackbody spectral photon flux exitance M_λ over the desired waveband. Hence, the image irradiance is computed using the following general expression:

$$(3) \qquad E_d = \frac{\varepsilon \, T_r}{4(F_{eff}^{\#})^2} \int_{\lambda_1}^{\lambda_2} M_\lambda \, d\lambda .$$

The integration in equation (3) is best performed using Gauss-Laguerre quadrature because of the form of the M_λ relation. Eight quadrature points are adequate for thermal inspection modeling because of the character of Planck's distribution over the wavelengths and surface temperatures of interest. The system parameters used in equation (3) depend on the infrared camera selected to perform the inspection. The inspection system used in this research has a responsive waveband of 3-5 microns, an effective F/number of 3.075, and a lens transmission of 0.90. Though there are some minor variations in lens transmission over the 3 - 5 micron region, they are negligible for our modeling purposes. Finally, the emissivity is assumed to be 0.25 (unpainted worn aluminum) over the entire waveband for the modeled surface. Though painted surfaces typically provide much higher emissivity values (0.9 is typical), using a value of 0.25 provides a more conservative value for estimating detection limits.

Equation (3) converts the computed surface temperatures into equivalent detector irradiance (flux density) values. To produce a simulated infrared image we must convert the computed irradiance values into grayscales. The image grayscales can be computed from the calculated image plane flux density using the known detector NEQ and sensitive flux range. Using a maximum allowable flux of $1x10^{15}$ photons/cm^2-sec, an NEQ of $2x10^{11}$ photons/cm^2-sec, and a dynamic range of 4096 grayscales (12 bit camera) gives an operating flux range of about $1.8x10^{14}$ to $1x10^{15}$ photons/cm^2-sec. However, the advertised detector sensitivity range is approximately $1x10^{13}$ to $1x10^{15}$ photons/cm^2-sec. As such, it can be seen that the photon flux density per grayscale is slightly above the NEQ level with a value of approximately $2.42x10^{11}$ photons/cm^2-sec. Hence, assuming the detector is linear as a function of incident flux density allows the photon flux density is converted to grayscales using the relationship

$$(4) \qquad \text{grayscale} = (E_d - 1x10^{13}) \,/ 2.42x10^{11}$$

This approximation sets values below $1x10^{13}$ to "0", and values above $1x10^{15}$ to "4095".

2.2.1 Thermal Image Noise Model

The experimental investigation of the infrared camera in section 2.1.1 suggested that temporal camera noise should not be a significant noise source impeding data analysis. To investigate this assumption temporal thermal image noise was included in the thermal image model as normally distributed additive noise. Two options were considered for adding the noise to the finite element model results. Noise can be added in post-processing to the images generated with equation (4) or it can be added directly to the apparent surface temperatures used in equation (2). Though arguments could be made that the primary temporal noise sources are governed by the camera (detector, electronics, etc.), preliminary

numerical tests demonstrated that for our purposes it did not make a significant statistical difference at which point in the process the noise effects were added. As a result, the noise was arbitrarily added directly to the temperatures used in equation (2).

Adding normally distributed noise to the modeled surface temperature requires some form of Gaussian sampling. Gaussian sampling cannot be done directly because the cumulative probability distribution is an error function that cannot be analytically inverted. Instead, the sampling is accomplished via a transformation approach involving the selection of two variables uniformly random over the interval (0,1).[1] Given two random numbers y_1 and y_2, noise is added to the finite element temperature predictions using the relation:

$$(5) \qquad Temperature = T_{fe} + \sigma M_{noise} \sqrt{-2 \ln y_1} \cos 2\pi y_2$$

where,

$$T_{fe} = finite\ element\ temperature\ prediction,$$
$$\sigma = noise\ standard\ deviation,$$
$$M_{noise} = thermal\ noise\ magnitude.$$

The random number generation followed the Park and Miller implementation of Schrage's method with Bays-Durham shuffling.[2]

2.3 Finite Element Modeling

As a starting point in the development of data analysis software, thermal finite element modeling was conducted to generate controlled simulation data.[3] Though dynamic thermography can be used to perform many inspection tasks, it is most commonly applied to the detection of missing material (e.g., hidden corrosion) or air gaps (disbonds) in bonded structures. As such, the finite element modeling focussed on these inspection classes. The varied model parameters included flaw aspect ratio (diameter/depth from surface), flaw shape, and paint thickness. A common rule of thumb is that the physical flaw detection limit is near a flaw aspect ratio of one. However, this presumes the flaw generates a temperature rise above the NETD and that the generated temperature anomaly has a cross-section that is resolvable by the detector optical system. To investigate the importance of a flaw's energy "trapping" capacity, the modeling included cases with equivalent flaw aspect ratios but differing depths from the viewed surface. These cases include situations where the aspect ratio is below one and the flaw cross-section is below the optical resolution limit.

The important parameters to consider when reviewing the results are the peak temperature contrast between the flaw center and the uniform temperature region not influenced by the flaw, the earliest time when the flaw perturbs the surface temperature by at least 0.01°C, and the flaw visibility latency (i.e., cooling rate). The best opportunity for visualizing the flaw in a single frame is when the flaw contrast peaks. However, it is important to recognize that the maximum surface temperature generated by the heating does not correspond to the point where the flaw visibility is at its maximum. As such, it is often not important to visualize the surface during the flash heating event. This is fortunate since the inspection surface flash heating typically saturates the detector, making imaging during this transient event

impractical. Nevertheless, if data analysis methods consider the temporal flaw effects, it may be necessary to capture the initial perturbation of the surface heat profile created by the flaw.

When the flaw depth is shallow and the inspection surface is unpainted, the initial flaw induced temperature deviation can occur shortly after the flash heating, requiring high frame rates to capture its initiation. Indeed, from an analytical standpoint we can expect that the penetration depth of the flash heating thermal pulse into the bare aluminum plate will be about midway into the plate during the pulse duration for the thin structures considered. As such, the flaw will begin to impede the thermal diffusion before the flash heating event is completed. Further, during the flash event the camera detector is typically saturated, preventing any reliable imaging. Therefore, it is reasonable to assume that it may be impractical to observe the flaw initiation in structures with bare aluminum surfaces. However, for painted test specimens, which have a significantly larger thermal time constant than bare aluminum, the penetration depth during the heating pulse will only be a few mils into the paint. Here the initial pulse duration will not affect the ability to visualize flaw initiation, though other thermal characteristics of the paint may impair the flaw detection. For example, the paint's specific heat allows it to store more energy than aluminum for the same induced temperature rise. Also, considering the paint conductivity relative to the aluminum, the paint will significantly reduce the rate at which heat is applied to the aluminum, though it will provide the energy for a longer duration.

Fundamentally the camera cannot detect the beginning of the flaw induced perturbations until the temperature deviation exceeds the NETD. In the case of the camera system used to support this project, the temperature deviation would need to surpass 0.0155 °C for the signal to be larger than the noise. To be conservative in determining an appropriate frame rate to observe the initiation of the flaw, we used the criteria that the system must collect four image frames prior to the frame where the flaw first creates a 0.01 °C temperature rise.

Though peak contrast provides the greatest signal to noise ratio for flaw visualization, flaw temperature latency is a more important feature in automated flaw detection. For example, the peak contrast may be theoretically detectable, but have small signal to noise ratio that has a poor likelihood of detection. Though the temperature rise is small, it typically lasts for many frames. As a result, an accumulation of frames may generate a more detectable flaw signature. Further, such an accumulation would reduce the temporal noise effects.

2.4 Thermal Finite Element Model Results

Finite element modeling was conducted for seven test cases involving flaws sized to produce aspect ratios (flaw lateral diameter/flaw depth from surface) from 0.5 to 5. The modeled flaws included varying amounts of missing material on the backside of painted and unpainted uninsulated aluminum plates and disbonds between bonded plates. The missing material was modeled as either a circular flat bottom hole or a hemispherical hole. All of the disbonds were circular. The following are the general parameters used with each finite element model:

Specimen Size: 10" x 10"
Heating Pulse Duration: 5 msec
Absorbed Energy: 2 kJ (spread uniformly across the specimen surface)

Initial Specimen Temperature: 21.11 °C
Temporal Resolution: 0.00125 seconds
Total Time Duration for Data Acquisition: 240 seconds

Each test case presents the maximum flaw temperature rise relative to the non-flawed area (i.e., temperature rise at peak flaw contrast), the temperature at the flaw center one second after the flash heating (measure of flaw latency), the camera frame rate needed to capture the flaw initiation in the infrared image (0.01°C temperature rise above non-flawed area), and the recommended camera frame rate to capture the flaw's peak contrast.

2.4.1 Case 1: Unpainted Aluminum Plate With Flat Bottom Holes

This case investigated an unpainted aluminum plate with circular flat bottom holes as simulated flaws. The material properties used are as follows:

Material	Thickness (inches)	Density (kg/m^3)	Specific Heat (J/kg °C)	Conductivity (J/sec-m-°C)
Aluminum	0.060	2770	875	163

The model results presented below demonstrate that even the smallest flaw considered (0.0125", aspect ratio of 0.5) is theoretically detectable if the flaw is optically resolvable.

Defect Depth From Surface (inches)	Defect Diameter (inches)	Maximum Flaw Temperature Rise (°C)
No defect	No defect	N/A
0.025	0.0125	0.07
0.025	0.025	0.29
0.025	0.050	1.12
0.025	0.075	2.16
0.025	0.100	3.14
0.025	0.125	3.99
0.05	0.025	0.030
0.05	0.050	0.11
0.05	0.100	0.35
0.05	0.150	0.58
0.05	0.200	0.75
0.05	0.250	0.866

The peak surface temperature generated by the simulated flash heating was 29.6 °C, but the surface cooled quickly as shown below. Though the results confirm that larger flaws trap more energy, one second after the heating the differences between the unflawed and flawed cases is virtually undetectable. As such, for bare aluminum the system should be operated at higher frame rates (120 fps recommended) to capture flaw latency effects and peak contrast. Further, to capture the flaw initiation, the camera would need to be operated in the kHz range. For the flaws located at a depth of 0.25 inches a frame rate of approximately 4000 fps should be used. For the flaws at a 0.5" depth a rate of 2000 fps should be used.

Defect Depth From Surface (inches)	Defect Diameter (inches)	Flaw Center Temperature 1 Second After Flash
No defect	No defect	26.39
0.025	0.0125	26.39
0.025	0.025	26.39
0.025	0.050	26.40
0.025	0.075	26.40
0.025	0.100	26.41
0.025	0.125	26.42
0.05	0.025	26.39
0.05	0.050	26.39
0.05	0.100	26.40
0.05	0.150	26.40
0.05	0.200	26.41
0.05	0.250	26.42

2.4.2 Case 2: Painted (5 mil) Aluminum Plate With Flat Bottom Holes

This case investigated a painted aluminum plate with circular flat bottom holes as simulated flaws. The material properties used are as follows:

Material	Thickness (inches)	Density (kg/m^3)	Specific Heat (J/kg °C)	Conductivity (J/sec-m-°C)
Paint	0.005	1100	3349	0.2
Aluminum	0.060	2770	875	163

The model results below show that the smallest flaw considered (0.0125", aspect ratio of 0.5) is theoretically detectable if the flaw is optically resolvable. When compared to the bare aluminum case, the model results indicate the maximum temperature difference between the flaw center and the region not perturbed by the flaw is greater with the 0.005"paint layer.

Defect Depth From Surface (inches)	Defect Diameter (inches)	Maximum Flaw Temperature Rise (°C)
No defect	No defect	N/A
0.025	0.0125	0.336
0.025	0.025	0.978
0.025	0.050	2.345
0.025	0.075	3.374
0.025	0.100	4.045
0.025	0.125	4.450
0.05	0.025	0.170
0.05	0.050	0.387
0.05	0.100	0.650
0.05	0.150	0.756
0.05	0.200	0.799
0.05	0.250	0.810

The peak surface temperature generated by the simulated flash heating was 146.8 °C, but the surface cooled quickly as shown below. The paint has a much lower conductivity than the aluminum, which significantly delays the initiation of the flaw induced temperature deviation. As a result, a frame rate of 140 frames per second would be adequate for visualizing flaw initiation for both of the flaw depths considered in this case. Also, it is interesting to note that though the surface cooled quickly, unlike the unpainted case (case 1) the presence of the flaw created significant differences in the cooling rate (flaw temperature latency). This would seem to indicate that a 0.005" layer of paint may actually help with the flaw detection by reducing the required frame rate and increasing the latency.

Defect Depth From Surface (inches)	Defect Diameter (inches)	Flaw Center Temperature 1 Second After Flash
No defect	No defect	25.82
0.025	0.0125	25.86
0.025	0.025	25.99
0.025	0.050	26.57
0.025	0.075	27.60
0.025	0.100	28.72
0.025	0.125	29.60
0.05	0.025	25.87
0.05	0.050	25.99
0.05	0.100	26.31
0.05	0.150	26.52
0.05	0.200	26.61
0.05	0.250	26.63

2.4.3 Case 3: Painted (10 mil) Aluminum Plate With Flat Bottom Holes

This case investigated a painted aluminum plate with circular flat bottom holes as simulated flaws. The only difference between this case and case 2 is the paint thickness. The material properties used are as follows:

Material	Thickness (inches)	Density (kg/m^3)	Specific Heat (J/kg °C)	Conductivity (J/sec-m-°C)
Paint	0.010	1100	3349	0.2
Aluminum	0.060	2770	875	163

As with the previous cases, the model results presented below demonstrate that even the smallest flaw considered (0.0125", aspect ratio of 0.5) is theoretically detectable if the flaw is optically resolvable. When compared to the case 2 with a 0.005" paint layer, it can be seen that the maximum temperature difference between the flaw center and the region not perturbed by the flaw decreases with the 0.010" paint layer. Though further investigation is required, this may suggest that there is an optimum paint thickness for flaw detection. Further modeling should focus on the peak contrast temperature as a function of flaw thickness and heating pulse duration.

Defect Depth From Surface (inches)	Defect Diameter (inches)	Maximum Flaw Temperature Rise (°C)
No defect	No defect	N/A
0.025	0.0125	0.109
0.025	0.025	0.327
0.025	0.050	0.900
0.025	0.075	1.500
0.025	0.100	2.020
0.025	0.125	2.440
0.05	0.025	0.070
0.05	0.050	0.167
0.05	0.100	0.350
0.05	0.150	0.477
0.05	0.200	0.550
0.05	0.250	0.590

As with case 2, the peak surface temperature generated by the simulated flash heating was 146.8 °C, but the surface cooled slower with the thicker paint layer. This added paint further delayed the initiation of the flaw induced temperature deviation. As a result, a frame rate of 30 frames per second would be adequate to visualize the flaw initiation for both of the flaw depths considered in this case.

Defect Depth From Surface (inches)	Defect Diameter (inches)	Flaw Center Temperature 1 Second After Flash
No defect	No defect	28.89
0.025	0.0125	28.99
0.025	0.025	29.02
0.025	0.050	29.78
0.025	0.075	30.34
0.025	0.100	30.70
0.025	0.125	30.91
0.05	0.025	28.95
0.05	0.050	29.05
0.05	0.100	29.19
0.05	0.150	29.24
0.05	0.200	29.25
0.05	0.250	29.25

2.4.4 Case 4: Unpainted Aluminum Plate With Hemispherical Holes

This case studied an unpainted aluminum plate with hemispherical backside holes as simulated flaws. Each flaw center is located 0.05” below the metal surface. To maintain the flaw center depth at 0.05” and achieve the desired flaw diameter, the hemispherical flaw radius is varied as shown in the table. The material properties used are as follows:

Material	Thickness (inches)	Density (kg/m^3)	Specific Heat (J/kg °C)	Conductivity (J/sec-m-°C)
Aluminum	0.060	2770	875	163

The model results presented below demonstrate that even the smallest flaw considered (0.0125", aspect ratio of 0.5) is theoretically detectable if the flaw is optically resolvable. However, though the actual NETD of the camera used in this test program was 0.0155 °C, the advertised NETD is 0.025 °C. As such, the smallest flaw is near the fundamental limit of the camera even when it is optimally calibrated.

When compared to the corresponding case 1 that modeled flat bottom holes, case 4 demonstrates that hemispherical backside holes are less efficient at trapping energy (i.e., reducing cooling rate) than flat bottom holes. Given that the heating applied in the model is uniform across the surface, isotherms are created parallel to the surface of the flat bottom holes. When the diffusing heat reaches the top of the flat bottom hole the energy begins to be released by convective cooling at the flaw air-metal interface. Since the convection heat transfer at the flaw is a relatively slow process in comparison to the conduction transfer away from the flaw, the unflawed regions cool much quicker leaving a "hotter" region above the flaw. This higher temperature area above the flat bottom flaw will remain until the lateral temperature gradients needed to conduct the energy away from the flaw propagate in from the flaw edges as the heat diffuses around the flaw. This process is responsible for the trapped energy that results in the flaw signature latency.

Similar to the flat bottom holes, the hemispherical flaws in case 4 begin to perturb the surface temperature profile when the induced heat front conducting through the aluminum first reaches the top of each flaw. However, unlike the flat bottom hole case, as you move laterally away from the flaw center there is a volume of aluminum below the isotherm to conduct the heat. As such, there is a small temperature gradient along the hemispherical flaw that supports further heat conduction. Though the gradient is much smaller than in the regions away from the flaw, it is still significant enough to support cooling rates that are noticeably higher than with the flat bottom holes. The flaw air-metal interface providing convective cooling still acts as an insulator relative to the surrounding conduction. This relative insulation, together with the reduced local temperature gradients is still sufficient to trap sufficient energy for flaw detection. However, the magnitude and latency of the hemispherical flaw signature is significantly smaller than the signature for the equivalent flat bottom hole cross-section.

Hemisphere Radius (inches)	Defect Diameter (inches)	Maximum Flaw Temperature Rise (°C)
No defect	No defect	N/A
0.012813	0.025	0.020
0.03625	0.050	0.040
0.13	0.100	0.070
0.28625	0.150	0.110
0.505	0.200	0.140
0.78625	0.250	0.170

The peak surface temperature generated by the simulated flash heating was 29.58 °C, but the surface over the center of each flaw cooled quickly to about 26.39°C after 1 second. This is the same temperature occurring in the unflawed case. As such, after 1 second there is no evidence of a flaw. As mentioned previous, the hemispherical flaw signature has a relatively short latency time. Further a frame rate of 16000 fps would be needed to capture the flaw initiation because of the small amount of energy trapped by the hemispherical flaw,

2.4.5 Case 5: Painted (5 mil) Aluminum Plate With Hemispherical Holes

This case investigated a painted aluminum plate with hemispherical backside holes as simulated flaws. The center of the each flaw is located 0.05" below the metal surface. To maintain the flaw depth at 0.05" (at flaw center) and achieve the desired flaw diameter, the radius of the hemispherical flaw shape is varied as shown in the table. The material properties used are as follows:

Material	Thickness (inches)	Density (kg/m^3)	Specific Heat (J/kg °C)	Conductivity (J/sec-m-°C)
Paint	0.005	1100	3349	0.2
Aluminum	0.060	2770	875	163

The model results presented below demonstrate that the smallest flaw considered (0.0125", aspect ratio of 0.5) is theoretically detectable if the flaw is optically resolvable. As with case 2, it can be seen that the maximum temperature difference between the flaw center and the region not perturbed by the flaw is greater when the 0.005"paint layer is present.

Hemisphere Radius (inches)	Defect Diameter (inches)	Maximum Flaw Temperature Rise (°C)
No defect	No defect	N/A
0.012813	0.025	0.050
0.03625	0.050	0.069
0.13	0.100	0.180
0.28625	0.150	0.290
0.505	0.200	0.379
0.78625	0.250	0.450

The peak surface temperature generated by the simulated flash heating was 146.8 °C, but the surface cooled quickly as shown below. Similar to case 2, the 0.005" paint appeared to improve the flaw signature visibility and latency. As with case 2, a frame rate of 140 frames per second would be adequate for visualizing flaw initiation.

Hemisphere Radius (inches)	Defect Diameter (inches)	Flaw Center Temperature 1 Second After Flash
No defect	No defect	N/A
0.012813	0.025	25.82
0.03625	0.050	25.84
0.13	0.100	25.88
0.28625	0.150	25.94
0.505	0.200	26.01
0.78625	0.250	26.09

2.4.6 Case 6: Painted (10 mil) Aluminum Plate With Hemispherical Holes

This case investigated a painted aluminum plate with hemispherical backside holes as simulated flaws. The only difference between this case and case 5 is the paint thickness. The material properties used are as follows:

Material	Thickness (mil)	Density (kg/m^3)	Specific Heat (J/kg °C)	Conductivity (J/sec-m-°C)
Paint	0.010	1100	3349	0.2
Aluminum	0.060	2770	875	163

The model results presented below demonstrate that the smallest flaw considered (0.0125", aspect ratio of 0.5) is theoretically undetectable even if the flaw is optically resolvable. Further, the next smallest flaw considered (0.025", aspect ratio of 1.0) is very close to the theoretical detection limit. As with case 3, increasing the paint thickness from 0.005" to 0.010" significantly reduced the flaw detectability.

Hemisphere Radius (inches)	Defect Diameter (inches)	Maximum Flaw Temperature Rise (°C)
No defect	No defect	N/A
0.012813	0.0125	0.010
0.03625	0.025	0.030
0.13	0.050	0.070
0.28625	0.075	0.120
0.505	0.100	0.177
0.78625	0.125	0.220

As with case 5, the peak surface temperature generated by the simulated flash heating was 146.8 °C, but the surface cooled slower in case 6 because of the thicker paint layer. This added paint further delayed the initiation of the flaw induced temperature deviation. As a result, a frame rate of 24 frames per second would be adequate to visualize the flaw initiation for both of the flaw depths considered in this case. When compared with case 3 (0.010" paint, flat bottom hole), it can be observed that it takes longer for the flaw to trap sufficient energy to produce a detectable signature.

Hemisphere Radius (inches)	Defect Diameter (inches)	Flaw Center Temperature 1 Second After Flash
No defect	No defect	28.89
0.012813	0.0125	28.90
0.03625	0.025	28.91
0.13	0.050	28.96
0.28625	0.075	29.00
0.505	0.100	29.06
0.78625	0.125	29.10

2.4.7 Case 7: Bonded Aluminum Plate With Circular Disbonds

This case investigated bonded aluminum plates with circular disbonds in the adhesive layer between the plates. The material properties used are as follows:

Material	Thickness (inches)	Density (kg/m^3)	Specific Heat (J/kg °C)	Conductivity (J/sec-m-°C)
Aluminum	0.060	2770	875	163
Cytec FM73 Adhesive	0.005	1150	1255.2	0.22
Aluminum	0.060	2770	875	163

The model results presented below demonstrate that the two smallest flaws considered (0.03"- aspect ratio of 0.5, 0.06" – aspect ratio of 1) are theoretically undetectable even if the flaw is optically resolvable. This is predominantly due to the lower thermal conductivity and heat capacity of the adhesive. In many ways the adhesive is thermally comparable to the paint used in previous cases. The conductivity and density are virtually the same. However, since the paint has a specific heat that is three times larger, it is better at absorbing and storing the heat energy with less increase in temperature than the adhesive. As a result, the adhesive acts as a better thermal insulator, reducing the local temperature gradients and flaw signature gradient. Nevertheless, though the disbond flaw visibility is reduced the signature latency is still very good.

Defect Diameter (inches)	Maximum Flaw Temperature Rise (°C)
No defect	N/A
0.03	0.010
0.06	0.020
0.12	0.070
0.18	0.130
0.24	0.206
0.30	0.280

The peak surface temperature generated by the simulated flash heating was 29.58 °C, but the surface cooled quickly as shown below. Though the flaw has good thermal latency time the camera would need to be operated at a frame rate of 640 fps to capture the initiation of the flaw signature.

Defect Depth From Surface (inches)	Defect Diameter (inches)	Flaw Center Temperature 1 Second After Flash
No defect	N/A	24.556
0.25	0.03	24.562
0.25	0.06	24.566
0.25	0.12	24.596
0.25	0.18	24.646
0.25	0.24	24.696
0.25	0.30	24.766

3.0 IMAGE ANALYSIS

3.1 Thermal Theory and Analytical Solutions

For thermal inspection applications, assuming no internal generation and isotropic, homogenous materials, the governing equation for transient heat conduction is:

$$(6) \qquad \nabla^2 T = \frac{\partial^2 T}{\partial x^2} + \frac{\partial^2 T}{\partial y^2} + \frac{\partial^2 T}{\partial z^2} = \frac{\rho c_p}{k}\frac{\partial T}{\partial t} = \frac{1}{\alpha}\frac{\partial T}{\partial t}$$

where,

k = thermal conductivity,
ρ = density (kg/m^3),
c_p = specific heat (J/kg °C),
α = thermal diffusivity (cm^2/s),
(x,y) = along surface,
z = into surface.

Analytical solutions to equation (6) can be derived in many forms with differing convergence properties, but each relies on series expansions to describe the surface temperature as a function of position and time. For example, when a plane impulse heat source of intensity Q is applied to the surface of an isothermal homogeneous slab of thickness L with no heat flow across the top or bottom surface, the transient temperature response at the surface (z=0) is given by:[4]

$$(7) \qquad T(t) = \frac{Q\alpha}{kL}\left(1 + 2\sum_{n=1}^{\infty} e^{-\alpha\left(\frac{n\pi}{L}\right)^2 t}\right)$$

Similarly for the 2-D case we get:

$$(8) \qquad T(t) = \frac{Q\alpha}{kLxLy}\left(1 + 2\sum_{n=1}^{\infty} e^{-\alpha\left(\frac{n\pi}{Lx}\right)^2 t}\right)\left(1 + 2\sum_{n=1}^{\infty} e^{-\alpha\left(\frac{n\pi}{Ly}\right)^2 t}\right)$$

Likewise, for the given separable boundary conditions the solution can be extended to 3-D as a product solution. These solutions assume no heat flow across the top and bottom surface after the heat pulse is applied. Changes in the boundary conditions will create corresponding changes in the spatial terms that affect the temperature distribution within the slab.

From a physical standpoint, it is logical to assume that the presence of a flaw may alter the internal energy storage and produce a perturbation in the time rate of change of the surface temperature. If we consider the 1-D case, the change in temperature at the surface over time can be described by:

$$(9) \qquad \frac{\partial T(t)}{\partial t} = -\frac{2Q}{kL}\left(\left(\frac{\alpha\pi}{L}\right)^2 \sum_{n=1}^{\infty} n^2 e^{-\alpha\left(\frac{n\pi}{L}\right)^2 t}\right)$$

In the series solutions provided in equations (7) through (9) we need to be concerned with the number of terms needed to reach convergence. This is governed by the Fourier number ($\alpha\, t/L^2$) that essentially compares the rate of heat conduction through volume to the rate of heat storage in the volume. The larger the Fourier number, the deeper the heat penetration over a given period of time and the faster the series convergence. For thin aluminum structures the series converges very quickly.

The expressions in equation (7) – (9) potentially provide a means of highlighting the presence of a flaw because internal defects generate local surface temperatures that are not consistent with the analytical solutions. However, this assumes the inspection surface and boundary conditions are "perfect" or that differences from the modeled conditions are insignificant. In practice, real and assumed boundary conditions rarely if ever agree and the structural complexity of objects of interest usually does not support closed form solutions. Nevertheless, analytical solutions can still provide useful information regarding trends and help identify flaw induced variations. This is particularly true for relatively thin structures and for shallow flaws.

For other more general structures it is often more computationally efficient to consider an approximate analytic method such as the energy integral equation (heat-balance integral that provides a solution that is correct on the average over the region). This approach begins with an integration of the partial differential equation over a phenomenological distance (thermal layer – defined as the distance beyond which there is no practical heat flow) to remove the derivative with respect to the space variable. Then a profile (usually a polynomial of 4th

degree or less) is selected for the temperature distribution over the thermal layer. This profile results in an ordinary differential equation with time as the independent variable. The solution to the ordinary differential equation is a temperature distribution defined as a function of time and position.

An alternate solution to equation (6) for a 1-D semi-infinite solid with an instantaneous surface heat flux Q provides a temperature profile through the solid described by:[4]

$$(10) \qquad T(x,t) = \frac{Q}{\sqrt{4\pi k \rho c_p t}} e^{\left(-\frac{x^2}{4\alpha t}\right)}$$

Under these conditions the surface temperature (x=0) is proportional to the inverse square root of time. This 1-D solution is often useful when considering relatively homogeneous structures that are very thin in comparison to their lateral dimensions. In these instances, the surface temperature can be plotted relative to the square root of time. At early times after the flash heating the plot of temperature versus the square root of time is relatively linear. Deviations from linearity frequently indicate the presence of an internal flaw.

Additional methods for performing thermal image analysis by comparison with 1-D and 2-D analytical solutions for simple single layer and multilayer structures has have been studied by many research teams with varying degrees of success.[5-14] Though the details of these efforts varied, of these analytical approaches principally relied on the time-domain characteristics of the measured surface temperatures. The resulting solutions provide varying degrees of accuracy, robustness (to both noise and normal structural inhomogeneities) and computational complexity. However, none of these efforts produced a flaw detection methodology that works for general inspection applications.

Alternative analytical based methods for detecting flaws have investigated different surface heating protocols to optimize the flaw excitation[15,16], use of dual infrared bands to minimize the influence surface artifacts[17], analytical metrics related to bulk thermal properties (e.g., thermal diffusivity[18,19] and thermal inertia[20]), characteristics of the temporal contrast curve[21], and tomographic analysis methods[22-25]. Each of these research efforts has improved flaw detection reliability for some inspection applications by enhancing the flaw visibility, reducing noise, or providing a quantitative basis for evaluating the results. Disadvantages of these methods include increased costs (e.g., more inspection hardware or high end computer processing required), computationally intensive analysis requirements that preclude near-real time inspection results, lack of robustness (inspection application specific), or results that still require interpretation.

The primary objectives of this research effort were to develop a data processing methodology that is tied to the underlying physics, which reduces or removes the data interpretation requirements, and which eliminates the need to look at significant numbers of data frames to determine if a flaw is present. Considering the strengths and weakness of previous research efforts, this research elected to consider both the temporal and spatial attributes of the surface

temperature. As will be shown later, each characteristic exhibits the presence of a flaw. However, optimal inspection performance requires a coupling of the appropriate spatial and temporal parameters. By properly coupling spatial and temporal metrics, we can generate a single synthesized image that highlights any hidden subsurface flaws.

3.2 Conventional Signal-Processing

As presented in section 3.1, signal-processing algorithm development began with an investigation of analytical solutions to the transient heat diffusion equation with impulsive heating. Though analytical solutions rarely exist for inspection problems of interest, they do provide useful trend and thermal characteristics information. Causal predictive filters relying on analytical solutions were investigated as a class of potential flaw detection filters. However, preliminary results demonstrated that in addition to being numerically intensive, causal filters are not sufficiently robust in the presence of the level of spatial and temporal noise and inhomogeneities typically encountered with dynamic thermography. Hence, causal filters were discounted and the algorithm development focused on variants of nonpredictive digital signal-processing (DSP) operators such as the Laplacian, Roberts' cross gradient, Sobel, Kirsch, Prewitt, differential hysteresis, Marr-Hildreth, Frei and Chen, homomorphic, relief, and sequential operators implemented with differing applications of equalization.[26-29]

Figures 6 - 14 display results from the application of some of the investigated DSP operators. These operators were implemented using convolution filters with the kernels specified with each image. The raw image used in each DSP test case is shown in figure 5. The 8 bits used in this 12 bit infrared image were selected based on the image histogram to optimize the flaw visibility for display purposes. As shown in the figure, the image contains one highly visible circular flaw, chalk registration lines to bracket the test area containing the flaw, flaw numbers drawn in chalk (this image contains flaw #8), and a small amount of visible noise. In most instances the noise in this image is high frequency, though there are a handful of relatively large "hot spots" created by surface noise (probably chalk). Some of these large noise spots are pointed out in the image. These large noise spots had significant latency that could have produced a "false" flaw detection. However, in this specific example it was visually apparent that these hot spots were created by chalk on the test specimen surface.

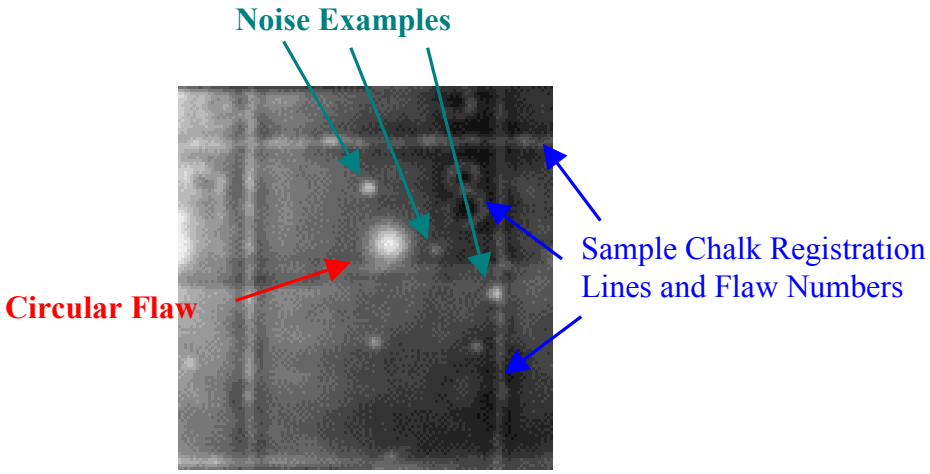

Figure 5. Sample thermal image with contrast enhancement.

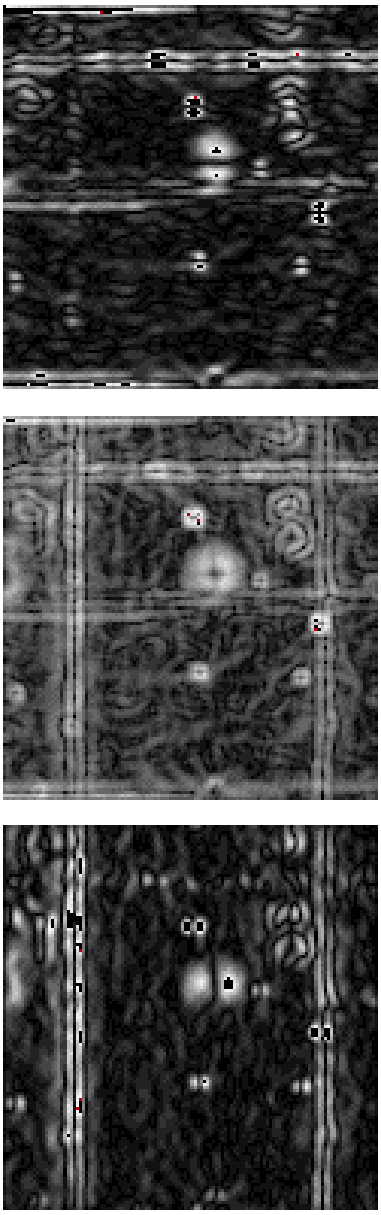

Horizontal Edge Kernel: $\begin{bmatrix} -2 & -2 & -2 \\ 0 & 0 & 0 \\ 2 & 2 & 2 \end{bmatrix}$

Prewitt Edge Kernel:

$$0.5\begin{bmatrix} 1 & 1 & 1 \\ 0 & 0 & 0 \\ -1 & -1 & -1 \end{bmatrix} + 0.5\begin{bmatrix} -1 & 0 & 1 \\ -1 & 0 & 1 \\ -1 & 0 & 1 \end{bmatrix}$$

Vertical Edge Kernel: $\begin{bmatrix} -2 & 0 & 2 \\ -2 & 0 & 2 \\ -2 & 0 & 2 \end{bmatrix}$

Figure 6. Sample results using edge detection filters.

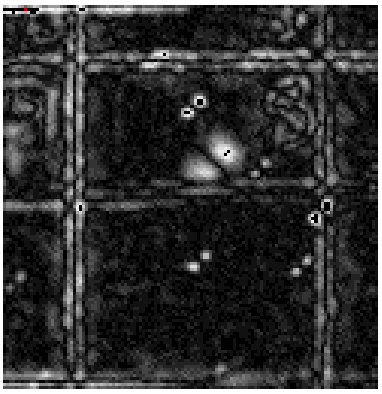

Kernel: $\begin{bmatrix} 0 & -10 & -14 \\ 10 & 0 & -10 \\ 14 & 10 & 0 \end{bmatrix}$

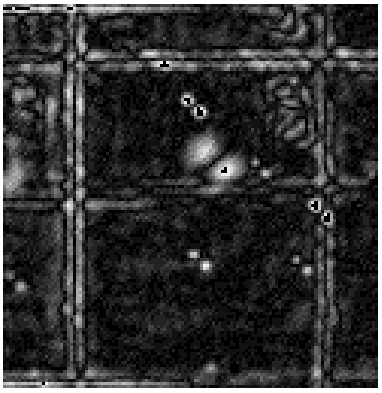

Kernel: $\begin{bmatrix} 14 & 10 & 0 \\ 10 & 0 & -10 \\ 0 & -10 & -14 \end{bmatrix}$

Figure 7. Sample results for diagonal edge detection filters.

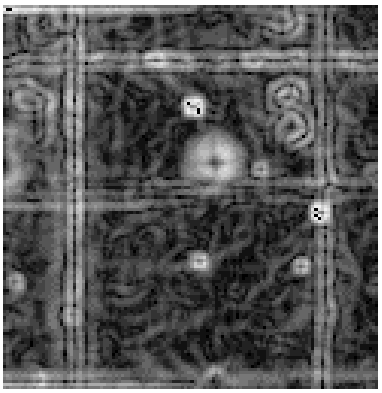

Kernel: $0.5\begin{bmatrix} 1 & 2 & 1 \\ 0 & 0 & 0 \\ -1 & -2 & -1 \end{bmatrix} + 0.5\begin{bmatrix} -1 & 0 & 1 \\ -2 & 0 & 2 \\ -1 & 0 & 1 \end{bmatrix}$

Figure 8. Sample results for a Sobel filter.

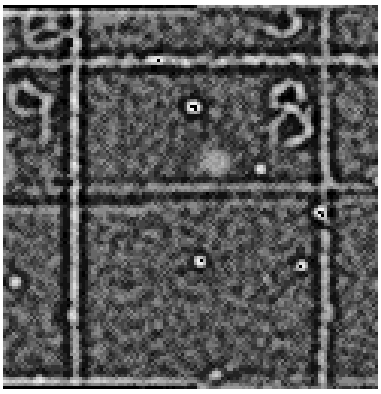

Kernel: $\begin{bmatrix} 0 & -1 & 0 \\ -1 & 4 & -1 \\ 0 & -1 & 0 \end{bmatrix}$

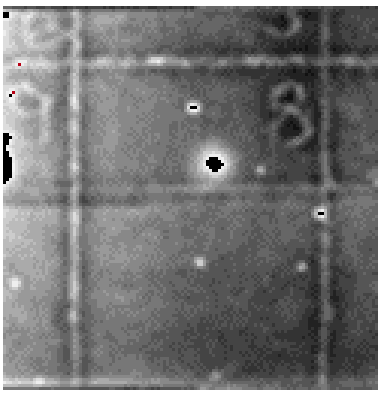

Kernel (with sharpening): $\begin{bmatrix} 0 & -1 & 0 \\ -1 & 5 & -1 \\ 0 & -1 & 0 \end{bmatrix}$

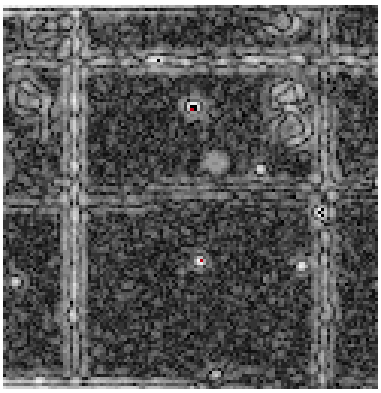

Kernel: $\begin{bmatrix} -1 & -1 & -1 \\ -1 & 8 & -1 \\ -1 & -1 & -1 \end{bmatrix}$

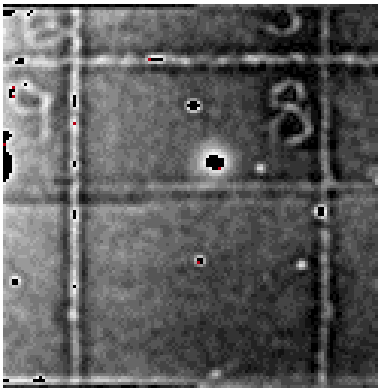

Kernel (with sharpening): $\begin{bmatrix} 0 & -1 & 0 \\ -1 & 9 & -1 \\ 0 & -1 & 0 \end{bmatrix}$

Figure 9. Sample results using Laplace filters.

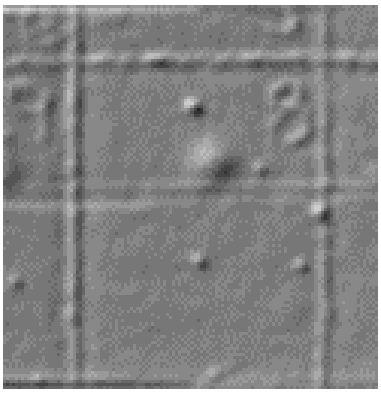

Relief Kernel: $\begin{bmatrix} -1 & 0 & 0 \\ 0 & 0 & 0 \\ 0 & 0 & -1 \end{bmatrix}$

Figure 10. Sample results using a relief filter.

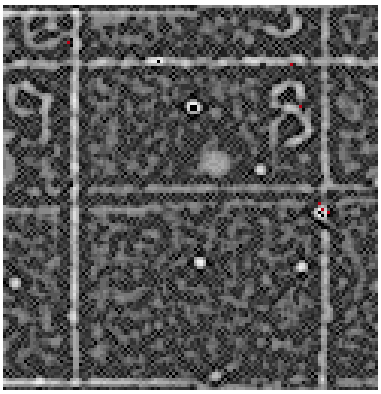

Kernel: Maximum of

$$\begin{bmatrix} 1 & -2 & 1 \\ -2 & 4 & -2 \\ 1 & -2 & 1 \end{bmatrix} \text{ and } \begin{bmatrix} -2 & 1 & -2 \\ 1 & 4 & 1 \\ -2 & 1 & -2 \end{bmatrix}$$

Figure 11. Sample results using a sequential filter.

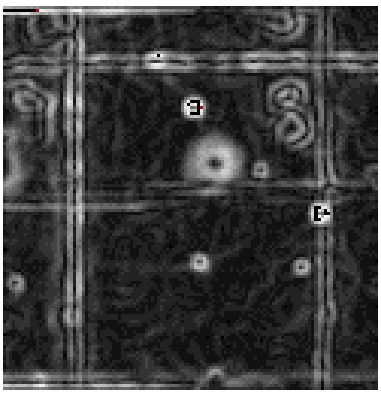

Kernel: Maximum of

$$\begin{bmatrix} 1 & 0 & -1 \\ 2 & 0 & -2 \\ 1 & 0 & -1 \end{bmatrix} \text{ and } \begin{bmatrix} 2 & 1 & 0 \\ 1 & 0 & -1 \\ 0 & -1 & -2 \end{bmatrix}$$

Figure 12. Sample results using a sequential derivative filter.

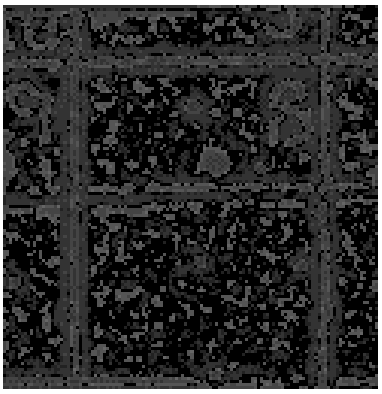

Kernel:

$$\left\{ \begin{bmatrix} 0 & 0 & 0 & 0 & 0 \\ 0 & -1 & -4 & -1 & 0 \\ 0 & -4 & -12 & -4 & 0 \\ 0 & -1 & -4 & -1 & 0 \\ 0 & 0 & 0 & 0 & 0 \end{bmatrix} - \begin{bmatrix} 1 & 2 & 3 & 2 & 1 \\ 2 & 7 & 11 & 7 & 2 \\ 3 & 11 & 17 & 11 & 3 \\ 2 & 7 & 11 & 7 & 2 \\ 1 & 2 & 3 & 2 & 1 \end{bmatrix} \right\} \left(\frac{1}{121} \right)$$

Figure 13. Sample results for a difference of Gaussians filter with Rayleigh equalization.

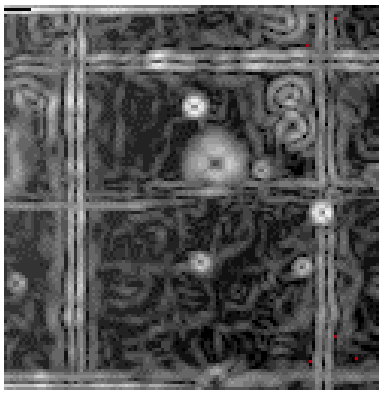

Figure 14. Sample results using a Frei and Chen filter.

The Frei and Chen filter can be implemented using either the maximum from the following 8 kernels or the sum of the results produced by each kernel. In this example the normalized sums were used to produce the image.

$$\left(\frac{1}{9} \right) \begin{bmatrix} 1 & 1 & 1 \\ 1 & 1 & 1 \\ 1 & 1 & 1 \end{bmatrix} \begin{bmatrix} -10 & -14 & -10 \\ 0 & 0 & 0 \\ 10 & 14 & 10 \end{bmatrix} \begin{bmatrix} -10 & 0 & 10 \\ -14 & 0 & 14 \\ -10 & 0 & 10 \end{bmatrix} \begin{bmatrix} 14 & -10 & 10 \\ -10 & 0 & 10 \\ 0 & 10 & -14 \end{bmatrix} \begin{bmatrix} 0 & 1 & 0 \\ -1 & 0 & 1 \\ 0 & -1 & 0 \end{bmatrix} \begin{bmatrix} -1 & 0 & 1 \\ 0 & 0 & 0 \\ 1 & 0 & -1 \end{bmatrix}$$

$$\begin{bmatrix} 1 & -2 & 1 \\ -2 & 4 & -2 \\ 1 & -2 & 1 \end{bmatrix} \begin{bmatrix} -2 & 1 & -2 \\ 1 & 4 & 1 \\ -2 & 1 & -2 \end{bmatrix}$$

As demonstrated in these images, conventional DSP operators have the ability to accentuate the visible flaw, but also have a tendency to highlight the image noise. For example, the spatial Laplacian is an indiscriminate edge detector that can highlight the flaw, chalk edges,

and high frequency noise sources. Though other filters may have edge detection advantages, the detected edges may not be true flaws. Instead they may represent surface features (emissivity variations), heating nonuniformities (though these should be relatively smooth), material variations (e.g., steel vs. aluminum), or other artifacts. This reinforces the need to consider both the spatial and temporal effects. However, coupling spatial and temporal data still requires an effective method for reducing the image noise without significantly reducing the flaw induced effects.

3.3 Parametric Model for Spatio-Temporal Smoothing of Image Data

This section describes a statistical method for the estimation of parameters in a simple model to filter infrared image data prior to analysis. As discussed in section 2.1, infrared images collected during the inspection of a structure are noisy. For our purposes, the image noise includes both an image dependent multiplicative component (e.g., emissivity variations) and a random additive component (optical system and thermal noise). The multiplicative component will be addressed in section 4.3. In this section we will focus on the random spatial and temporal noise.

Conventional blind smoothing noise filters such as low pass filters, spatial averaging, directional averaging, and median filters are not well suited to our problem. These approaches are typically designed for image enhancement (accentuate or extract specific image features) rather than image restoration (removal of the noise without signal degradation). Since the flaw detection algorithms (section 4) compute image derivatives to detect anomalies, it is important to use a digital filter that preserves the proper higher order moments. Therefore, it is useful to fit the spatial and temporal image data to a smooth parametric model of the appropriate order to remove noise artifacts.

The first moment preserving filter considered was the Savitzky-Golay smoothing filter.[2,30] This filter applies an unbiased moving window procedure with filter coefficients that preserve the desired moments. Specifically, the underlying image data is least-squares fit with a polynomial of the desired order. Since the process is linear, we can pre-compute the filter coefficients that perform the polynomial least-squares fitting and then quickly apply the filter to each image using a convolution. This approach is straightforward to implement and is computationally tractable. However, the challenge is to select the appropriate filter order and width. Typically a second order filter is adequate for infrared inspection images, but the filter width is more subjective and data dependent. Increasing the filter width improves the noise reduction, but at the expense of high frequency features. Care must be exercised to ensure that the filter width is smaller than the narrowest real image feature (i.e., flaw size) of interest or low contrast high frequency flaw data may be smoothed beyond detection. Sample results from the application of Savitzky-Golay filters are provided in section 4.1.

Though Savitzky-Golay filters are computationally efficient, an alternative parametric model was considered that provided more flexibility in the investigation of weighting alternatives and mixed component image derivatives. The method selected to populate the parametric model is the least square identification of the parameters in a spatio-temporal polynomial model with temporal weighting. Image data from spatially and temporally local regions are

used to identify the parameters of the local model. Then spatial and temporal image values and image derivatives are estimated using the model parameters and the general model form instead of the raw image data. These model values are used in turn to evaluate estimates of quantities that depend on these values and derivatives, such as the image Laplacian at a point. Consistent with the digitized infrared images, it is assumed that image data are available at discrete locations on a rectangular grid, with equal spacing in each coordinate axis, and at many equally spaced times. The data are denoted:

$$(11) \qquad T\left(x_i, y_j, t_k\right), i = 0,...,n_x - 1, j = 0,...,n_y - 1, k = 0,...,n_t - 1,$$

where,

$$(12) \qquad \begin{aligned} x_i &= x_0 + i\Delta x & i &= 0,...,n_x - 1 \\ y_j &= y_0 + j\Delta y & j &= 0,...,n_y - 1 \\ t_k &= t_0 + k\Delta t & k &= 0,...,n_t - 1 \end{aligned},$$

and n_x is the number of points measured in the *x*-direction, n_y is the number of points measured in the *y*-direction, and n_t is the number of time steps measured.

The parametric model chosen to fit the data is spatially quadratic in the *x* and *y* coordinates and temporally quadratic. Though the surface cooling is exponential in character, over small temporal windows it is well fit by a quadratic relation. Also, the temporal quadratic relation is more computational efficient than an exponential relation . The model has the form:

$$(13) \qquad \begin{aligned} g(x,y,t) = &\left(c_{00}^{(0)} + c_{00}^{(1)}t + c_{00}^{(2)}t^2\right) + \left(c_{10}^{(0)} + c_{10}^{(1)}t + c_{10}^{(2)}t^2\right)x \\ &+ \left(c_{01}^{(0)} + c_{01}^{(1)}t + c_{01}^{(2)}t^2\right)y + \left(c_{20}^{(0)} + c_{20}^{(1)}t + c_{20}^{(2)}t^2\right)x^2 \\ &+ \left(c_{11}^{(0)} + c_{11}^{(1)}t + c_{11}^{(2)}t^2\right)xy + \left(c_{02}^{(0)} + c_{02}^{(1)}t + c_{02}^{(2)}t^2\right)y^2 \end{aligned}$$

The model contains 18 parameters that can be identified using a least squares approach. In particular, the parameters are computed using a least squares approach with temporal weighting. To start, parameter identification is performed by rewriting equation (13) in vector form:

$$(14) \qquad (\boldsymbol{A})\boldsymbol{p} = g$$

where $(\boldsymbol{A})$ is the row vector of times and spatial locations defined:

$$(15) \qquad \begin{aligned} (\boldsymbol{A}) = \big(&1 \quad t \quad t^2 \quad x \quad tx \quad t^2x \quad y \quad ty \quad t^2y \quad ... \\ &x^2 \quad tx^2 \quad t^2x^2 \quad xy \quad txy \quad t^2xy \quad y^2 \quad ty^2 \quad t^2y^2\big) \end{aligned}$$

$\boldsymbol{p}$ is the parameter vector defined:

$$\boldsymbol{p} = \left(c_{00}^{(0)} \quad c_{00}^{(1)} \quad c_{00}^{(2)} \quad c_{10}^{(0)} \quad c_{10}^{(1)} \quad c_{10}^{(2)} \quad c_{01}^{(0)} \quad c_{01}^{(1)} \quad c_{01}^{(2)} \quad \ldots \right.$$
$$\left. c_{20}^{(0)} \quad c_{20}^{(1)} \quad c_{20}^{(2)} \quad c_{11}^{(0)} \quad c_{11}^{(1)} \quad c_{11}^{(2)} \quad c_{02}^{(0)} \quad c_{02}^{(1)} \quad c_{02}^{(2)} \right)^T \tag{16}$$

and g denotes the scalar on the left-hand side of equation (13).
There are eighteen parameters in the model of equation (13). Hence, at least eighteen realizations of equation (14) must be written to solve for the parameters. Since there are six coefficients corresponding to each power of the temporal term, at least six measurements at six physically independent locations must be made at each time step. Further, since the model involves temporal terms up to the quadratic level, measurements are required at three or more times step. Therefore, to perform least squares identification of the model parameters (and thereby smooth over the effects of measurement noise) more than eighteen total data points are required using six or more image pixels at each time step (image frame), and with three or more times steps measured.

We seek to perform an identification of model parameters in a spatial/temporal region that is a contiguous segment of the entire collection of data specified by equation (11). To perform a simple least squares identification of the model parameters, we first create a coefficient matrix $\boldsymbol{A}$, each row of which is a realization of equation (15) for a particular time and x-y location. Because the model is intended to characterize image data, there exists a column vector $\boldsymbol{T}$ with elements corresponding to the rows of $\boldsymbol{A}$, that is the image grayscale measured at the appropriate locations and times. Both $\boldsymbol{A}$ and $\boldsymbol{T}$ contain N rows, with $N \le n_t$. The duration $N\Delta t$ is the time segment over which the data are to be modeled with equation (13). For practical purposes, we might choose N in the interval [5,25]; this will be discussed further, later. During a given parameter identification, the system might be modeled at the times $\left(t_s, t_{s+1}, \ldots, t_{s+N-1}\right)$. The model specifies that:

$$\boldsymbol{A}\boldsymbol{p} = \boldsymbol{T} \tag{17}$$

If the images were entirely noise free, and if the phenomenon being measured was suitably modeled as the spatio-temporal trivariate quadratic of equation (13), then the parameters $\boldsymbol{p}$ could be identified precisely, and the model used to predict the grayscales which are related to surface temperature. However, the images are not noise-free, and it is anticipated that the trivariate quadratic model is only an appropriate model for system behavior in a local sense. In view of this, equation (17) is solved in a least squares sense. To accomplish this, the pseudo-inverse of the coefficient matrix $\boldsymbol{A}$ is evaluated via singular value decomposition (SVD), and used to express $\boldsymbol{p}$:

$$\boldsymbol{p} = \boldsymbol{A}^{+}\boldsymbol{T} \tag{18}$$

where $\boldsymbol{A}^{+}$ denotes the pseudo-inverse of the coefficient matrix $\boldsymbol{A}$. The parameters so-obtained, and used in equation (13), can be taken as representative of the system behavior in the space/time prism represented by the data, but are usually only taken to represent system behavior at the central value of the independent variables, i.e.:

$$(19) \qquad x = x_{0.5(n_x+1)} \qquad y = y_{0.5(n_y+1)} \qquad t = t_{0.5(2s+n_t-1)}$$

[Recall that the model parameters have been identified using data measured at times $(t_s, t_{s+1}, ..., t_{s+N-1})$.]

Weighted least squares estimation is accomplished by applying a weighting to the factors in equation (17). Specifically, to emphasize the measurements near the temporal mid-point in the identification of the model parameters requires a weighting that diminishes the influence of measured values away from the central time. For example, the nonnegative weighting function defined by:

$$(20) \qquad w(t) = exp\left(-\frac{1}{2t_\sigma^2}(t - t_c)^2 \right)$$

applies a weight near one for values of *t* near t_c, and a diminished weight for values of *t* far from t_c (as determined by the weighting width scale factor, t_σ). To perform weighted least squares analysis, the factors on both sides of equation (17) are weighted. To accomplish this, the following diagonal weighting matrix is created:

$$(21) \qquad \boldsymbol{W} = \begin{bmatrix} w(t_s)\boldsymbol{I}_{(n_x n_y)\times(n_x n_y)} & \boldsymbol{0} & \cdots & \boldsymbol{0} \\ \boldsymbol{0} & w(t_{s+1})\boldsymbol{I}_{(n_x n_y)\times(n_x n_y)} & \cdots & \boldsymbol{0} \\ \vdots & \vdots & \ddots & \vdots \\ \boldsymbol{0} & \boldsymbol{0} & \cdots & w(t_{s+N-1})\boldsymbol{I}_{(n_x n_y)\times(n_x n_y)} \end{bmatrix},$$

where $\boldsymbol{I}_{(n_x n_y)\times(n_x n_y)}$ is the identity matrix with dimension $(n_x n_y)\times(n_x n_y)$. This is a diagonal matrix with dimension $(n_x n_y N)\times(n_x n_y N)$, and with the weights of equation (20) repeated along the diagonal *N* times in groups of size $n_x n_y$. Each side of equation (17) is weighted with the square root of $\boldsymbol{W}$:

$$(22) \qquad \boldsymbol{W}^{1/2}\boldsymbol{A}\boldsymbol{p} = \boldsymbol{W}^{1/2}\boldsymbol{T}$$

The parameters are estimated by computing the pseudo-inverse of the coefficient matrix, $\boldsymbol{W}^{1/2}\boldsymbol{A}$, then premultiplying both sides of the expression by this coefficient matrix. The parameters are:

$$(23) \qquad \boldsymbol{p} = \left(\boldsymbol{W}^{1/2}\boldsymbol{A}\right)^{+}\boldsymbol{W}^{1/2}\boldsymbol{T}$$

The 18 parameters in $\boldsymbol{p}$ characterize the model for the data in the form of equation (13), in a weighted least squares sense. As stated previously, if the phenomenon actually resembles the

trivariate quadratic of equation (13), then there is a strong potential for the error of representation to be low. However, the error is not guaranteed low. If the noise contained in the measurements is great, then the error will, on average, be large. Further, this approach to parameter identification works best when the noise samples are uncorrelated, spatially and temporally. When the spatial and/or temporal noise variation is not uncorrelated, then a statistical bias may appear in the parameter estimates. That is, the correlated noise may be misinterpreted as a feature of the system and reflected in the estimates of the parameters, $\boldsymbol{p}$.

On the other hand, if the noise samples are uncorrelated then the procedure yields asymptotically unbiased and statistically consistent estimates of the parameters. This means, in essence, that as n_x, n_y, and N increase, the parameter estimates converge, in a statistical sense, to the correct (but unknown) values. Further, if the noise samples are uncorrelated and come from a random source governed by a Gaussian distribution, then the parameter estimators are random variables with a multivariate, Student t sampling distribution. This indicates that, in principle, confidence intervals on the model parameters could be approximated. This may, however, be quite difficult in practice.

A practical issue in application of the present procedure is the choice of the value of N, the number of time slices of data used to estimate the model parameters. When N is small the coefficient matrix on the left side in equation (22), $\boldsymbol{W}^{1/2}\boldsymbol{A}$, is small, and computation of its SVD proceeds rapidly. (Recall that on the order of $n_x n_y n_t$ separate models must be identified.) When the matrix $\boldsymbol{A}$ has dimensions $N \times m$, the SVD computation takes on the order of Nm^2 computations. The value of N is linearly related to the number of rows in $\boldsymbol{A}$. Therefore, it is clear why the above statement is true. The minimum value for N is three.

As N increases computation time increases, but the potential for smoothing out temporal noise improves. The standard error of the parameter estimates (i.e., the standard deviations of the random variables that are the sources of the parameter estimates) decreases as $N^{-1/2}$. This would seem to indicate that N should be very large. However, the spatio-temporal polynomial of equation (13) is only an approximation to the behavior of the actual system. When N becomes too great there is the possibility that the temporal quadratic of the model will fail to suitably fit the measured data and short duration flaw induced anomalies will be smoothed to the point where they are undetectable. This indicates that N should be kept below some (unknown) limit. These factors must be weighed in selection of N, and the experience of the data analyst must be tapped. We suggest that N be chosen from the interval [5,25] depending on the camera frame rate and the amount of temporal noise. In summary, for the model of equation (13) to accurately capture real system behavior over a time period of $N\Delta t$, the real system behavior over that time period must actually appear quadratic. In practice, the real system follows an approximately exponential decay. However, for short durations the quadratic expression provides a good estimate of this exponential behavior.

The same general comments apply to the choice of the measurement parameters n_x and n_y. Making these values large increases computation time and introduces the potential for noise

smoothing. The quantities $n_x \Delta x$ and $n_y \Delta y$ should not be chosen so large that the spatial temperature variation in the actual system cannot appear quadratic. Typically this is not a problem because the inspection surface is heated in a quasi-uniform manner. Deviations from quadratic behavior are expected near areas with significant emissivity variations (e.g., a different material or surface finish) or significant temperature differences (e.g., above a hidden flaw). The overall intent is to detect these anomalous regions that deviate from quadratic behavior. Care should be taken to ensure that the quantities $n_x \Delta x$ and $n_y \Delta y$ are not so large that they smooth flaw data beyond the point of detection. A 3x3 spatial window will minimize flaw smoothing, but also minimize the noise reduction. As such, it is recommended that the spatial window be at least 5x5. Larger windows should be considered is the spatial noise is very strong and the 5x5 window does not adequately reduce the noise.

The weighted least squares approach used here to identify the parameters of the model, $\boldsymbol{p}$, has very good potential to arrive at parameter estimates that accurately simulate real system behavior if the parameters used in the identification process are chosen appropriately. Indeed, the performance of the model can be evaluated for any given data prism by estimating the root mean square (RMS) error of the representation. Using the notation of equation (17) this error is:

$$\varepsilon = \left[\frac{1}{N n_x n_y} (\boldsymbol{T} - \boldsymbol{A}\boldsymbol{p})(\boldsymbol{T} - \boldsymbol{A}\boldsymbol{p})^T \right]. \tag{24}$$

This error is, of course, a function of the identification parameters, n_x, n_y, N and t_σ. The estimation algorithm defined here could be made adaptive by minimizing ε during the identification of parameters of each prism of data, with respect to n_x, n_y, N and t_σ. Of course, this would require the performance of an optimization in four dimensional grid (discrete) space for each of about $n_x n_y n_t$ data prisms. However, this would involve a very substantial development effort that is beyond the scope of this effort.

As will be shown in section 4.2, the weighted least-squares parametric model successfully provides image metrics that highlight the presence of hidden flaws. However, the principal disadvantage of the parametric model as implemented is the time it takes to perform the calculations. Future work should convert the developed model into a convolution based digital filter that computes the 3-D (x, y, t) weighted filter coefficients consistent with the selected parametric model.

4.0 DATA ANALYSIS RESULTS

The thermal inspection system infrared camera measures the signal emitted from the surface as a function of time. This signal is directly related to the surface temperature T(x,y,t). From an evaluation of the heat diffusion equation and experimental results we were able to identify two measurable metrics for highlighting the presence of internal structural defects. Both the time rate of change of the internal energy and the net lateral conduction heat flux along the

surface highlight the presence of internal flaws. Methods for coupling these metrics were investigated to improve flaw detection sensitivity.

The temperature rises very quickly (almost instantaneously) after the flash and then decays in a relatively exponential manner. To first order the decay should follow an exponential decay at a rate governed by the local material properties. Though adjacent regions with different properties will decay at different rates, the decays should be relatively smooth unless lateral diffusion becomes significant. This lateral diffusion can be due to significantly different thermal diffusivities, differing material thicknesses, or internal flaws. When this occurs there is often a detectable spatial and temporal change in the image temperature field. Further, in some instances an internal flaw may induce two significant slope changes in the exponential decay.

4.1 Energy Balance Metric

From energy conservation, in the absence of internal energy generation the rate of energy transfer into a control volume minus the energy transfer out of a control volume equals the energy stored. As such, if the transient energy storage can be measured with an infrared camera it may be a potential indicator of the presence of an obstruction to energy transport as heat or the presence of a heat sink.

The governing differential equation for transient diffusion shows that the time rate of change of internal energy is balanced by the net lateral conduction heat flux along the surface. Since the infrared camera rapidly (up to 1000 images per second) measures the surface radiance over time, it may be possible to estimate both the lateral conduction (image spatial Laplacian) and change in internal energy (first derivative with respect to time) near the surface.

In principal, an internal flaw should perturb the flow of heat into the specimen. If the transient diffusion equation is rearranged, it would appear that the difference in the time rate of change of internal energy and the net lateral conduction heat flux along the surface could be monitored as a possible metric for detecting flaws.

$$\frac{\partial^2 T}{\partial z^2} = \frac{1}{\alpha}\frac{\partial T}{\partial t} - \frac{\partial^2 T}{\partial x^2} - \frac{\partial^2 T}{\partial y^2}. \tag{25}$$

The challenge in applying this approach is determining the thermal diffusivity $\forall$.

Thermal diffusivity is typically measured using the laser flash method.[31] Here the front surface of the material is impulsively heated with a laser pulse while an infrared camera temporally measures the heat rise on the back surface. The diffusivity is determined using the formula $\alpha = \frac{0.1388\, d^2}{t_{1/2}}$, where d is the sample thickness and t is the time from the pulse initiation for the back surface to reach one half its maximum temperature. Since its development, many corrections have been introduced to this relation to account for radiative

heat losses, the laser pulse finite width, non-uniform heating of the sample, and other related experimental factors.[32-40] However, the remaining practical limitations to this approach are that the measurements are one-dimensional and require simultaneous access to both the front and back surface.

A recently developed method for overcoming the 1-D measurement limitation was demonstrated by Wayne State University.[41] Their technique applies a one-dimensional plane wave thermal pulse to the front surface and temporally images the lateral blurring of a straight-edge or corner shadow on the back side of the structure in an area which is far from the shadow region. This technique has demonstrated the ability to accurately measure thermal diffusivity in isotropic materials and to measure the three orthogonal diffusivities for a uniaxial graphite-fiber-reinforced laminated polymer composite slab. However, as with the laser flash method, measuring diffusivity using infrared imaging of the thermally blurred shadows still requires simultaneous access to the front and back surfaces of the specimen being measured.

Diffusivity measurement methods that require access to both the front and back surface of a structure are impractical for most general inspection processes. Further, many structures contain multiple types of materials and layered elements that compound the diffusivity measurements. This complexity, together with the added measurement and analysis time makes accurate diffusivity measurements impractical for the general flaw detection applications. However, since the intent is to detect anomalous thermal behavior induced by internal flaws, it may be adequate to select an approximate value to use in equation (25) that would normalize the result in a manner that would highlight flaw induced deviations. For example, $\forall$ could be arbitrarily selected to minimize equation (25) for the first 5 image frames. Though this would not be a good estimate for $\forall$ since the flow of heat into the structure is large immediately following the flash heating, it might be sufficient as a parameter normalization method.

Strictly speaking, the infrared camera does not measure temperature. Though radiometric cameras that estimate temperature given a user specified surface emissivity are commercially available, the camera used in this research was nonradiometric. As such, computing $\frac{\partial^2 T}{\partial z^2}$ may require that the image grayscales be converted into temperatures.

Considering the camera waveband and the temperature of interest, $e^{\frac{hc}{\lambda kt}} >> 1$ in the exitance expression (equation 2). Hence, if we consider the spectral exitance and rearrange the equation for incident photon flux density we can express the surface temperature in terms of the flux density E_d. This allows the temperature to be approximated by the following relations for the single wavelengths of 3, 4, and 5 microns (high sensitivity region):

5 microns: $T = 2877.5724/\ln(1.7929e18/E_d)$
4 microns: $T = 3596.9655/\ln(4.3772e18/E_d)$
3 microns: $T = 4795.9541/\ln(1.3834e19/E_d)$

It is apparent that T . $C_1/\ln(C_2/E_d)$ if the temperature estimate is based on a single wavelength rather than the integration of the exitance over the full waveband. To apply this approximation, the image grayscales must be converted into E_d (photons/cm^2-sec) using equation (4).

4.2 Flaw Detection Results Using Finite Element Data

Consideration of the energy balance provided in section 4.1 suggests that the presence of a flaw may be highlighted by comparing the difference between the time rate of change of internal energy and the net lateral conduction heat flux along the surface. However, as discussed previously, this requires an estimate of the thermal diffusivity and conversion of the image grayscales to surface temperatures. An alternative approach considered in this section evaluates the temporal and spatial energy transport components separately.

The presence of a flaw changes both the local cooling rate and lateral diffusion rate if the flaw impedes (traps, delays, or stores energy) or facilitates energy conduction. As such, it is logical to expect that both the time derivative and the spatial Laplacian of the surface temperature distribution might highlight the presence of an internal flaw. However, as discussed in earlier sections, image noise can inhibit flaw detection. This is particularly true using metrics that involve image differentiation because numerical derivatives tend to accentuate noise.

To minimize the impact of temporal and spatial noise, two steps were used to produce the results presented in this section. First, all derivatives were computed using a Savitzky-Golay smoothing and differentiation filter that preserves the second moment. Second, the processed results from individual image frames were summed to enhance the flaw effects. Temporal image noise is a zero mean random process that tends to average out when images are summed. However, flaws induce temperature deviations that have a degree of latency governed by their size and thermal properties. As such, if the processed individual frame results are summed and normalized, a single image can be generated that principally contains features that have a higher probability of representing flaw characteristics than noise.

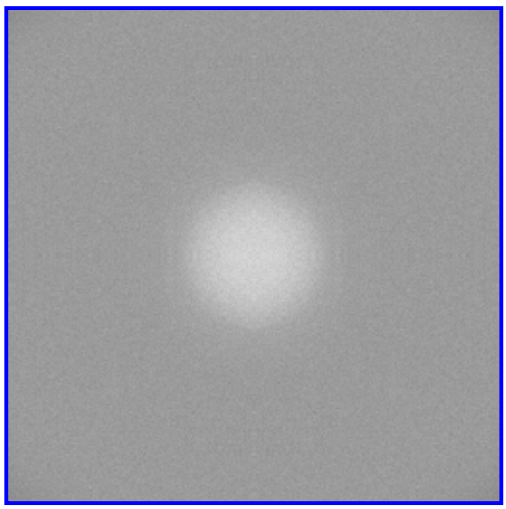

Further, summing the results from individual frames significantly improves the signal to

noise ratio, making small flaw detection more probable. For example, a single processed image frame may contain a flaw indication that has a small signal to noise ratio or a barely detectable grayscale. However, this low signal strength can be dramatically amplified if the processed flaw has reasonable latency.

Figure 15. Simulated thermal image of an aluminum plate with a flat bottom hole.

Figure 15 displays a single image frame created using finite element data from section 2.4.1 (largest flaw) and the thermal imaging model presented in section 2.2. This data simulates data acquired at 500 frames per second for a 256 x 256 focal plane array camera sensitive in the 3-5 micron waveband. The images represent simulated inspection data for a 60 mil aluminum plate with a 10 mil deep flat bottom hole on the backside of the plate. Since the flaw location for this simulated data is known a priori, the grayscales have been adjusted in this image to maximize the flaw visibility for display purposes. However, all analysis in this section was performed on the raw data.

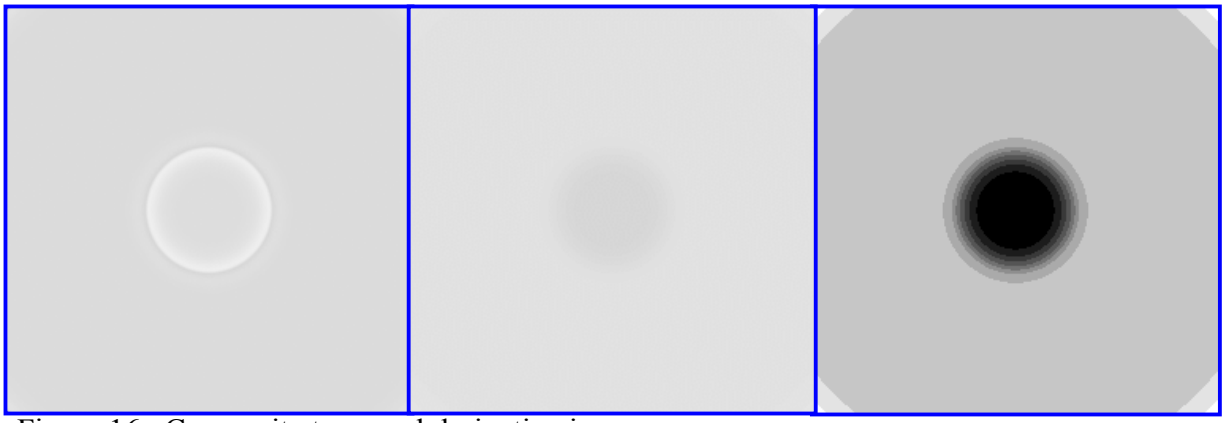

Figure 16. Composite temporal derivative images.

Figure 16 presents image results that were generated on the same finite element data set that produced figure 15. These images were created using the following relation with 256 image frames:

$$\sum_{i=1}^{i=\#\ of\ frames} \frac{\partial Gray(x,y,t)}{\partial t}. \tag{26}$$

The left image in figure 16 sums the temporal derivative of the image grayscales Gray(x,y,t). The center image and image on the right sum the derivatives of [-1/ln Gray(x,y,t)] as a function of time. The right image was produced by level equalization of the center image to increase the flaw visibility. The logarithmic relationship is an approximate conversion of the image grayscales to temperature as discussed in section 4.1. The constants in the relations provided in section 4.1 did not appear to significantly affect the flaw visibility, so they were ignored. As shown in figure 16, the flaw alters the cooling rate enough to highlight the flaw, though the visibility is marginal except where histogram equalization was performed. Also, converting the grayscales into an approximate temperature did not improve the flaw detection. In fact, it actually reduced the visibility.

The goal of the impulsive surface heating is to impart a planar heat wave onto the surface. If the energy is uniformly coupled into the surface, in the absence of noise the surface temperature will remain spatially uniform until lateral diffusion becomes significant. As such, the second derivative of the images should equal zero until lateral conduction variations are created. Under these conditions, the image Laplacian should produce high visibility evidence of an internal flaw. Figure 17 presents image results for a Laplacian operation using the following relation on 256 image frames:

$$(27) \qquad \sum_{i=1}^{i=\#\ of\ frames} \frac{\partial^2 Gray(x,y,t)}{\partial x^2} + \frac{\partial^2 Gray(x,y,t)}{\partial y^2}.$$

These images were generated from the same finite element data set that produced figure 15. The left image displays the results for the "noise free" case. The center image displays the result of using equation (27) when temporal noise was added to the simulated data set. The right image displays the result of applying level equalization to the center image. The image noise for each image frame was generated using equation (5) with $\sigma M_{noise} = 0.001 T_{fe}$.

The black region inside the white rings in figure 17 overlaps the hidden flaw edge. As shown in these images, the spatial Laplacian is effective in highlighting the flaw edge in the synthetic data. In general, the Laplacian operator has the advantage of being rotation invariant and suppresses uniform and slowly varying image features. As such, linear variations due to heating nonuniformities do not adversely affect the flaw detection. However, the principal disadvantage of the Laplacian is that as a high pass filter it tends to accentuate the high frequency noise more significantly than the flaw's thermal edges. The summation process tended to reduce the impact of the zero mean temporal noise, but it may not be as effective on quasi-static spatial noise. Also, the Laplacian operation creates double edges adjacent to the actual feature edge, though this typically is not a significant concern because the actual edge location can be determined using the zero-crossing property of the Laplacian operator.

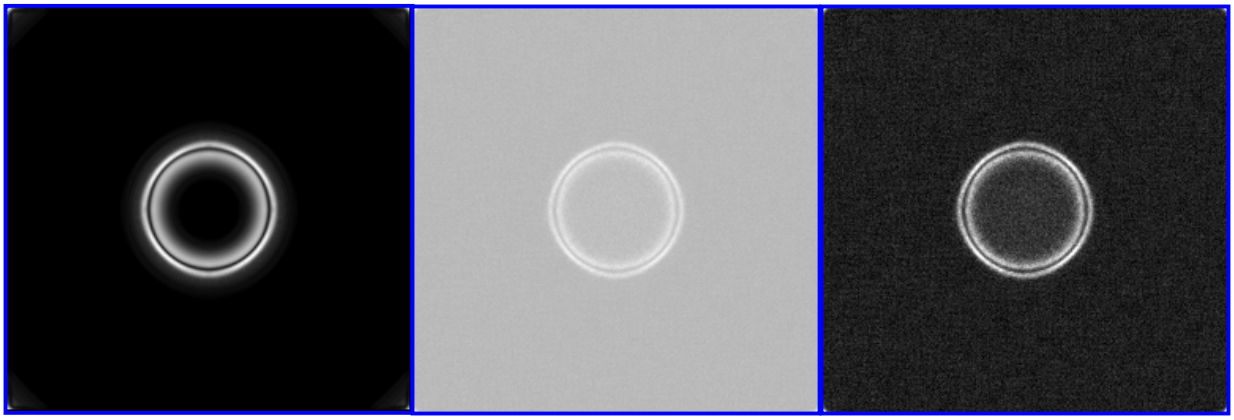

Figure 17. Composite Laplacian images using grayscale data.

Figure 18 displays the image generated using the following relation on 256 image frames:

$$(28) \qquad \sum_{i=1}^{i=\#\ of\ frames} \frac{\partial^2 T}{\partial x^2} + \frac{\partial^2 T}{\partial y^2}$$

where T is approximately equal to -1/[ln Gray(x,y,t)]. As with the previous results, this image was generated using the same finite element data set that produced figure 15.

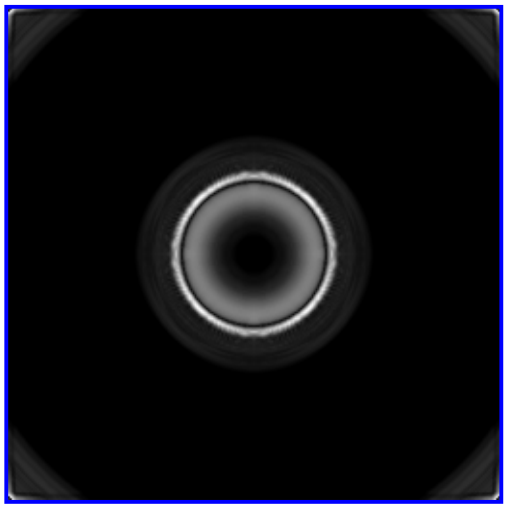

Figure 18. Composite Laplacian image using approximate temperature data.

As shown in figure 18, the application of equation (28) produces a composite image that displays evidence of the hidden flaw. However, as demonstrated in figure 17, the results are not as clear as those produced by equation (27). As such, there appears to be no advantage to trying to convert the grayscale images into a temporal surface temperature map.

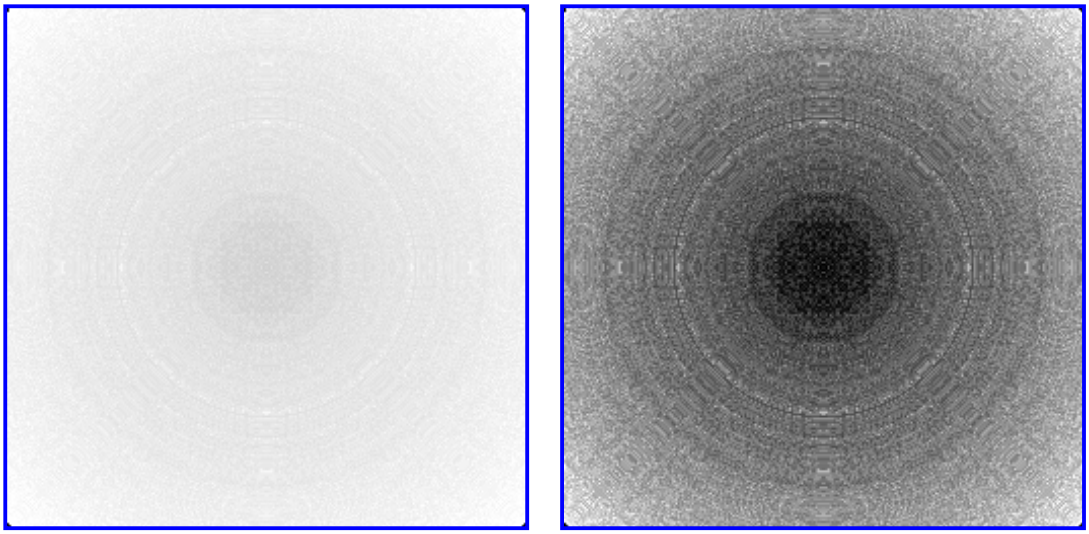

Figure 19. Composite Laplacian image for a painted specimen.

Figure 19 displays the composite image produced by the application of equation (27) to simulated noise free data for a 60 mil aluminum with flat bottom hole on the back side and a 10 mil paint layer on the front surface. The left image presents the direct result from equation (27) and the right image provides the results after the left image was level equalized. As shown in the images, there is very little if any clear evidence that the flaw is present. This simulated results suggests that the paint's thermal thickness and heat capacity prevents the trapped energy from creating a detectable temperature variation on the specimen surface. However, as presented in section 2.4.3, even in the presence of the 10 mil paint

layer, the underlying flaw should generate a temperature variation over the flaw that is within the camera's sensitivity limit. As such, the problem may be that the Laplacian operator is not appropriate for use with painted test specimens.

Figure 20 compares the application of equation (27) to the data set used to produce figure 15 and to an equivalent case where the simulated flaw was a hemispherically shaped backside hole instead of a flat bottom hole. The image on the left displays the hemispherical flaw results and the image on the right displays the flat bottom hole results. Though there are subtle differences in the results, the images suggest that a smooth transition from the structure to the flaw may still be detectable. This is consistent with the flaw induced temperature rise results presented in section 2.4.4. Though the hemispherical flaw is not as efficient at trapping energy as a flat bottom hole, it still induces a detectable temperature rise.

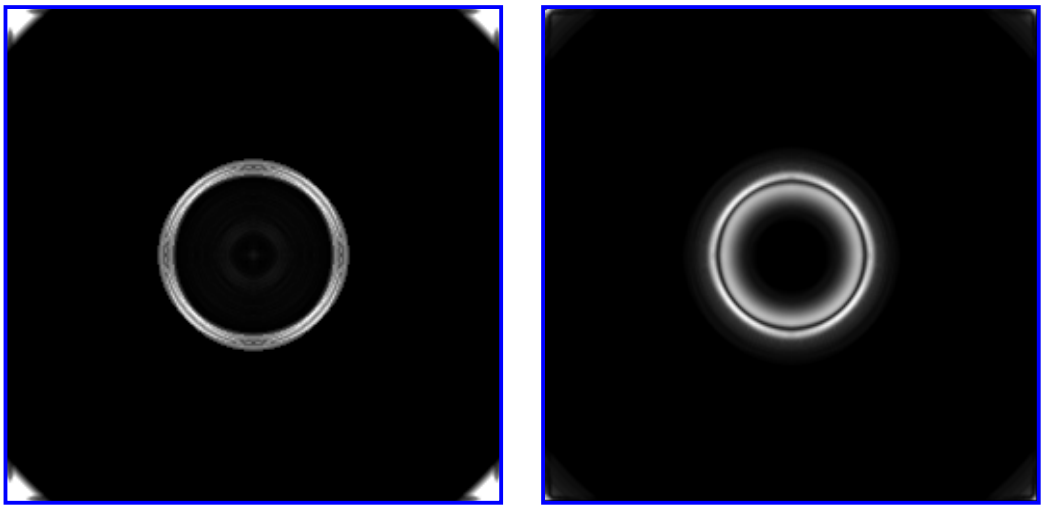

Figure 20. Composite Laplacian images for hemispherical and flat bottom holes.

Figure 21 displays a sample result for an adhesive disbond. This results was created using equation (27) and 256 image frames. Though the flaw is detectable, lateral diffusion affects are less than the test cases with flat bottom hole specimens because the adjacent region containing Cytec adhesive has a conductivity that is two orders of magnitude smaller than aluminum. As a result, the adhesive is not as effective at conducting the energy away. However, the adhesive disbonds did tend to have greater latency than the corresponding flat bottom holes. As a result, though the diffusive effects were lower, the disbond visibility was very high.

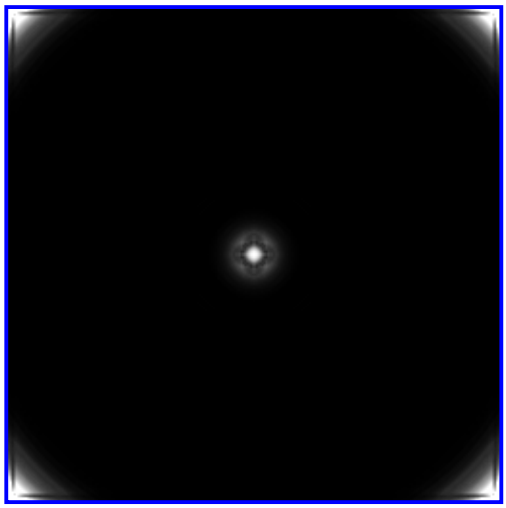

Figure 21. Composite Laplacian image for a simulated adhesive disbond.

The results presented in this section demonstrate that signal processing can significantly enhance and highlight the presence of hidden flaws. Though the results from only a few test cases were displayed, all of the modeled cases presented in section 2.4 were evaluated. This evaluation of simulated inspection data suggests that flaw diameters as small as 0.125" may be detectable, even when temporal noise is significant. However, the flaw detectability drops significantly with increasing paint thickness. For the simulated inspection results the flaws became virtually undetectable when the paint thickness reached 10 mils. Experimental results corresponding to the simulated test cases are presented in the next section.

4.3 Flaw Detection Results Using Experimental Data

Section 4.2 presented sample results for simulated data. In this section experimental results are provided for aluminum plates with machined flat bottom holes and for boron-epoxy composite test specimens. The machined flaws had aspect ratios (ratio of lateral size to depth from surface) from 0.5 to 20, and data acquisition speeds from 60 Hz to 476 Hz. In each test chalk lines were drawn on the specimen surface to provide a significant spatial noise source and to act as registration points. As will be shown in the results provided, spatial noise proved to be a much more significant impediment to flaw detection than temporal noise.

Consistent with the analysis of the simulated test data in section 4.2, the initial evaluation of the experimental data focused on the use of equations (26) and (27). The summation of the temporal derivatives did highlight the flaws, though the signal to noise ratio was typically low. Generally the surface chalk artifacts overwhelmed the flaws in signal strength. Though the Laplacian image (equation 27) highlighted the flaws, it also highlighted a significant amount of spatial noise or structural details not related to the flaw. For example, a test case was run on an F-15 rudder specimen. The rudder specimen consists of 8 plies of boron epoxy composite skin over aluminum honeycomb (0.25" cell size). Interply delaminations and disbonds were placed in the specimen at the locations shown in figure 22. The delaminations were created with grafoil inserts and the disbonds were created with pull-tabs. Each flaw (represented by different color) was placed at a different depth and some flaws overlapped to determine if the presence of a near surface flaw would hide a deeper flaw.

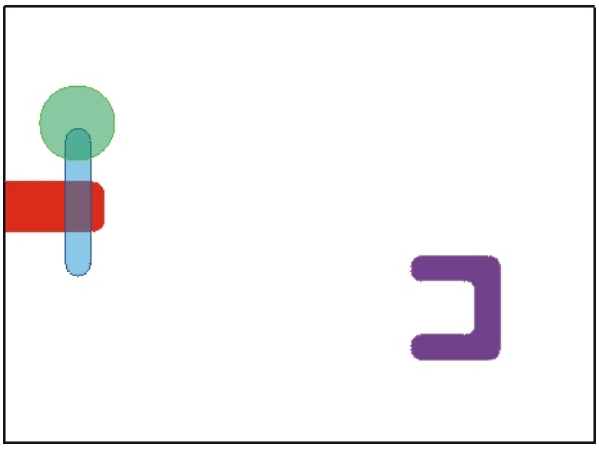

Figure 22. F-15 composite rudder specimen flaw design.

Figure 23 displays the Laplacian image of the left side of the rudder specimen (note: specimen was rotated relative to figure 22) created using equation (27). Prior to the use of equation (27) the images grayscales were smoothed using the parametric model presented in section 3.3. The two red squares were insulators placed on the specimen surface as registration marks. As can be seen in the image, the flaws are visible, as are the honeycomb cells. Since the flaws are large in comparison to the cells they are easily detected. However, if the flaws were on the order of the cell size they might not be noticed. This example demonstrates the tendency of Laplacian operators to highlight edges. Since this effect is undesirable, other metrics were considered.

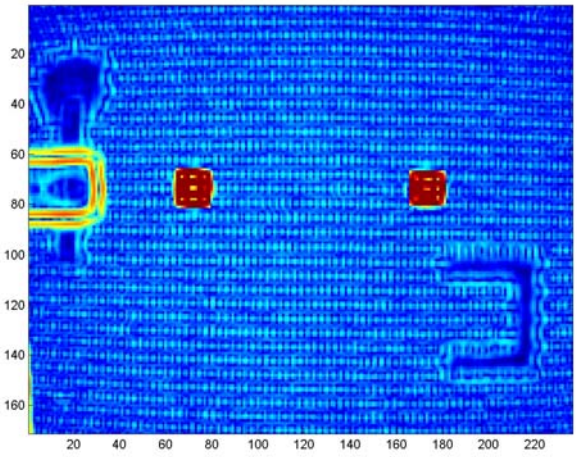

Figure 23. Composite Laplacian image for an F-15 rudder.

4.3.1 Flaw Detection Metric Comparison

To avoid the noise accentuation created by the Laplacian operation, the following metrics were investigated. Each of these variations to the equations (26) and (27) still highlight spatial and temporal differences in the datacube, but with different noise accentuation properties. Also included in these alternative metrics are formulations that couple both spatial and temporal effects. To facilitate the application of these and other metrics, an

analysis software package was developed. This software, called *ATAC* (Automated Thermal Analysis Code), is presented in appendix A. Prior to the application of equations (29) through (37), the *ATAC* software applies the parametric model presented in section 3.3 to perform spatio-temporal smoothing of the image data. Also, the composite image created by equations (29) – (37) are normalized for display.

$$(29)\quad Gray(x,y) = \sum_{t\,=\,frame\,start}^{t\,=\,frame\,end} G(x,y,t)$$

$$(30)\quad Gray(x,y) = \sum_{t\,=\,frame\,start}^{t\,=\,frame\,end} \left|\frac{\partial G(x,y,t)}{\partial t}\right|$$

$$(31)\quad Gray(x,y) = \sum_{t\,=\,frame\,start}^{t\,=\,frame\,end} \left|\frac{\partial^2 G(x,y,t)}{\partial t^2}\right|$$

$$(32)\quad Gray(x,y) = \sum_{t\,=\,frame\,start}^{t\,=\,frame\,end} \sqrt{\left(\frac{\partial^2 G(x,y,t)}{\partial x^2}\right)^2 + \left(\frac{\partial^2 G(x,y,t)}{\partial y^2}\right)^2}$$

$$(33)\quad Gray(x,y) = \sum_{t\,=\,frame\,start}^{t\,=\,frame\,end} \left|\frac{\partial^2 G(x,y,t)}{\partial x^2}\right| + \left|\frac{\partial^2 G(x,y,t)}{\partial y^2}\right|$$

$$(34)\quad Gray(x,y) = \sum_{t\,=\,frame\,start}^{t\,=\,frame\,end} \sqrt{\left(G(x,y,t)\frac{\partial^2 G(x,y,t)}{\partial x^2}\right)^2 + \left(G(x,y,t)\frac{\partial^2 G(x,y,t)}{\partial y^2}\right)^2}$$

$$(35)\quad Gray(x,y) = \sum_{t\,=\,frame\,start}^{t\,=\,frame\,end} G(x,y,t)\sqrt{\left(\frac{\partial^2 G(x,y,t)}{\partial x^2}\right)^2 + \left(\frac{\partial^2 G(x,y,t)}{\partial y^2}\right)^2}$$

$$(36)\quad Gray(x,y) = \sum_{t\,=\,frame\,start}^{t\,=\,frame\,end} \left|\frac{\partial G(x,y,t)}{\partial t}\right|\sqrt{\left(\frac{\partial^2 G(x,y,t)}{\partial x^2}\right)^2 + \left(\frac{\partial^2 G(x,y,t)}{\partial y^2}\right)^2}$$

$$(37)\quad Gray(x,y) = \sum_{t\,=\,frame\,start}^{t\,=\,frame\,end} \left|\frac{\partial^2 G(x,y,t)}{\partial t^2}\right|\sqrt{\left(\frac{\partial^2 G(x,y,t)}{\partial x^2}\right)^2 + \left(\frac{\partial^2 G(x,y,t)}{\partial y^2}\right)^2}$$

Equations (29) – (37) were applied to the datacubes acquired from two aluminum test specimen that each contained 21 flaws. Though the results from each equation were evaluated, only sample results will be provided in this report to illustrate the effectiveness of each equation in detecting and highlight the hidden flaws. However, to illustrate the general characteristics of each metric, figures 25-33 present the results for each metric applied a datacube for an aluminum test specimen that contains three flaws ranging in size from 0.45”

to 0.5” in diameter. The specimen surface has chalk registration lines to highlight the regions containing flaws and chalk numbers for each individual flaw. The datacubes for figures 25-33 were acquired at 59 frames per second with a pixel resolution of 256 x 256. Twenty five frames were summed to produce the results provided in each figure. The image data window (“x” pixels by “y” pixels by “t” image frames) used to identify the parameters for the local spatio-temporal smoothing polynomial was 7 x 7 x 11 for each datacube.

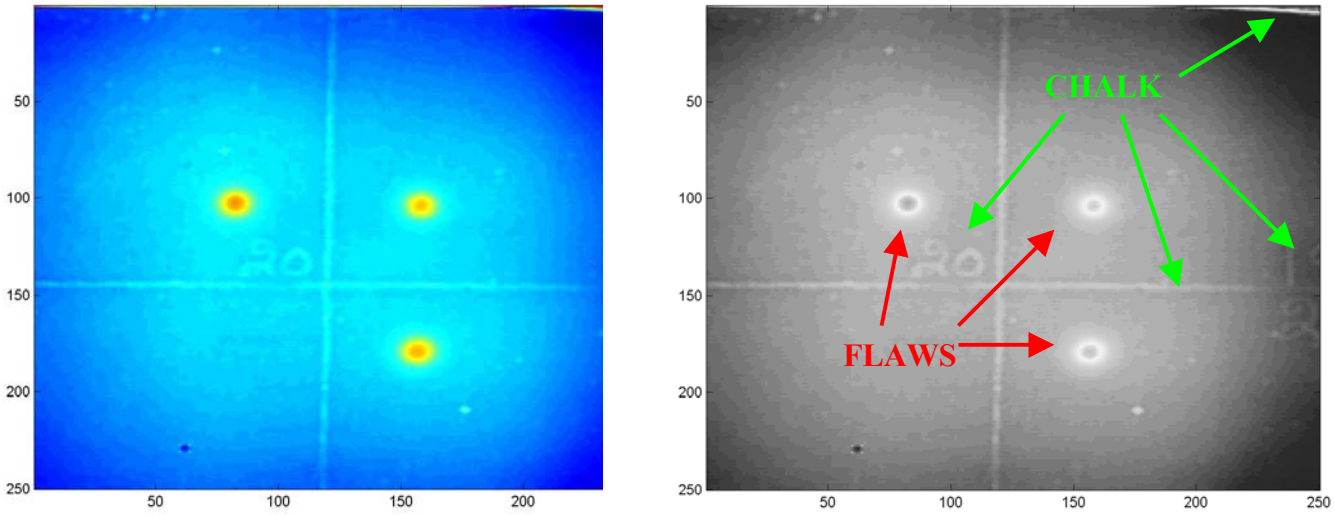

$$Gray(x,y) = \sum_{t=frame\,start}^{t=frame\,end} G(x,y,t)$$

Figure 24. Composite radiance image.

Figure 24 presents the results from the application of equation (29). This image represents a composite radiance image that is analogous to a temperature image if the surface emissivity is uniform. In this image the three circular flaws have good visibility because the regions above the flaws cool slower than the adjacent regions. The spatial noise is relatively low, though the chalk registration lines are highly visible. Though summing more frames typically improves the flaw visibility, it offered no significant advantage here because the chalk had greater thermal latency than the flaws. In general, the composite radiance image proved effective in highlighting hidden flaws, but was not able to remove the influence of the chalk and other surface spatial noise.

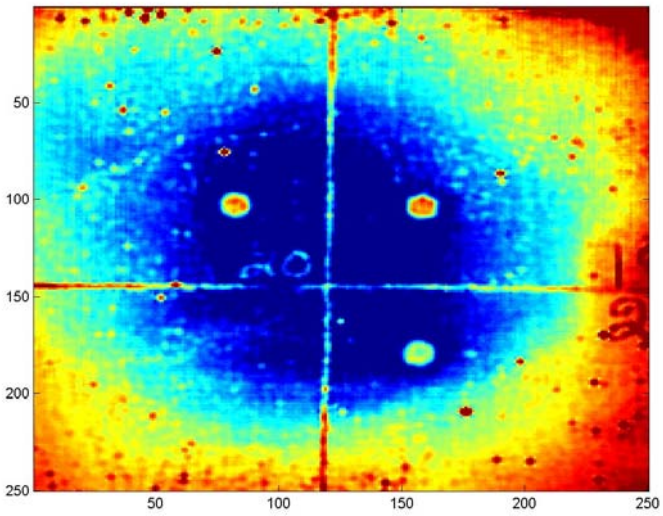

$$Gray(x,y) = \sum_{t=frame\,start}^{t=frame\,end} \left| \frac{\partial G(x,y,t)}{\partial t} \right|$$

Figure 25. Composite temporal first derivative image.

Figure 25 presents the results from the application of equation (30). This composite image represents the summation of the temporal derivatives of the surface radiance image. Though the three circular flaws have acceptable visibility, this metric accentuated much more spatial noise than the composite radiance image (equation 29). Further, the chalk registration lines and numbers are also very visible. Summing additional provided no improvement because the chalk had greater thermal latency than the flaws. In general, the composite temporal derivative image proved effective in highlighting large hidden flaws, but was not as effective on the smaller flaws that had spatial dimensions on the order or the sizes of the spatial noise.

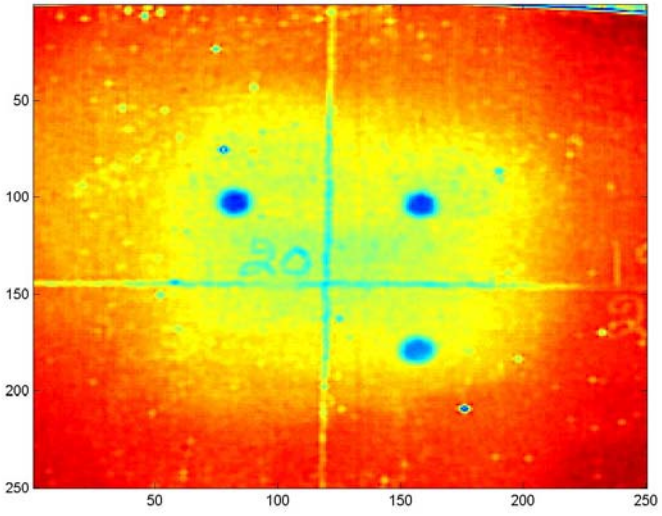

$$Gray(x,y) = \sum_{t=frame\,start}^{t=frame\,end} \left| \frac{\partial^2 G(x,y,t)}{\partial t^2} \right|$$

Figure 26. Composite temporal second derivative image.

Figure 26 presents the results from the application of equation (31). This composite image represents the summation of the temporal second derivatives of the surface radiance image. Similar to the results from the temporal first derivative (equation 30), the three circular flaws

have acceptable visibility but there is a significant amount of spatial noise. Though the false colors in figure 26 may not display as much apparent noise as figure 25, the relative strength of the noise relative to the flaw signal strength is about the same. In general the temporal second derivative has similar characteristics to the temporal first derivative. Considering the analytical solutions presented in section 3.1 demonstrate that the thermal energy transfer process is somewhat exponential in nature, it is not surprising that the first and second temporal derivative metric produce composite images with similar characteristics. In general, the composite temporal second derivative image proved effective in highlighting hidden flaws, but was not effective in mitigating spatial noise or the effects of the surface chalk.

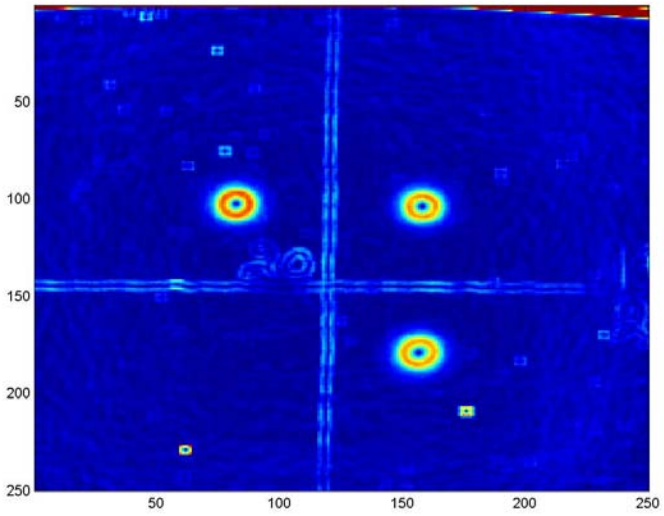

$$Gray(x,y) = \sum_{t=frame\,start}^{t=frame\,end} \sqrt{\left(\frac{\partial^2 G(x,y,t)}{\partial x^2}\right)^2 + \left(\frac{\partial^2 G(x,y,t)}{\partial y^2}\right)^2}$$

Figure 27. Composite spatial Laplacian image – variant 1.

Figure 27 presents the results from the application of equation (32). This composite image represents a root mean square image of the Laplacian components of the surface radiance image. One advantage of this metric is that by evaluating the root mean square of the spatial second derivatives all perturbations add to the flaw's signal strength. In principal the Laplacian operator can result in the summation of a positive and negative component which partially cancel the flaw induced spatial perturbations. The metric in equation (32) avoids this potential problem. However, similar to the standard Laplacian operator noise and image edges are highlighted with double edges. Though the chalk is accentuated by equation (32), the other spatial noise is heightened less than with the temporal image derivative operators (equations 30 and 31). In general, equation (32) proved effective in highlighting hidden flaws and reducing localized spatial noise, but was not effective in mitigating the effects of the surface chalk.

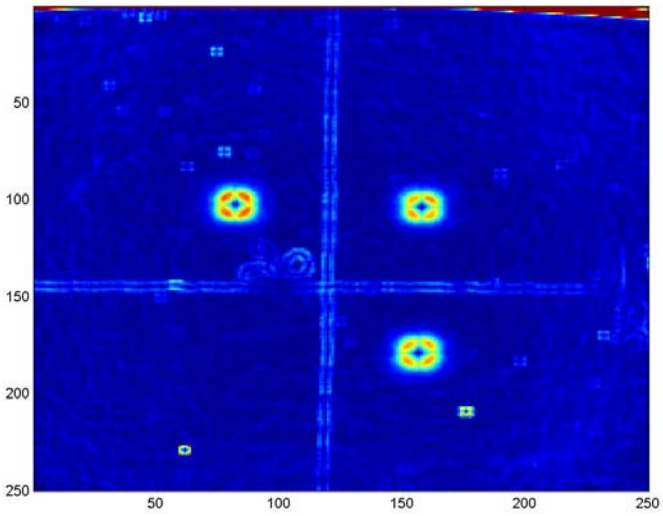

$$Gray(x,y) = \sum_{t=frame\,start}^{t=frame\,end} \left| \frac{\partial^2 G(x,y,t)}{\partial x^2} \right| + \left| \frac{\partial^2 G(x,y,t)}{\partial y^2} \right|$$

Figure 28. Composite spatial Laplacian image – variant 2.

Figure 28 presents the results from the application of equation (33). Equation (33) sums the magnitude of the Laplacian components. Similar to the root mean square (rms) metric provided by equation (32), equation (33) sums all flaw perturbations without the possibility of cancellation between the x and y spatial terms. However, the summation of the magnitudes of the components provides a stronger signal than the rms approach. Nevertheless, the resulting composite image in figure 28 is very similar in nature to figure 27. The only apparent qualitative difference is that the circular flaws appear to be almost square with a cross passing through the flaw. As with equation (32), equation (33) proved effective in highlighting hidden flaws and reducing localized spatial noise, but was not effective in mitigating the effects of the surface chalk.

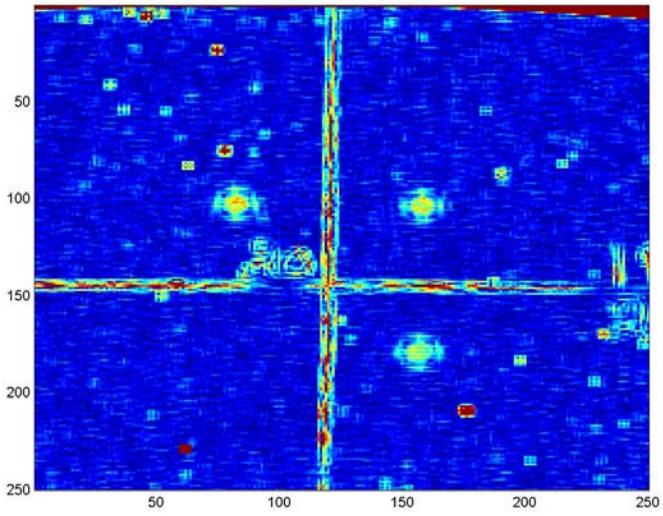

$$Gray(x,y) = \sum_{t=frame\,start}^{t=frame\,end} \sqrt{\left(G(x,y,t) \frac{\partial^2 G(x,y,t)}{\partial x^2} \right)^2 + \left(G(x,y,t) \frac{\partial^2 G(x,y,t)}{\partial y^2} \right)^2}$$

Figure 29. Composite radiance weighted Laplacian image – variant 1.

Figure 29 presents the results from the application of equation (34). This composite image can be considered a radiance weighted Laplacian filter. As was shown in figures 24 and 27, both the composite radiance image and rms Laplacian image produce highly visible flaws with a relatively good signal to noise ratio. The combination of these metrics provided by equation (34) reduced the flaw signal to noise ratio and increased the amount of localized spatial noise. In general, equation (34) proved capable of flaw detection, but was not efficient at reducing spatial noise or chalk artifacts.

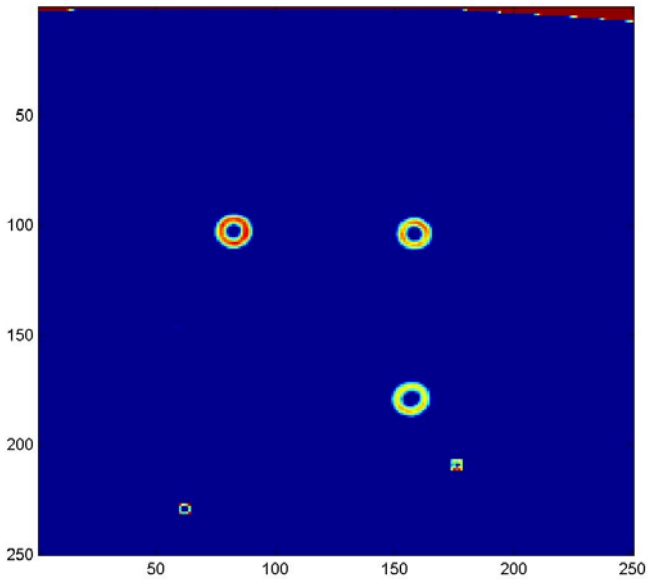

$$Gray(x,y) = \sum_{t=frame\,start}^{t=frame\,end} G(x,y,t)\sqrt{\left(\frac{\partial^2 G(x,y,t)}{\partial x^2}\right)^2 + \left(\frac{\partial^2 G(x,y,t)}{\partial y^2}\right)^2}$$

Figure 30. Composite temperature weighted Laplacian image – variant 2.

Figure 30 presents the results from the application of equation (35). This composite image is a variation of the radiance weighted rms Laplacian filter provided by equation (34). Since the radiance (more specifically the image grayscale) is always a positive value, it would appear that the equations (34) and (35) should be mathematically equivalent and provide the same composite image. However, as described in section 3.3, the experimental data is smoothed by fitting the image data to a weighted 18 parameter model that is spatially and temporally quadratic. As such, the product of the radiance and quadratic spatial terms is not necessarily the same as the fitted coupled parameters. Indeed, as shown in figure 30, the metric based on the fitted coupled parameters was much more effective at lessening the influence of spatial and chalk noise sources. The only chalk effects not significantly mitigated are along the top edge of the image (principally the upper right hand corner in red). Though image 30 displays virtually no noise, the data shows that some noise is still present but with a strength that is much lower than the signal strength. As such, the normalized image does not display noise. Of all of the metrics investigated, equation (35) typically proved to be the best metric for detecting flaws and mitigating noise.

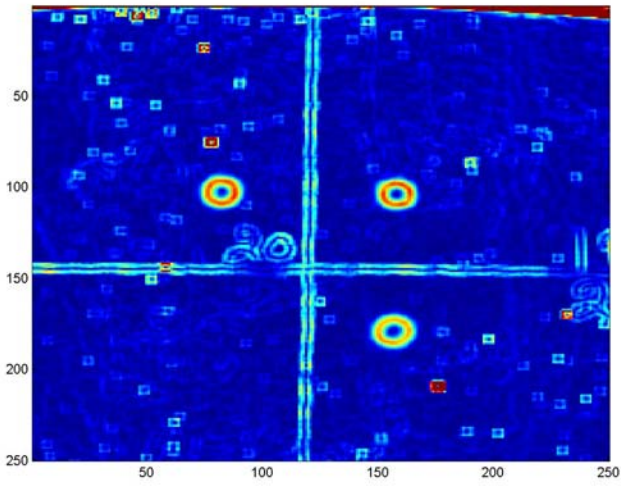

$$Gray(x,y) = \sum_{t\ =\ frame\ start}^{t\ =\ frame\ end} \left| \frac{\partial G(x,y,t)}{\partial t} \right| \sqrt{\left(\frac{\partial^2 G(x,y,t)}{\partial x^2} \right)^2 + \left(\frac{\partial^2 G(x,y,t)}{\partial y^2} \right)^2}$$

Figure 31. Composite temporal derivative weighted Laplacian image.

Figure 31 presents the results from the application of equation (36). This composite image is an rms Laplacian filter weighted by the magnitude of the temporal derivative of the radiance. The spatial noise is relatively low, though the chalk registration lines are highly visible. In general, equation (36) proved effective in highlighting hidden flaws, but was not able to remove the influence of the chalk and other surface spatial noise.

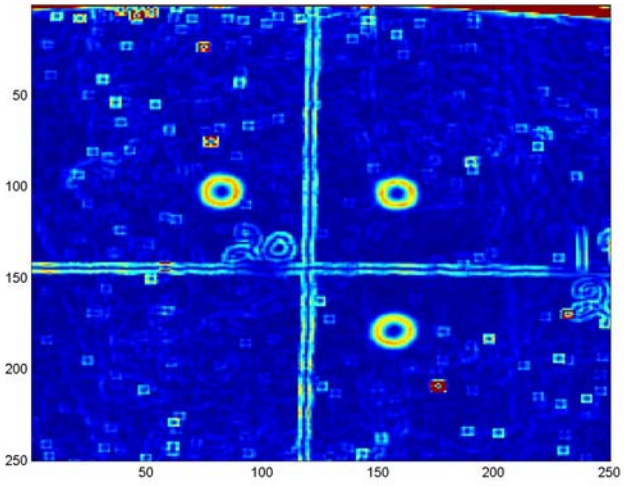

$$Gray(x,y) = \sum_{t\ =\ frame\ start}^{t\ =\ frame\ end} \left| \frac{\partial^2 G(x,y,t)}{\partial t^2} \right| \sqrt{\left(\frac{\partial^2 G(x,y,t)}{\partial x^2} \right)^2 + \left(\frac{\partial^2 G(x,y,t)}{\partial y^2} \right)^2}$$

Figure 32. Composite temporal second derivative weighted Laplacian image.

Figure 32 presents the results from the application of equation (37). This composite image is an rms Laplacian filter weighted by the magnitude of the temporal second derivative of the radiance. From a qualitative standpoint, figure 32 looks virtually identical to figure 31. In

both cases the spatial noise is relatively low, though the chalk registration lines are highly visible. However, the flaw signals in figure 11 are actually stronger than the corresponding flaw signals in figure 32. In general, equation (37) proved effective in highlighting hidden flaws, but was not able to remove the influence of the chalk and other surface spatial noise. The following table compares of the average signal to noise ratio for each metric provided by equations 29 – 37. Each average ratio was computed after subtraction of the lowest value in the composite image. Three specific ratios are provided: ratio of flaw signal to background noise signal, flaw signal to chalk signal in upper right hand corner, and flaw signal to crossing chalk line signal. As reference, the initial thermal image datacube was evaluated to determine the frame which provided the highest flaw signal to noise ratio after subtraction of the preflash image. For this data set the best flaw to noise ratio was 2.05. At this optimal frame the flaw to chalk line ratio was 2.08 and the flaw to corner chalk ratio was 0.75.

	Fig. 25 Eq. 29	Fig. 26 Eq. 30	Fig. 27 Eq. 31	Fig. 28 Eq. 32	Fig. 29 Eq. 33	Fig. 30 Eq. 34	Fig. 31 Eq. 35	Fig. 32 Eq. 36	Fig. 33 Eq. 37
Flaw/ Noise	2.25	2.06	3.45	10.04	23.63	7.31	31.80	20.36	16.49
Flaw/Corner	0.96	0.18	1.09	0.216	0.29	0.13	0.21	0.16	0.25
Flaw/Line	1.93	2.05	2.38	3.29	3.88	0.81	3.5	1.82	1.62

The radiance weighted rms Laplacian filter (equation 35) generated the highest flaw signal to noise ratio. Also, the sum of the magnitude of the Laplacian components (equation 33) and the rms Laplacian filter weighted by the magnitude of the temporal derivative of the radiance (equation 36) provided excellent signal to noise ratios. Though equation (35) produced a signal strength greater than the crossing chalk lines, like most of the metrics it was not as effective at mitigating the heavy chalk layer in the upper right hand corner of the image.

4.3.2 Experimental Results: Radiance Weighted RMS Laplacian Metric

The previous section presented sample results that demonstrated the effectiveness of the radiance weighted rms Laplacian metric. In this section additional datacubes are evaluated with this metric to assess the ability of equation (35) to detect small hidden flaws.

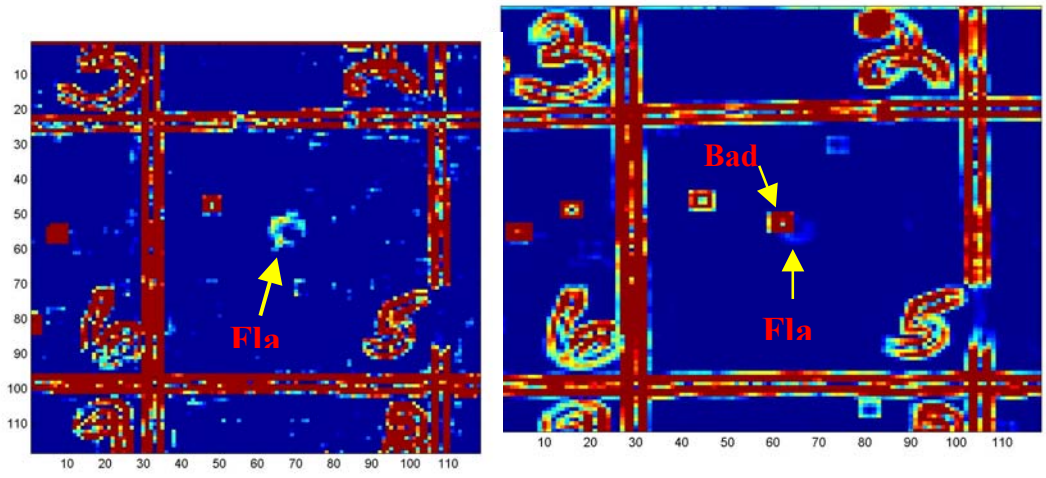

Figure 33. 0.1” diameter flaw detection results.

Figure 33 presents composite images generated by equation (35). The image highlights a circular 0.100" diameter flaw located in the image center. The left image was created from a data set collected at 248 frames per second with a 127 x 124 pixel window. The right image was created from a data set collected at 476 frames per second with a 64 x 64 pixel window (data scaled to 127 x 122 for comparison). Since the same amount of computer RAM was allocated for each data acquisition, more frames were collected at the higher frame rate (right image). As a result, since more frames were available for the summation, the composite result for the 476 frame per second case had reduced spatial noise, though the chalk lines and numbers are still very apparent. Further, it is interesting to note that the small flaw in the image center is partially obscured by a bad pixel in the image on the right. However, despite the bad pixel the flaw was still detected by the metric.

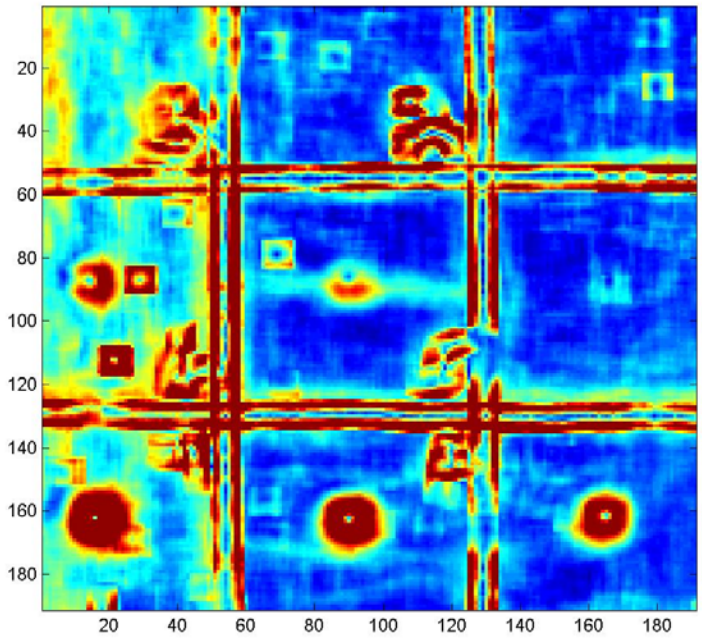

Figure 34. Multiply flawed test specimen detection results.

Figure 34 displays the composite image produced by equation (35) for an aluminum plate with circular backside flat bottom hole diameters ranging from 0.0125"to 0.2". The images were acquired at 119 frames per second with a 256 x 256 pixel window. This specimen is subdivided into numbered square regions with the flaws located approximately in the center of each region. The chalk lines separating each region and the chalk numbers are highly visible for most regions. Increasing the number of image frames summed in equation (35) would reduce the chalk visibility, but it might also reduce the visibility of the smaller flaws that had a lower latency time than the larger flaws which are more effective at trapping energy. However, this small flaw visibility reduction might be overcome by with a contrast enhancing technique such as differential histeresis processing. In this experimental test case the flaws on the bottom row are very visible. In the middle row the flaw visibility is noticeably reduced. The 0.075" flaw in the center right region is partially visible with a signal strength that is sufficiently above the image noise for flaw detection. However, none of the flaws in the top row are detectable. Hence, the 0.075" flaw is probably the smallest flaw that can be reliably detected in this specimen.

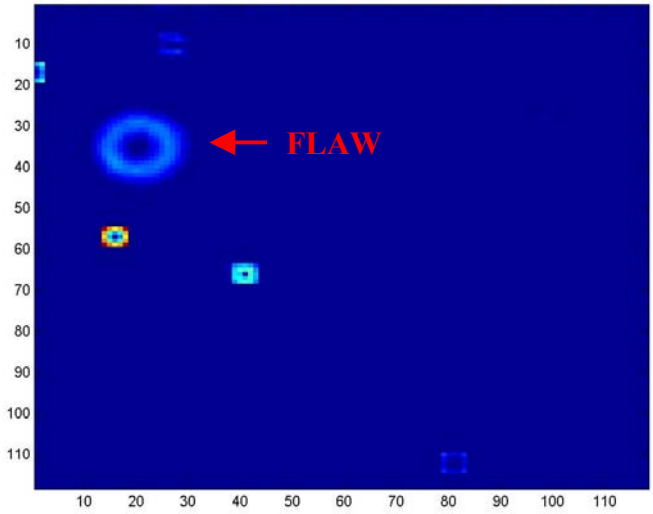

Figure 35. 0.475" flaw detection example.

Figure 35 displays the composite images generated by equation (35) for an aluminum specimen with a single 0.475" diameter circular backside flat bottom hole. This datacube was acquired at 248 frames per second with a 127 x 124 pixel window. In this test case the chalk lines and numbers are not visible, though there are a few square noise sites. These square artifacts are caused by bad camera pixels. Often these effects can be removed by recalibrating the camera. The reasons the chalk is not visible is probably the combination of a thinner chalk layer, the use of more image frames (a few hundred) than are typically available at lower camera speeds, and the large flaw size. Higher camera speeds provide more images with a measurable flaw signal. Though data can be acquired for a longer period at the slower frame rates, it often adds little to the results because of the limited flaw latency.

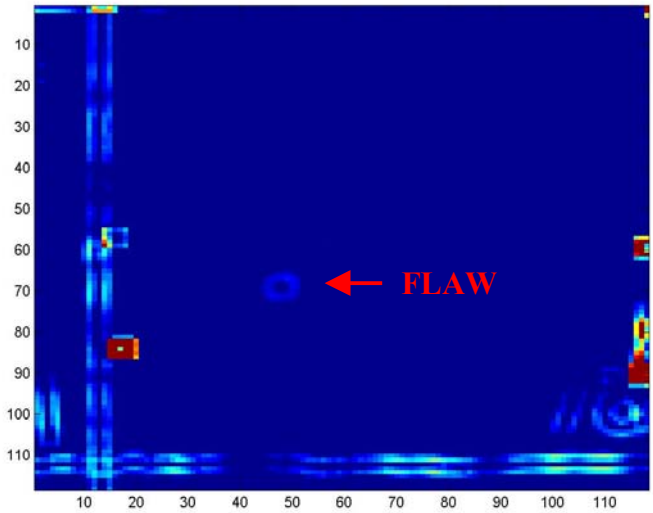

Figure 36. 0.225" flaw detection example.

Figure 36 displays the composite images generated by equation (35) for an aluminum specimen with a single 0.225" diameter circular backside flat bottom hole. This datacube was acquired at 248 frames per second with a 127 x 124 pixel window. In this test case the chalk lines and numbers are highly visible. Also, there are localized noise points (square regions in red) that indicate bad pixel locations. Since the flaw is about one half the size of the flaw in the previous test case (figure 35), its energy trapping capability is lower. As a result, the 0.225" flaw does not generate enough signal strength in the metric to overcome the surface chalk visibility. However, the flaw does have very good visibility relative to the now chalk background regions.

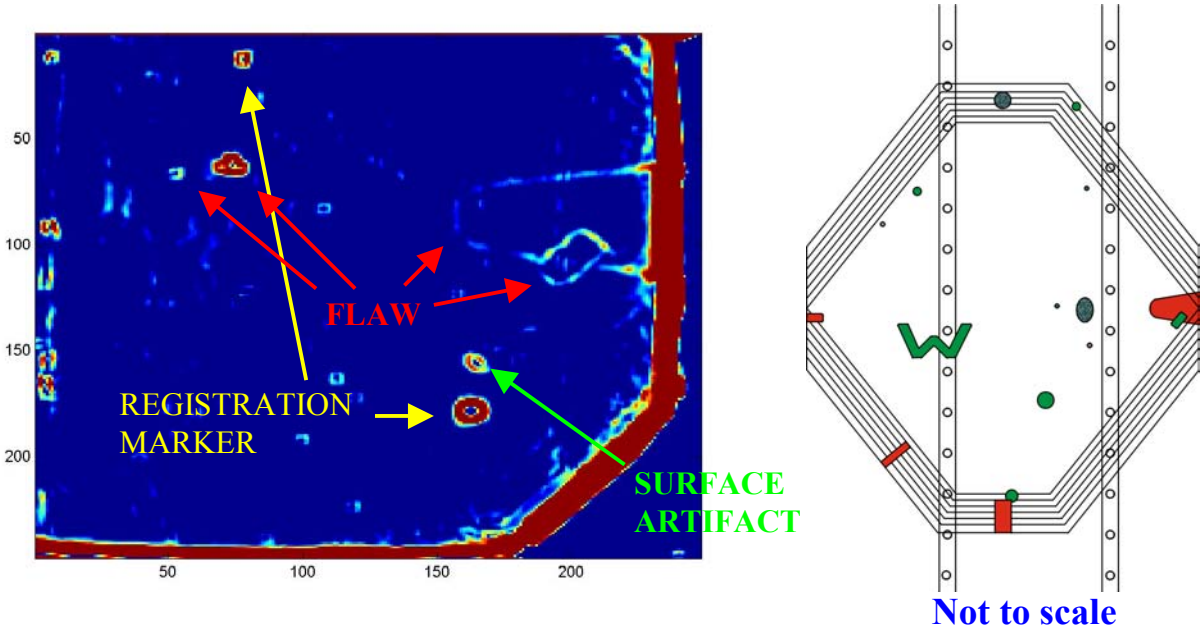

Figure 37. Composite doubler example.

Figure 37 displays the composite images generated by equation (35) for an eight layer boron epoxy composite doubler test specimen. The infrared images were acquired at 30 frames per second. The drawing on the right illustrates the general construction details and flaw locations. The 3.0'x3.0' specimen consisted of 0.187" thick 7075-T6 aluminum plate with a 2.0'x2.0' octagonal 7 ply composite boron-epoxy doubler (with a 181 fiberglass outer protective layer). Two 1.0" wide x 0.125" thick 7075-T6 straps with fasteners (one strap with steel and the another with aluminum fasteners) were assembled on the back of the specimen to simulate a wing skin assembly. The doubler contained 16 programmed flaws (8 grafoil inserts, 4 pull tabs, 2 surface grinds, and two pinhole induced "natural flaws") and multiple unprogrammed disbonds and delaminations. The flaws ranged in size from a minimum of 0.125" in diameter to the largest flaw with a maximum dimension of 4.0". The red flaws in the drawing are air gaps created by pull tabs inserted between the composite plies during the specimen construction. The green flaws are grafoil (flexible graphite) inserts that have thermal properties that are very similar to the composite layers. Each flaw was placed at a different depth within the composite structure. In addition to the implanted flaws, registration markers (insulated tape and lead tape) were placed on the specimen surface. Typically composites are thermally very noisy because there tends to be a significant amount of small disbonds and porosity variations created during the composite layup process.

Equation (35) was sensitive to these localized air gaps. However, since these air gaps are undesirable flaws created during the application of the repair, it is desirable that equation (35) highlight their presence. Though the metric provided by equation (35) was able to detect some of the flaws, it did not appear to be as effective on composites as it was on metallic structures. This may be partially due to the presence of the 4.0" long flaw located on the right side of the image. This flaw generated a very large signal that had the greatest amount of latency of any flaw in the specimen. As a result, it tended to overwhelm the small flaws. However, when very large flaws are detected, it may be important to mask out these regions and reapply equation (35) to the remainder of the image to detect the smaller flaws.

4.4 Surface Effects

Variations in the surface conditions and material property differences such as emissivity and near surface conduction inhomogeneities can act as significant spatial noise sources that may obscure the presence of true flaws. This has been apparent in many of the examples considered in section 4.3 where chalk on the specimen surface often generated a higher signal strength than the flaws. In some instances surface emissivity variations accentuate small or nonexistent surface temperature variations. These variations can be very transient or have a latency that can create a false flaw indication. In other instances, surface condition variations can include areas that either store energy or dissipate it very slowly in comparison to the surrounding structure. When this occurs the corresponding surface hot spot can have significant latency, creating a false flaw indication with the metric provided by equation (35). Consider, for example, the data set that contains the thermal image in figure 38.

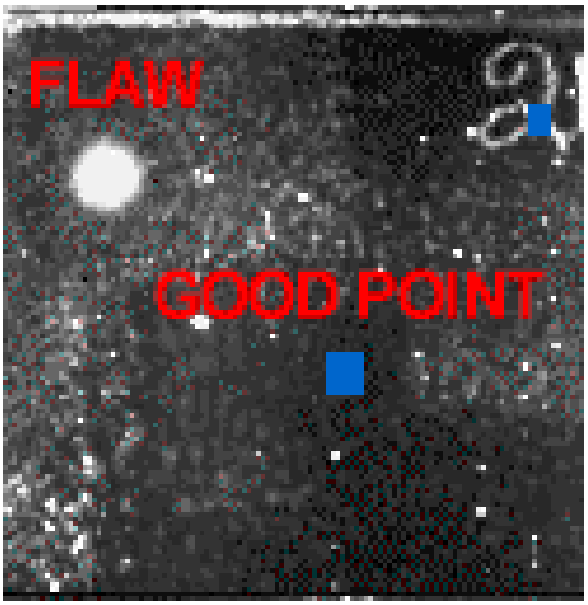

Figure 38. Sample image: Minimal surface energy storage example.

This image displays a very visible circular flaw in the upper left hand corner, as well as chalk marks and numbers. In principal, the thin chalk on the specimen surface should not significantly affect the local cooling rates. The plots in figure 39 illustrate how a point over the center of the flaw, a normal non-flawed image position (center of blue box near middle of image), and chalk (blue box over the chalk number 2 in upper right hand corner) cool over

time. As can be seen in the expanded early time plot (bottom plot), the chalk initially appears "hotter" than the good area, but quickly cools to the point where it matches the behavior of the unflawed image location point. However, the area over the flaw remains hotter for a significantly longer period of time.

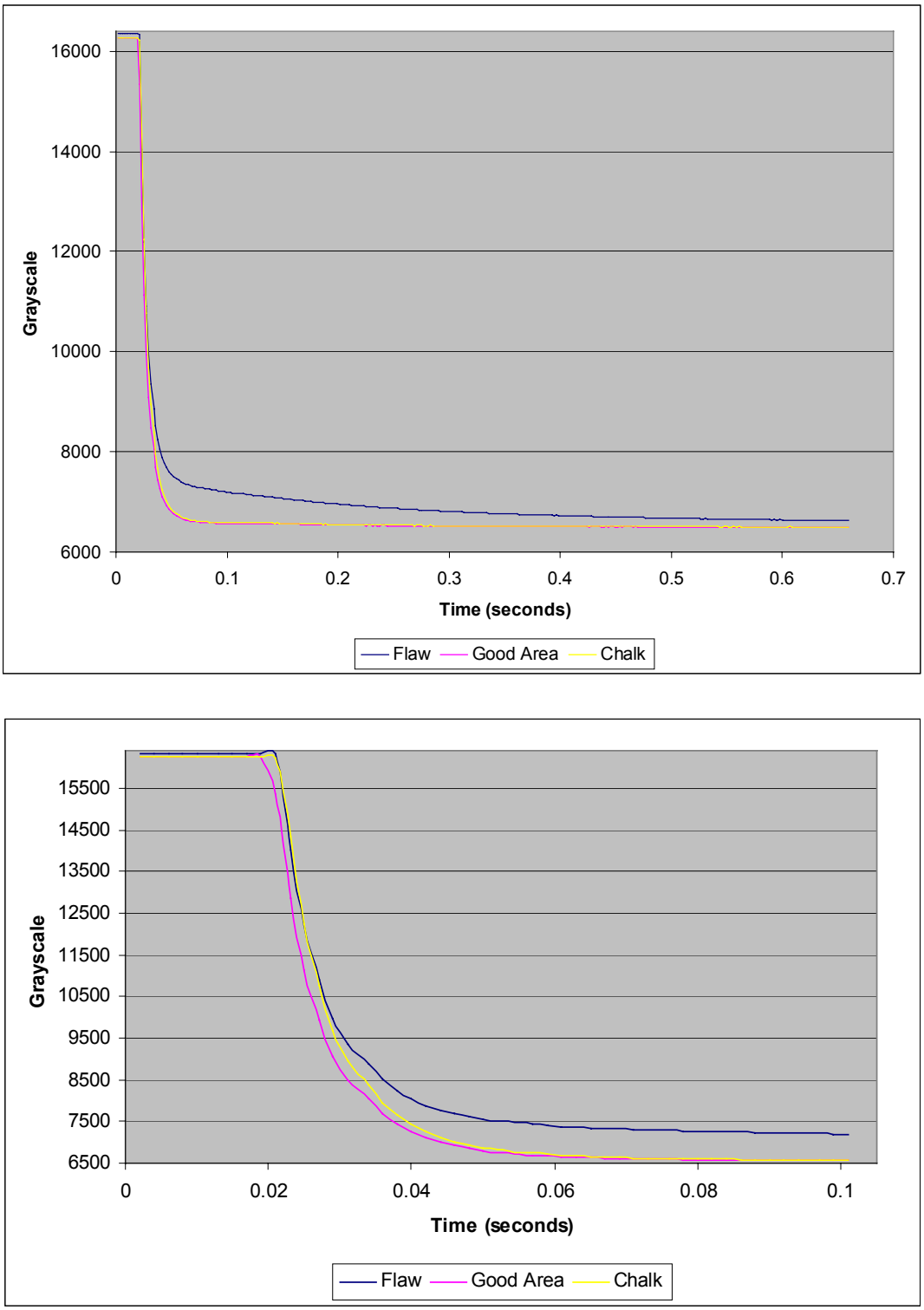

Figure 39. Temporal cooling plots: minimal surface energy storage example.

Under the conditions illustrated in figure 39, the surface effects have minimal impact on the flaw detection capabilities provided by equation (35). However, in other cases the surface features can produce anomalous behaviors that are not transient in nature. Consider, for example, the data set that contains the thermal image in figure 40. Qualitatively the image has similar characteristics to the image in figure 38. The circular flaw if highly visible and the chalk lines and numbers are clearly discernible. There does not appear to be visual or infrared evidence of significant differences between figures 38 and 40. However, the temporal cooling rates demonstrate anomalous cooling for this data set relative to the previous case.

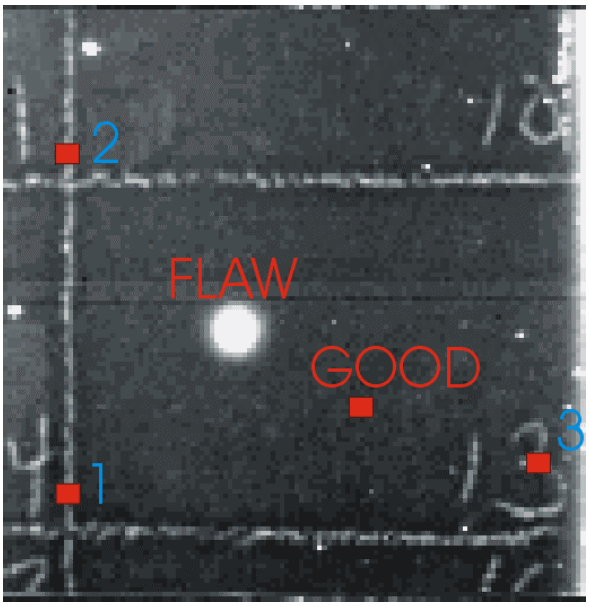

Figure 40. Sample image: Significant surface energy storage example.

For comparison purposes, figure 41 plots the temporal cooling over the flaw center, the "good" (unflawed) position located under the red box, and over three separate points with chalk on the surface of the specimen. Though the chalk appears visually similar in the image, significant apparent cooling rate differences occur. A shown in the middle plot, initially each of the chalk locations appear hotter than the unflawed position, but quickly begin to cool, similar to the case plotted in figure 39. However, the bottom plot in figure 41 shows that the temperature at chalk position number 2 actually stabilizes at a hotter temperature than the other chalk points and begins to exceed the apparent temperature over the flaw after about 0.23 seconds. This is physically possible and may be caused by the emissivity, local energy storage, chalk conductivity, or some other near surface effect. Locations that act like chalk position number 2 create local hot spots that are not indicative of internal flaws. However, this behavior is not consistent at all chalk locations. Consider, for example, the temporal cooling at chalk points 1 and 3. As was the case in the previous example, chalk points 1 and 3 behave similarly, quickly cool to the temperature of the unflawed point. However, chalk point 2 retains a constant offset for a significant period of time.

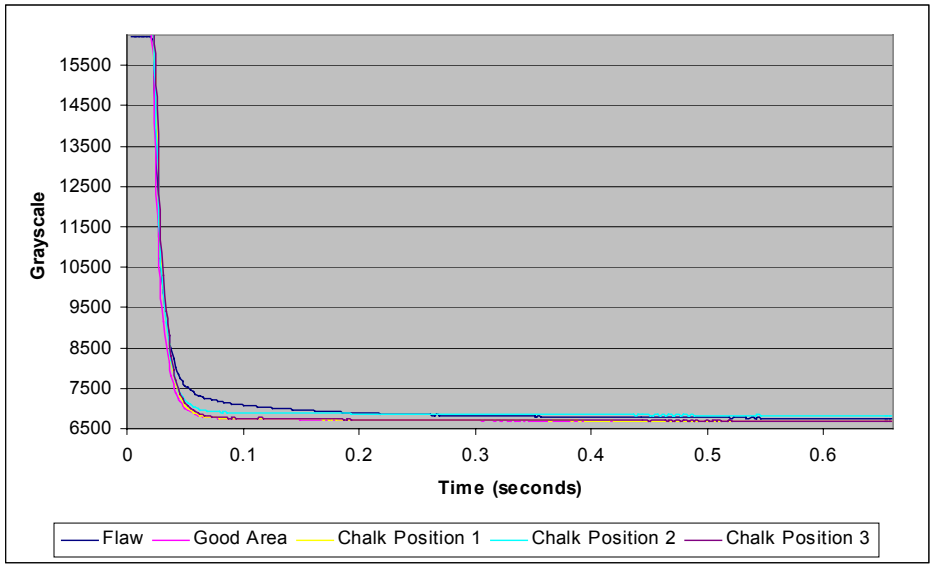

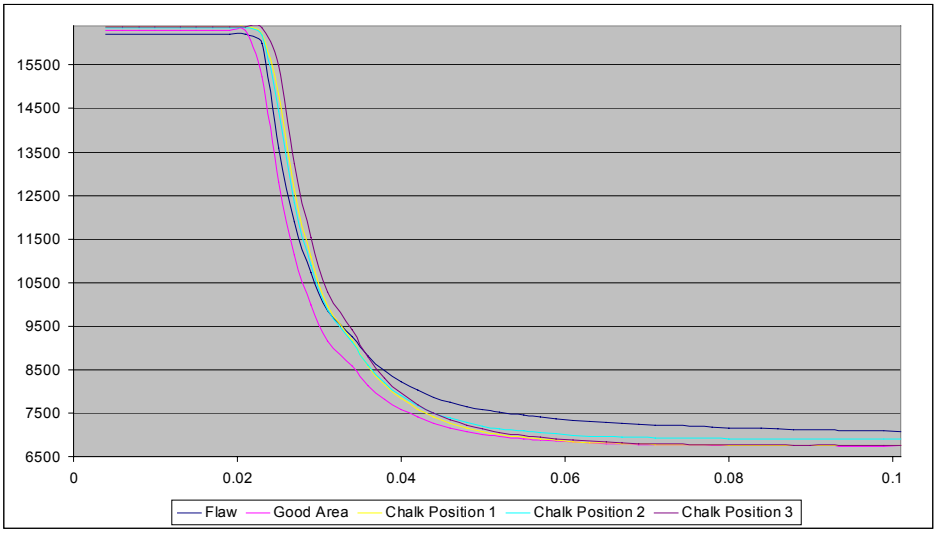

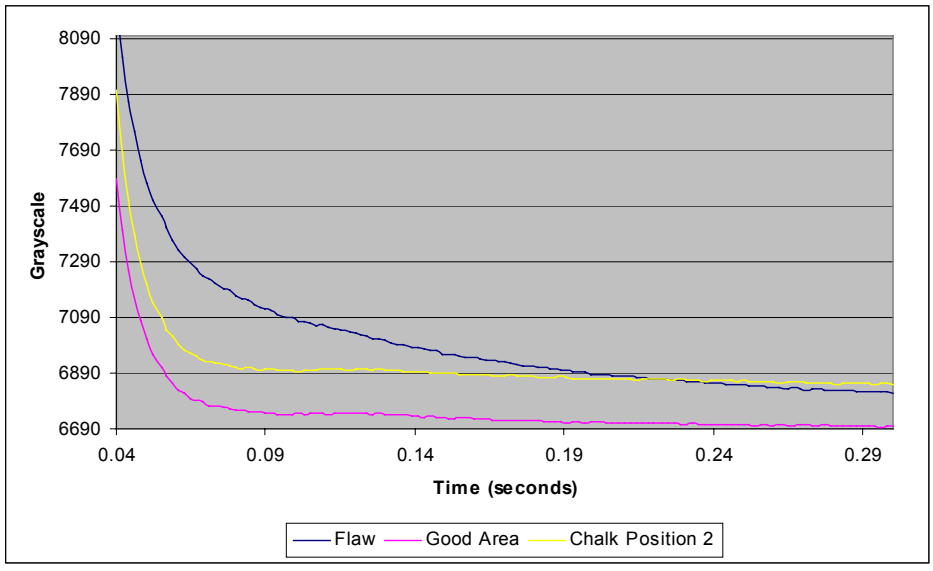

Figure 41. Temporal cooling plots: anomalous surface effects example..

Historically, the approach used to reduce the influence of surface effects has been to subtract the average of the preflash images from all post-flash images. When this is performed on the data set displayed in figure 41 there is a noticeable shift in the plot for chalk position 2 which keeps its apparent temperature below that of the flawed area. However, as shown in figure 42, chalk position 2 still remains offset from the plots for the other chalk points. An alternative that has also been investigated relies on relative measurements. In principle, the positions with the fastest cooling rate should correspond to an unflawed region. If this position is used as a reference the signal to noise ratio can be increased by subtracting the value at this point from every other image point at each point in time. However, this approach does not perform well when there is nonuniform surface heating since it is linearly proportional to the amount of energy absorbed.

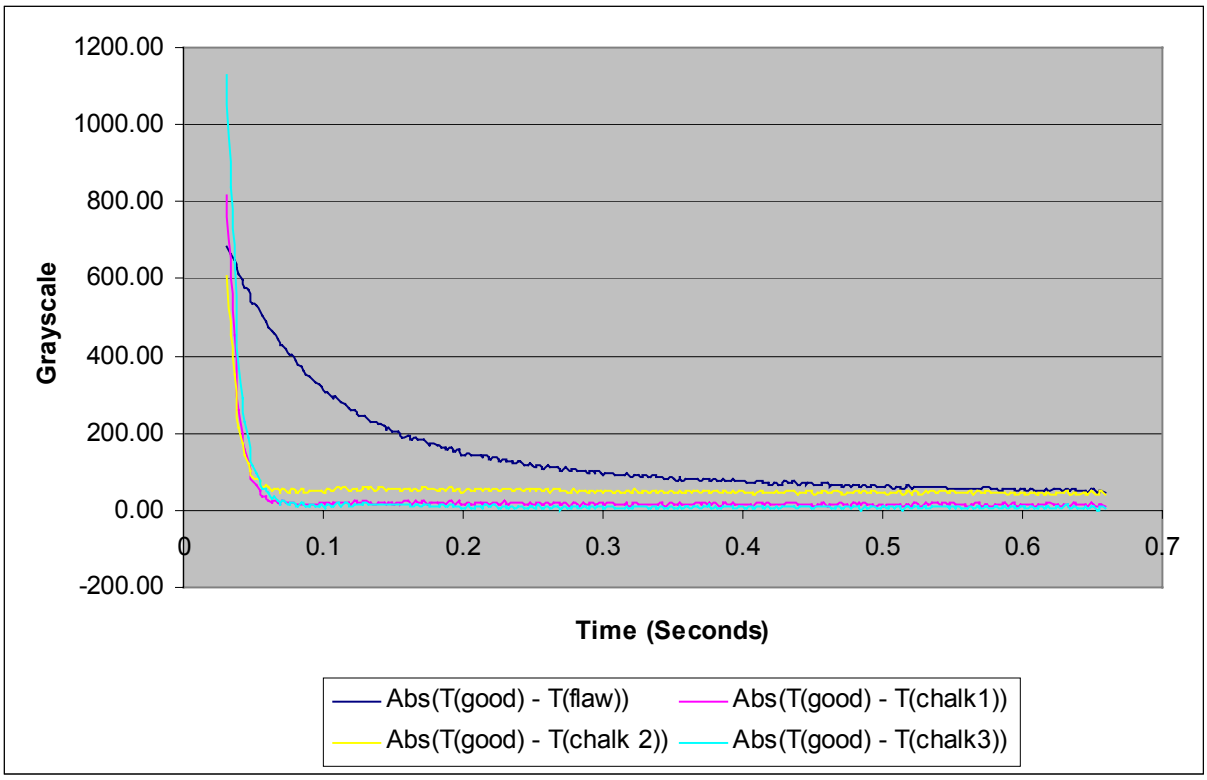

Figure 42. Temporal surface cooling plots with preflash image subtraction.

4.4.1 Surface Effects Correction Factor

When considering the thermal radiation process, effects such as emissivity are multiplicative factors. As such, it would appear that a multiplicative correction factor would perform better than a baseline image subtraction process. To investigate this possibility the each image data point was multiplied by a correction factor equal to the ratio of the average preflash grayscale at an arbitrary reference point and the average preflash grayscale for the current image point. This can be considered a rough estimation for a surface emissivity correction factor. When this correction was applied to the same data set that was used to produce figures 41 and 42, it provided the results displayed in figure 43.

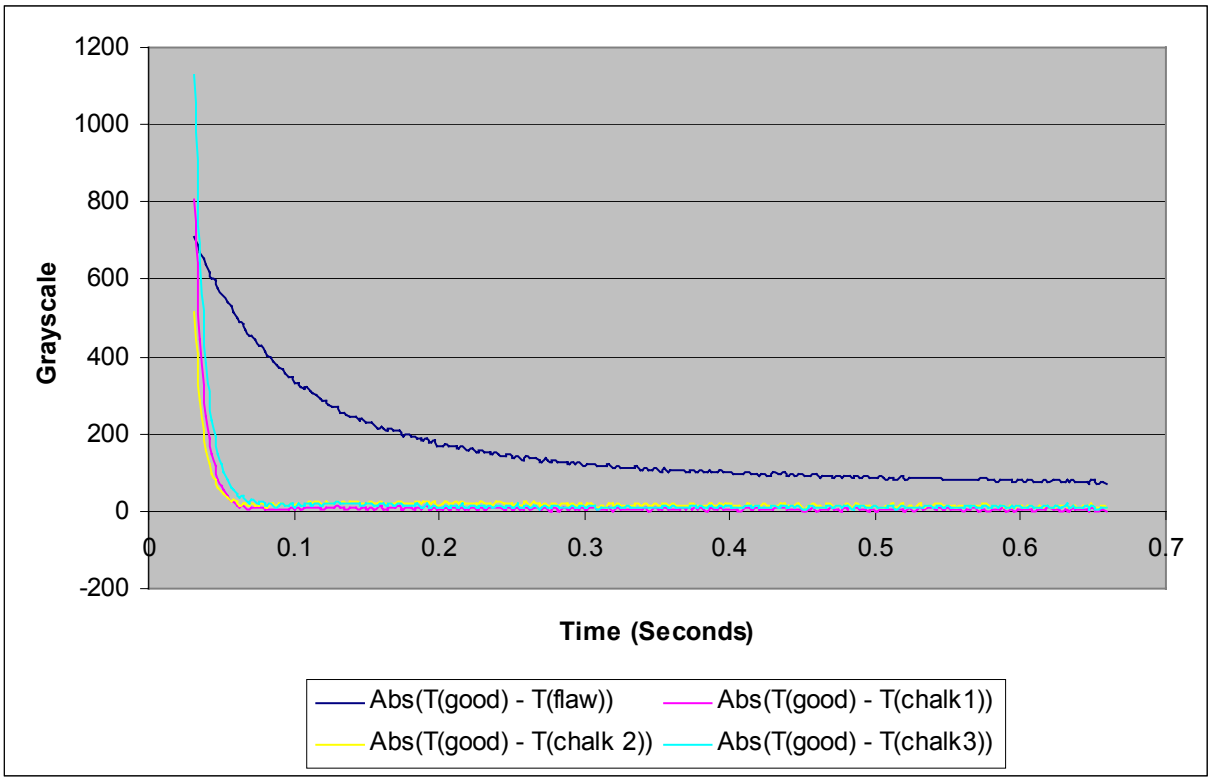

Figure 43. Temporal surface cooling plots with a multiplicative surface correction factor.

As can be observed in the plot in figure 43, as a result of the application of the multiplicative correction factor each chalk position now behaves similarly and in a manner consistent with the test case displayed in figure 39. Chalk position number 2 no longer has an offset in its temporal cooling plot. There are still variations in chalk temperature immediately after the application of the flash heating, but these effects dampen out quickly. It is likely that the slight temperature increase at early times may represent differences in the amount of energy absorbed by the chalk. Small variations in the chalk thickness should create some local differences, but should not adversely affect flaw detection using equation (35). However, if the surface chalk is thick enough to trap significant energy, its low thermal conductivity could still create significant thermal latency in the infrared image even after the correction factor is applied. This is because the correction factor is intended to account for local emissivity variations, but not conductivity variations.

Though the cooling plots in figure 43 provide promising results, the true test of the utility of the multiplicative surface correction factor is in its application in conjunction with equation (35). Figure 44 presents a comparison of the composite images provided by equation (35) with (bottom image) and without (top image) the use of the surface correction factor. The data set used in this test was acquired at 120 frames per second using a 256 x 256 pixel window. The test specimen is a 0.060” thick aluminum plate that contains nine backside circular flat bottom holes with diameters ranging from 0.225” to 0.425”. Eighty image frames were used to create both images.

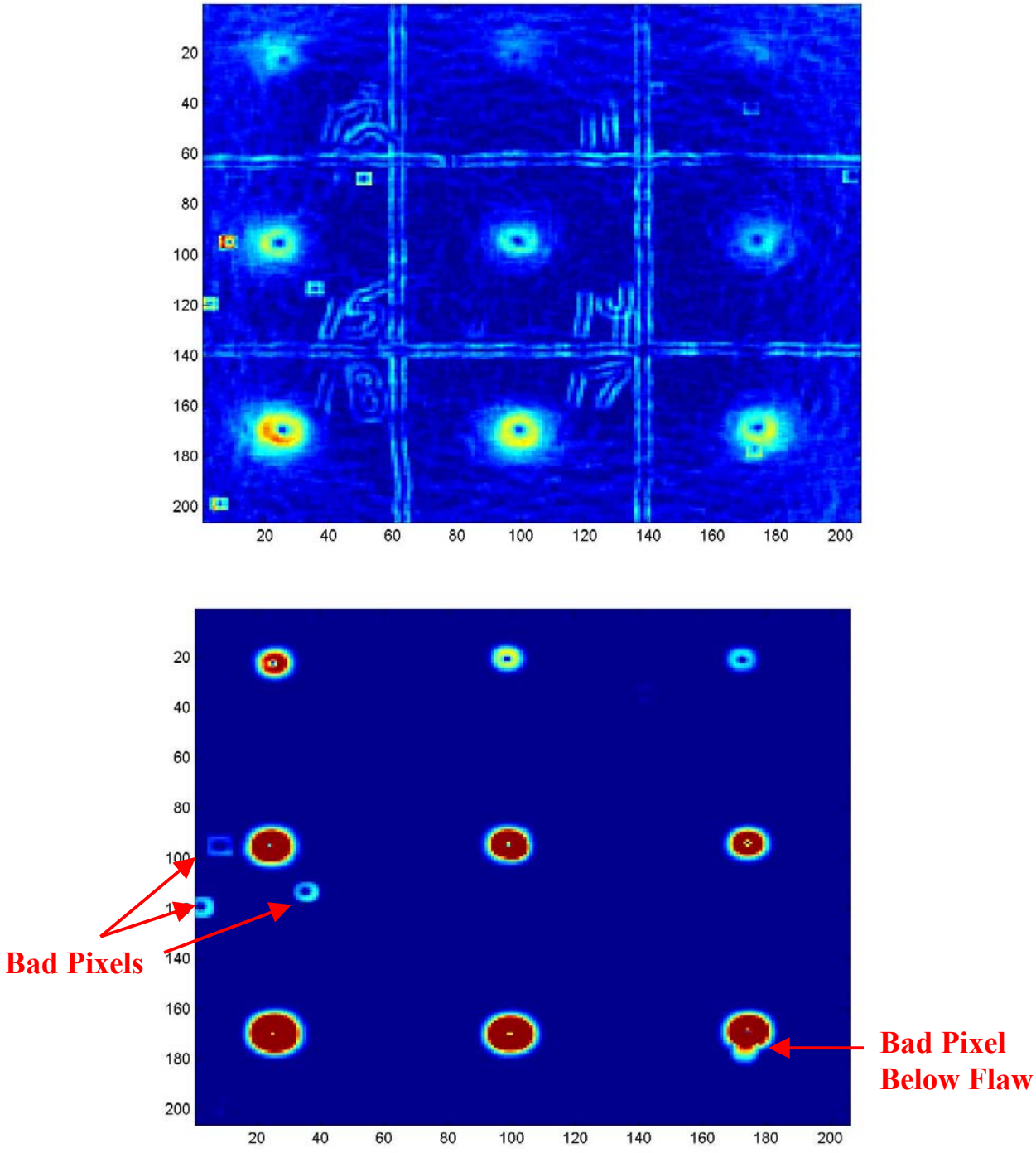

Figure 44. Surface emissivity variation correction analysis example.

Figure 44 demonstrates a significant reduction in surface effects. Virtually all of the surface chalk effects were removed when the surface correction factor was applied to the image data prior to the use of equation (35). Though most of the surface effects were removed, anomalous pixels were still highlighted. Application of equation (35) to the regions containing pixels usually results in a square outline around the suspect pixel. However, these

pixels typically have signal values that are four to five standard deviations outside the preflash mean values. Therefore, these abnormal pixels can be filtered out with standard post processing methods.

The test case presented in figure 44 provided outstanding results. Unfortunately, not all test cases were as successful. Figure 45 presents a comparison of the composite images provided by equation (35) without (left image) and with (right image) the use of the surface correction factor. The data set used in this test was acquired at 248 frames per second using a 127 x 124 pixel window. The test specimen is a 0.060" thick aluminum plate that contains a 0.3" diameter backside circular flat bottom hole. Though there was a large reduction in the surface chalk visibility, it was not completely removed. It is likely that the chalk thickness was greater in this test case than in the example presented in figure 44. As a result, the energy absorbed in the thicker chalk regions created latent heat signatures indicative of stored energy rather than emissivity variations.

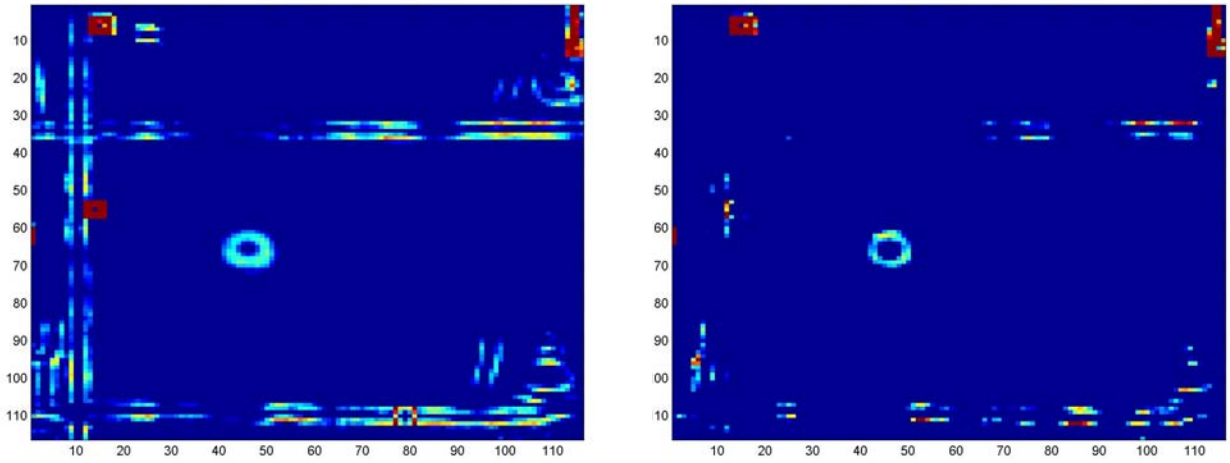

Figure 45. Surface emissivity variation correction analysis example number 2.

Figure 34 presented results with a minimum flaw size detection capability of 0.075". In that example no surface correction factor was applied and the small flaw visibility was marginal. This may have been due in part to the frame speed (119 frames per second). To examine the importance of the camera speed, this specimen was reexamined with an acquisition rate of 476 frames per second. To achieve this speed the pixel data window was reduced to 64 x 64. Figure 46 displays the composite results for a 24 x 24 region surrounding the 0.075" diameter flaw. This image was generated by applying the surface correction factor to the image data prior to using equation (35). As demonstrated in the image, the flaw visibility has been significantly improved over the results presented in figure 34. This suggests that the application of equation (35) in conjunction with the surface correction factor may provide detection capabilities below 0.075" flaws. It is important to note that the actual flaw cross section was very near the fundamental pixel resolution limit, occupying only a few pixels. However, the algorithm detects is very sensitive to the lateral diffusion effects which, when considered temporally, provide a cumulative effect that magnifies the apparent flaw size. However, once the flaw has been highlighted, identifying the time when the local diffusion

gradient first becomes nonzero can better approximate its actual size. This sizing capability could be easily automated and added to the analysis software if needed.

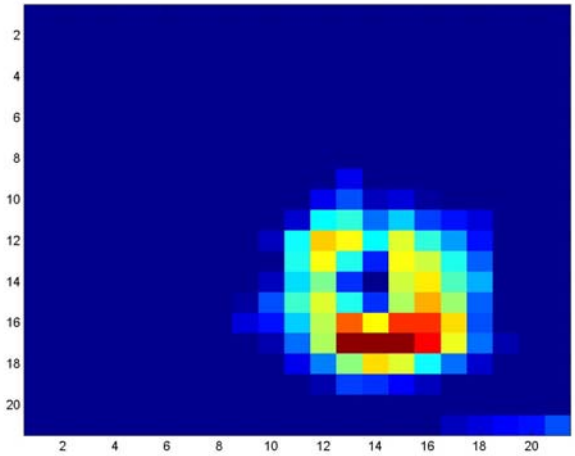

Figure 46. 0.075" flaw detection with the application of a surface correction factor.

4.4.2 Paint Thickness Effects On Flaw Detection

A longstanding challenge for dynamic thermography has been the detection and quantification of flaws in specimens that contain significant surface paint thickness variations. Paints typically have a thermal conductivity on the order of two to three orders of magnitude smaller than metals. As a result, small variations in paint thickness create thermal depths that correspond to significant equivalent variations in the metal thickness. Further, dynamic thermography relies on the ability of the flaw to trap energy or increase its conduction/dissipation relative to the surrounding areas. When this situation occurs it typically creates a detectable temperature variation on the specimen surface if there are no intervening effects. As discussed and investigated in section 2.4, the specific heat and conductivity of paint adversely impact the detection of underlying flaws. First, paint has a higher specific heat than metal, requiring a greater energy contribution to create the same temperature rise. This means that the flaw must be larger (i.e., trap more energy) to create the same detection signal. Second, paint is a good thermal insulator in comparison to metal. As such, it temporally spreads out the impulsive heating to create a longer heating duration and lower initial energy input for the underlying metal structure. Since the aluminum is very efficient at conducting the energy away, the local temperature gradients surrounding the flaw will favor lateral energy conduction as opposed to energy trapping if the paint thickness is too large. In other words, if the heating rate from the paint is too slow the transmitted energy may be conducted away in the aluminum too quickly to create the local storage needed to produce a detectable flaw signature even if equation (35) is applied to the data set.

As a preliminary investigation of the impact of paint thickness on flaw detection, a datacube was collected for a painted aluminum plate. The plate was 6.0" x 6.0" x 0.070" thick aluminum and contained a 2.0" diameter flat bottom hole circle milled out of the center of

the backside of the specimen. Paint was applied to the four quadrants on the top surface of the specimen as shown in figure 47.

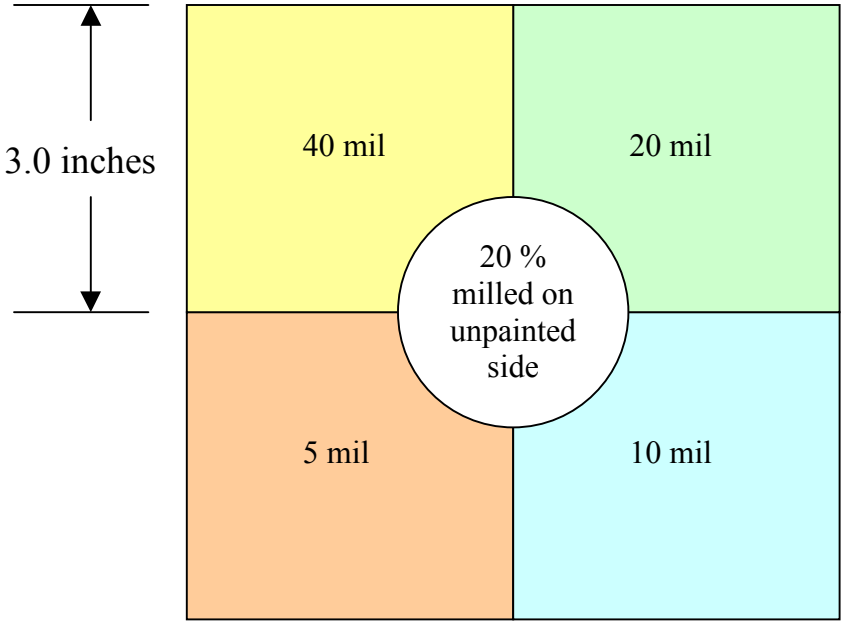

Figure 47. Painted test specimen design.

Figure 48 presents the composite image generated by equation (35) after the application of the multiplicative surface correction factor to the image data set collected at 60 frames per second. The black circular ring in the image center was drawn to outline the milled flaw edges. Evidence of the flaw was present in the region under the 5 mil paint layer, but not under any of the other areas. Further, the sharp edge at the transition between the paint layers created a very strong signal that may have overwhelmed most of the flaw signature. Based on this preliminary result, it does not appear encouraging that equation (35) would be helpful in detecting flaws under thickly painted surfaces. When the contrast was adjusted it was possible to bring out aspects of the flaw in each of the quadrants except for the 40 mil paint region. However, when this image enhancement was performed each quadrant had to be addressed separately. This post processing is not practical in most situations because the paint thickness and flaw locations are typically unknown. Nevertheless, it does suggest that there is an underlying signal that might be detectable using an alternative metric. The plots in figure 49 further support this. Figure 49 plots the temporal cooling for a flawed and unflawed region in each quadrant. In each case the apparent temperature over the milled flaw remains hotter than the regions over the non-milled area. This demonstrates that the flaw does produce a detectable temperature change even under a 40 mil thick paint layer. However, the relative difference between the flawed and unflawed regions is small. Further, the cooling rate changes were influenced more by the paint thickness differences than the flaw. As such, it is likely that paint thickness variations will continue to hinder flaw detection and quantification. Further analysis and experimentation is needed to determine the reliable detection limits for painted test specimens.

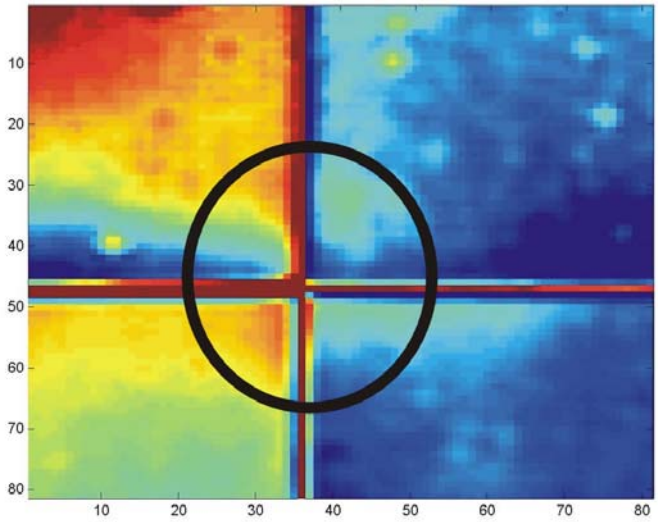

Figure 48. Paint thickness test specimen composite results.

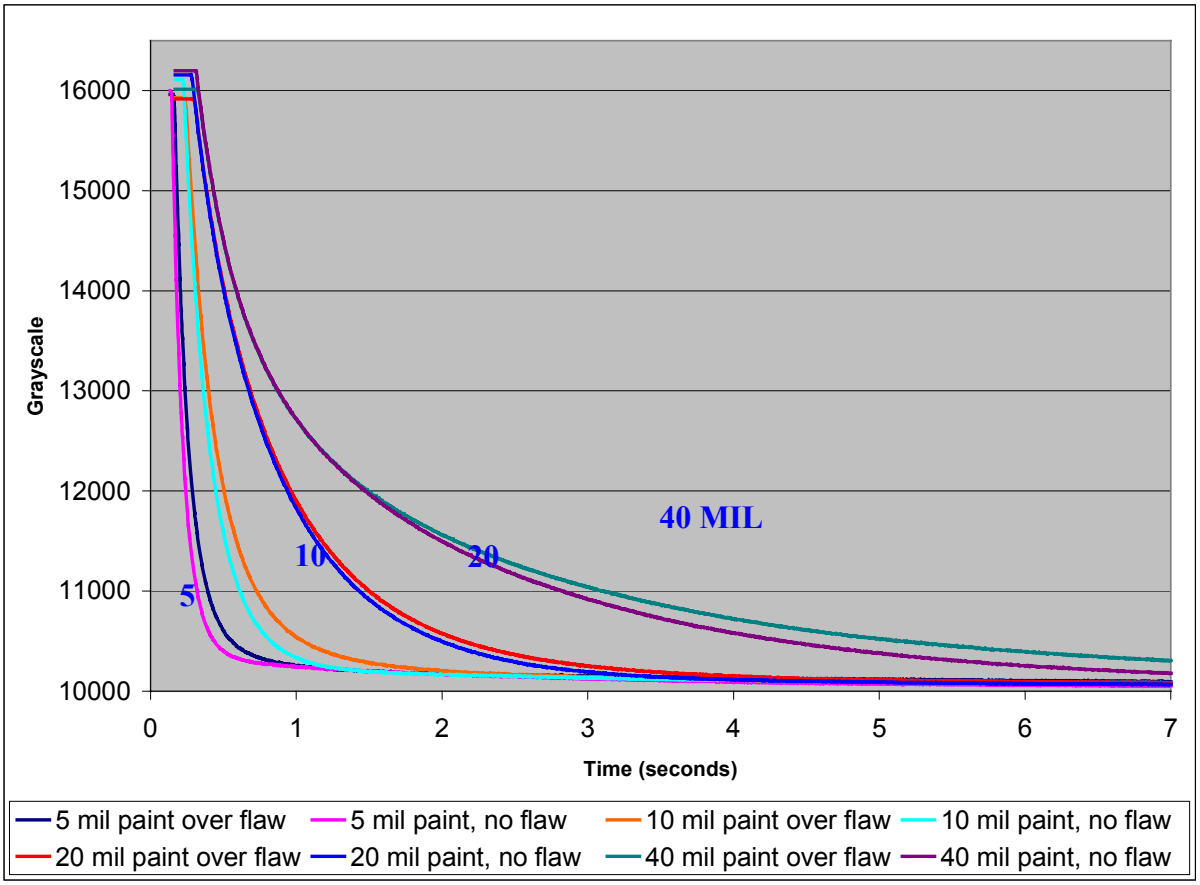

Figure 49. Paint thickness specimen temporal cooling plot.

While the preliminary results on thickly painted structures were not encouraging, further investigation of the influence of paint on flaw detection is warranted. This future study

should include both an analytical and controlled experimental examination of painted test specimens. Though this effort will probably require a finite element analysis, preliminary investigations may be performed using an analytical solution. Following the orthogonal-expansion approach used by Rajic, it may be possible to estimate the surface temperature on a painted metallic plate using the following relations:[42]

$$T(x,t) = \sum_{n=1}^{\infty} \frac{\dfrac{Q}{\alpha_1 \beta_n^2}\left(1 - e^{-\alpha_1 \beta_n^2 t}\right)\cos \beta_n x}{N},$$

$$N = \frac{2\beta_n p + \sin 2\beta_n x}{4\beta_n} + \frac{\delta^2 \sin^2 \beta_n p\left[2\gamma\beta_n (L-p) + \sin 2\gamma\beta_n (L-p)\right]}{4\gamma\beta_n \sin^2 \gamma\beta_n (L-p)},$$

$$\alpha_1 = \textit{paint thermal diffusivity},$$

$$\alpha_2 = \textit{metal thermal diffusivity},$$

$$k_1 = \textit{paint thermal conductivity},$$

$$k_2 = \textit{metal thermal conductivity,}$$

$$L = \textit{metal thickness,}$$

$$p = \textit{paint thickness,}$$

$$\gamma = \sqrt{\frac{\alpha_1}{\alpha_2}},$$

$$\delta = \frac{k_1}{k_2}\gamma^{-1}.$$

Assuming perfect thermal contact between the paint and metal plate provides the following transcendental equation for the eigenvalues:

$$\delta \tan(\beta_n p) + \tan\left[\beta_n \gamma (L-p)\right] = 0.$$

The roots can be found using a Newton-Raphson method bounded by the singular points

$$\beta_n = \frac{n\pi}{2(L-p)\gamma}, \quad \beta_n = \frac{n\pi}{2p}.$$

5.0 CONCLUSIONS AND RECOMMENDATIONS

The two year research effort presented in this report focused on the evaluation and derivation of signal-processing operators for automated analysis of dynamic thermography infrared data sets, the development of an inspection simulation model, experimental validation of the derived flaw detection metrics, and creation of an analysis software package with enhanced flaw visualization tools. The principal achievements and recommendations from this effort included the following:

1. The developed thermal inspection model demonstrated that it was suitable for generating high fidelity simulation data. When this simulation data was provided to the developers of the Thermal Wave Imaging technology they were unable to distinguish the simulated image data from real inspection data.

2. The developed parametric model for spatio-temporal smoothing of the image data proved effective in mitigating the spatial and temporal noise. However, additional work is needed to determine the optimal weighting width scale factor t_σ to use in the nonnegative weighting function. Optimizing the scale factor may improve the signal to noise ratio and further improve the flaw detection limit. Additionally, future efforts should convert the developed parametric model into a convolution based digital filter that computes the 3-D (x, y, t) weighted filter coefficients consistent with the selected parametric model. Implementing the filter as a convolution kernel would significantly reduce the image analysis time.

3. The radiance weighted root mean square Laplacian operator proved to be the most effective metric for automated flaw detection. However, an rms Laplacian filter weighted by the magnitude of the temporal derivative of the radiance also generated promising results. The key factors influencing the performance of these two metrics were the number of image frames with flaw signals used to produce the composite image and the energy storage capacity of noise sources such as chalk applied to the specimen surface. In general, the flaw detection metrics performed better with increased camera speed because additional useful image frames were available for data processing. Recommended improvements to the analysis process include filtering of bad image pixels prior to the application of the analysis metric and the addition of a general polygon analysis window to the *ATAC* software to allow the user to define a non-rectangular data analysis region. Recalibrating the camera can minimize the number of bad image pixels. Alternately, since these pixels have signal values that are four to five standard deviations outside the preflash mean values they can be easily identified and removed from the analysis process.

4. The developed analysis operators proved effective on detecting flaws in both composite and metallic structures. In general, the radiance weighted root mean square Laplacian operator performed better on metallic structures than composite structures. On metallic structures with a 10” x 10” inspection area (corresponds to a 0.04” x 0.04” pixel spatial resolution) this metric demonstrated the ability to detect a 0.075” diameter flaw. The finite element results and preliminary experimental results

suggest that smaller flaws should be detectable with higher optical magnification levels. Insufficient tests were run on composite structures to estimate the practical detection limits on these structures.

5. Surface effects such as emissivity variations can present challenges to both manual and automated data analysis approaches. In this study we investigated the utility of a multiplicative correction factor equal to the ratio of the average preflash grayscale at an arbitrary reference point and the average preflash grayscale for each image point. This spatially variable correction factor proved very effective in mitigating surface effects. However, it could not overcome situations where significant energy was absorbed near the surface. In these instances emissivity effects did not principally cause the generated latent hot spots. However, it may be valuable to investigate the use of a similar approach that relies on the average of the first few post-flash images. This might rebaseline the images to reduce the influence of surface energy absorbers (e.g., thick chalk marks or other contaminants such as grease). If the camera speed is sufficiently high this post-flash corrective factor might still be capable of detecting small near surface flaws that have low latency.

6. A comprehensive analysis software package, *ATAC* (Automated Thermal Analysis Code), was developed to automate flaw detection using thermal imaging data. *ATAC* is an object-oriented PC software package with an interactive graphical user interface. Many of the software modules are multithreaded to allow two or more of the software features to run in parallel. This lets the user look at results from one set of parameters while processing a separate data analysis with a different set of parameters. *ATAC* performs all of the data processing, analysis, and display functions needed to provide reliable automated flaw detection. The raw data can be displayed and adjusted interactively as a 2-D or 3-D data set. The processed data can be displayed frame by frame or as a composite image that highlights image areas that have a high probability of containing an anomaly.

7. Paint proved to be an impediment to flaw detection. The finite element results provided data that suggests that a small amount of paint may actually improve the flaw latency and detection capabilities. However, increasing paint thickness and spatial paint thickness variations create significant challenges for thermal inspection systems and analysis algorithms. Considering the thermal properties of paint, minor thickness variations in paint could be mistaken for larger variations in the underlying metallic structure. Also, if the paint is too thick if provides a heating rate to the underlying structure that is too slow to generate a detectable temperature signature on the specimen surface. In these situations the energy transmitted through the paint may be conducted away in the aluminum too quickly to create the local storage needed to produce a detectable flaw signature.

6.0 REFERENCES

1. B. R. Frieden, "Computational Methods of Probability and Statistics," *The Computer in Optical Research*, ed. B. R. Frieden, Springer-Verlag, New York, p. 136 (1980).
2. William H. Press, et al, Numerical Recipes in Fortran, Second Edition, Cambridge University Press (1992).
3. Finite element modeling was performed by Wayne State University (PI: Dr. Xiaoyan Han) under purchase order BD-6281.
4. H. S. Carslaw and J. C. Jaeger, *Conduction of Heat in Solids*, 2nd Ed., Clarendon Press, London (1959).
5. Balageas, D., A. Deom, and D. Boscher, "Characterization and NDT of Carbon Epoxy Composites by a Pulsed Photothermal Method," *Materials Evaluation*, vol. 45, no. 4, pp. 461-465 (April 1987).
6. Maillet, D., A. S. Houlbert, S. Didierjean, A. S. Lamine, and A. Degiovanni, "Non-destructive Thermal Evaluation of Delaminations in a Laminate: Part II – The Experimental Laplace Transforms Method," *Composites Science and Technology*, vol. 47, pp. 155-172 (1993).
7. Batsale, J. A. Bendada, D. Maillet, and A. Degiovanni, "Distribution of a Thermal Contact Resistance: Inversion Using Exponential Laplace and Fourier Transformations and a Asymptotic Expansion*," Proceedings of the 1st International Conference on Inverse Problems in Engineering*, Palm Coast, FL, pp. 139-146 (June 13-18, 1993).
8. Grinzato, E. and S. Marinetti, "Materials NDE by Non-Linear Filtering Applying Heat Transfer Models," *Advances in Signal Processing for Non-Destructive Evaluation of Materials*, ed. X. Maldague, NATO ASI Series, Series E: Applied Sciences, vol. 262, Kluwer Academic Publishers, pp. 117-132 (1994).
9. D. J. Crowther, L. D. Favro, P. K. Kuo, and R. L. Thomas, "Thermal Wave Detection and Analysis of Defects in Structural Composite Materials*," Review of Progress in Quantitative Nondestructive Evaluation*, ed. D. O. Thompson and D. E. Chimenti, vol. 12, Plenum Press, New York, pp. 481-485 (1993).
10. L. D. Favro, X. Han, P. K. Kuo, and R. L. Thomas, "Improving the Resolution of Pulsed Thermal Wave Images with a Simple Inverse Scattering Technique," Journal De Physique IV, Colloque C7, vol. 4, pp. 545 – 550 (June 1994).
11. Crowther, D. J., Favro, L. D., Kuo, P. K., and Thomas, R. L., "Inverse Scattering Algorithm Applied to Infrared Thermal Wave Images," *J. Appl. Phys.*, vol. 74, pp. 5828-5834 (1993).
12. Favro, L. D., Han, X., Kuo, P. K., and Thomas, R. L., "Improving the Resolution of Pulsed Thermal Wave Images with a Simple Inverse Scattering Technique," *Journal de Physique*, IV-C7, pp. 545-551 (1994).
13. Pade, O., and Mandelis, A., "Computational Thermal-wave Slice Tomography with Backpropagation and Transmission Reconstructions," *Rev. Sci. Instrum.,* vol. 64, pp. 3548-3562 (1993).
14. P. R. Emeric and W. P. Winfree, "Thermal Characterization of Multilayer Structures from Transient Thermal Response," Review of Progress in Quantitative Nondestructive Evaluation, ed. D. O. Thompson and D. E. Chimenti, vol. 14A, Plenum Press, New York, pp. 475-482 (1996).

15. Winfree, W. P., B. s. Crews, and P. A. Howell, "Comparison of Heating Protocols for Detection of Disbonds in Lap Joints," *Review of Progress in Quantitative Nondestructive Evaluation*, ed. by D. O. Thompson and D. E. Chimenti, vol. 11A, Plenum Press, New York, pp. 471-478 (1992).
16. Spicer, J. W., W. D. Kerns, L. C. Aamodt, R. Osiander, and J. C. Murphy, " Time-Resolved Infrared Radiometry (TRIR) Using a Focal Plane Array for Characterization of Hidden Corrosion," Proceedings of SPIE Conference 1933, Thermosense XV, ed. Lee R. Allen, Orlando FL, p. 148 (1993).
17. L. A. LeSchack and N. K. Del Grande, "A Dual-Wavelength Thermal Infrared Scanner As A Potential Airborne Geophysical Exploration Tool," Geophysics, vol. 41, p. 1318 (1976).
18. K. E. Cramer, W. P. Winfree, E. R. Generazio, R. H. Bhatt and D. S. Fox, "The Application of Thermal Diffusivity Imaging to SIC-Fiber-Reinforced Silicon Nitride," Review of Progress in Quantitative Nondestructive Evaluation, ed. D. O. Thompson and D. E. Chimenti, vol. 12B, pp. 1305-1311 (1993).
19. M. Oksanen, A. Volcan, P. Fenici, and L. Fabbri, "Simulation on the Accuracy of Laser-Flash Data Analysis Methods," Review of Progress in Quantitative Nondestructive Evaluation, ed. D. O. Thompson and D. E. Chimenti, vol. 15A, Plenum Press, New York, pp. 549-552 (1996).
20. N. K. Del Grande, K. W. Dolan, P. F. Durbin and D. E. Perkins, "Emissivity-Corrected Infrared Method for Imaging Anomalous Structural Heat Flows," US Patent No. 5,444,241 (Aug. 22, 1995).
21. Xiaoyan Han, L. D. Favro, P. K. Kuo and R. L. Thomas, "Early-Time Pulse-Echo Thermal Wave Imaging", Review of Progress in Quantitative Nondestructive Evaluation, ed. D. O. Thompson and D. E. Chimenti, vol. 15A, Plenum Press, New York, pp. 519-524 (1996).
22. L. D. Favro, H. J. Jin, P. K. Kuo, R. L. Thomas, and Y. X. Wang, "Real Time Thermal Wave Tomography," Photoacoustic and Photothermal Phenomena III, Springer Series in Optical Sciences, vol. 69, ed. D. Bicanic, Springer-Verlag, Berlin, pp. 519- 521 (1992).
23. Vavilov, V. P. and X. Maidague, "Dynamic Thermal Tomography: A New Promise in the IR Thermography of Solids," Proceedings of SPIE Conference 1682, Thermosense XIV, ed. Jan K. Eklund, Orlando, FL, p. 194 (1992).
24. N. K. Del Grande, K.W. Dolan, P.F. Durbin, M.R. Gorvad, B.T. Kornblum, D. E. Perkins, D. J. Schneberk and A. B. Shapiro, "Three-Dimensional Dynamic Thermal Imaging of Structural Flaws by Dual-Band Infrared Computed Tomography," Proceedings of SPIE International Symposium on Aerospace and Remote Sensing, vol. 1942, Orlando, FL, (1993).
25. Vladimir P. Vavilov, Ermanno Grinzato, Paolo G. Bison, Sergio Marinetti, and Chiara Bressan, "Thermal Characterization and Tomography of Carbon Fiber Reinforced Plastics Using Individual Identification Technique," Materials Evaluation, vol. 54 no. 5, pp. 604-610 (May 1996).
26. John C. Russ, *The Image Processing Handbook*, CRC Press, Boca Raton (1992).
27. Rafael Gonzalez and Richard Woods, *Digital Image Processing*, Addison-Wesley Publishing Company, Reading MA (1993).
28. Anil Jain, *Fundamentals of Digital Image Processing*, Prentice Hall, Englewood Cliffs, NJ (1989).

29. Peters et al, United States Patent No. 5,563,962, "Two Dimensional Digital Hysteresis Filter for Smoothing Digital Images," (October 8, 1996).
30. Savitzky A., and Golay, M. J. E., *Analytical Chemistry,* vol. 36, pp. 1627-1639 (1964).
31. Parker, W. J., R. J. Jenkins, C. P. Butter, and G. L. Abbott, "Flash Method of Determining Thermal Diffusivity, Heat Capacity and Thermal Conductivity", J. Appl. Phys., vol. 32, p. 1679 (1961).
32. Clark, L. M. III and R. E. Taylor, "Radiation Loss in the Flash Method for Thermal Diffusivity", J. Appl. Phys., vol. 46, p. 714 (1975).
33. Taylor, R. E. and L. M. Clark, III, "Finite Pulse Time Effects in Flash Diffusivity Method", High Temperatures – High Pressures, vol. 6, p. 65 (1974).
34. Taylor, R. E. and J. A. Cape, "Finite Pulse-Time Effects in the Flash Diffusivity Technique", Appl. Phys. Lett., vol. 5, no. 10, p. 210 (1964).
35. Cowan, R. D., "Pulse Method of Measuring Thermal Diffusivity at High Temperatures", J. Appl. Phys., vol. 34, p. 926 (1963).
36. Cape, J. A. and G. W. Lehman, "Temperature and Finite Pulse-Time Effects in the Flash Method for Measuring Thermal Diffusivity", J. Appl. Phys., vol. 34, p. 1909 (1963).
37. Azumi, T. and Y. Takahashi, "Novel Finite Pulse-Width Correction in Flash Thermal Diffusivity Measurement", Rev. Sci. Instrum., vol. 52, no. 9, p. 1411 (1981).
38. Heckman, R. C., "Error Analysis of the Flash Thermal Diffusivity Technique", in Proceedings 14th International Thermal Conductivity Conference, Plenum Press, New York (1976).
39. Koski, J. A., "Improved Data Reduction Method for Laser Pulse Diffusivity Determination with the Use of Minicomputers", in Proceedings of the 8th Symposium on Thermophysical Properties, 2, The American Society of Mechanical Engineers, p. 94, New York (1981).
40. Degiovanni, A., "Correction de longueur d'impulsion pour la mesure de la diffusivity thermique par la methode flash", Int. J. Heat Mass Transfer, vol. 31, no. 3, p. 2199 (1988).
41. Zhong Ouyang, Li Wang, Feng Zhang, L.D. Favro, and R.L. Thomas, Proc. Eighth International Symposium on Nondestructive Characterization of Materials, June 15-20, 1997 Boulder, Colorado.
42. Nik Rajic, "Quantitative Examination of Corrosion Damage by Means of Thermal Response Measurements", NASA/TP-1998-208429 (June 1998).

APPENDIX A: ATAC THERMAL IMAGING ANALYSIS SOFTWARE

This appendix presents an overview of the capabilities contained in the comprehensive analysis software, *ATAC* (Automated Thermal Analysis Code), developed to automate the flaw detection using thermal wave imaging data. The main body of the software was written using Microsoft's Visual C^{++}. As such, it is an object-oriented software, which allows for easy maintenance of the program modules. In addition, the software contains modules written in Matlab® and incorporated into the C^{++} main code. These modules were incorporated via code translation in either of the following ways:

1) An executable program, resulting from compiling the original code written in Matlab® using the Matlab® compiler and associated libraries and using a C^{++} function to call an external program, or

2) Translating the original Matlab® functions using Mideva (a commercially available translator) and compiling the resulting C^{++} functions with the rest of the *ATAC* software.

The software is GUI (graphical user interface) driven to allow easy modification of the input parameters. Additionally, some of the modules are multithreaded to allow two or more of the software features to run in parallel. This lets the user look at results from one set of parameters while processing a separate data analysis with a different set of parameters.

A.1 The Main Menu Screen

This section describes the main menu screen of the *ATAC* software, shown in Figure A-1.

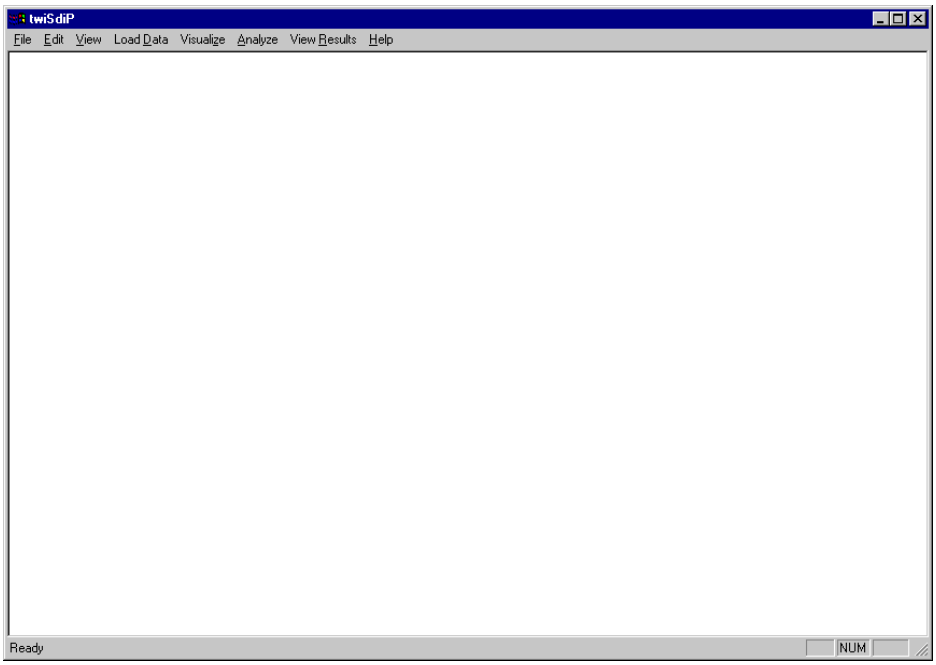

Figure A-1. ATAC Main Menu Window.

The main menu displays the basic Windows menus (**File**, **Edit**, **View, Minimize**, **Maximize,** and **Close** buttons) and the software specific menus (**Load Data**, **Visualize**, **Analyze, View Results** and **Help)**. The **File** menu has only two functions; Exit and Edit. The *Exit* function is available but none of the **Edit** menu functions are available at this time. The **View** menu displays or hides the status bar. The other software functions package will not run until a datacube is loaded (using the **Load Data** menu). If another function is selected before datacube is loaded, the message shown in Figure A-2 is displayed. Therefore, the first step in the analysis process is to use the **Load Data** menu to select the data to be analyzed.

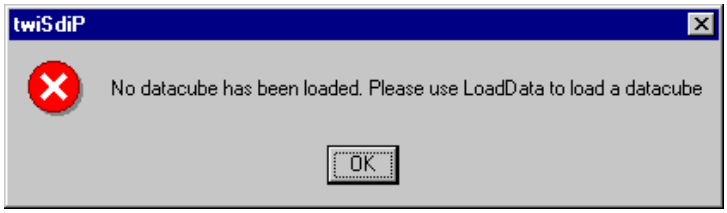

Figure A-2. Error message displayed if a function is selected before a datacube is loaded.

A.2 The Load Data Menu

This menu loads an uncompressed datacube from a file and makes it available to the rest of the software. The **Load Data** menu is shown in Figure A-3.

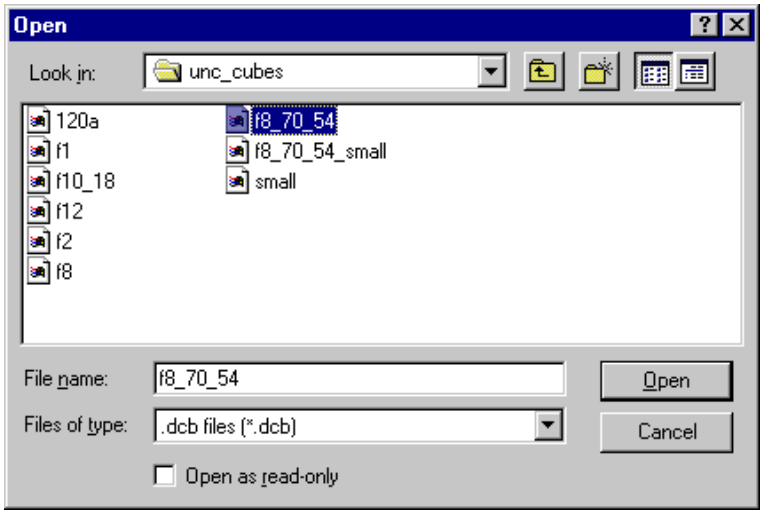

Figure A-3. Load Data menu.

This dialog box is an open-file menu. The software checks if the file is an uncompressed datacube and if it has the correct format. If the datacube is compressed, the message shown in A- 4 is displayed. If this occurs the datacube must be uncompressed using a utility found in the Thermal Wave Imaging, Inc. EchoTherm® 32 software.

Figure A-4. Datacube compression warning message.

Once a datacube has been successfully opened, the other software menus (with the exception of the **View Results** menu) become functional.

A.3 The Visualize Menu

The Visualize menu launches a GUI-driven 3D-visualization tool to aid in the analysis process. This module was written in Matlab®, compiled into an executable, and called from the main software as an external program on a separate thread from the main code. This lets the Visualizer run independently from the main code. Figure A-5 displays the Visualizer module window.

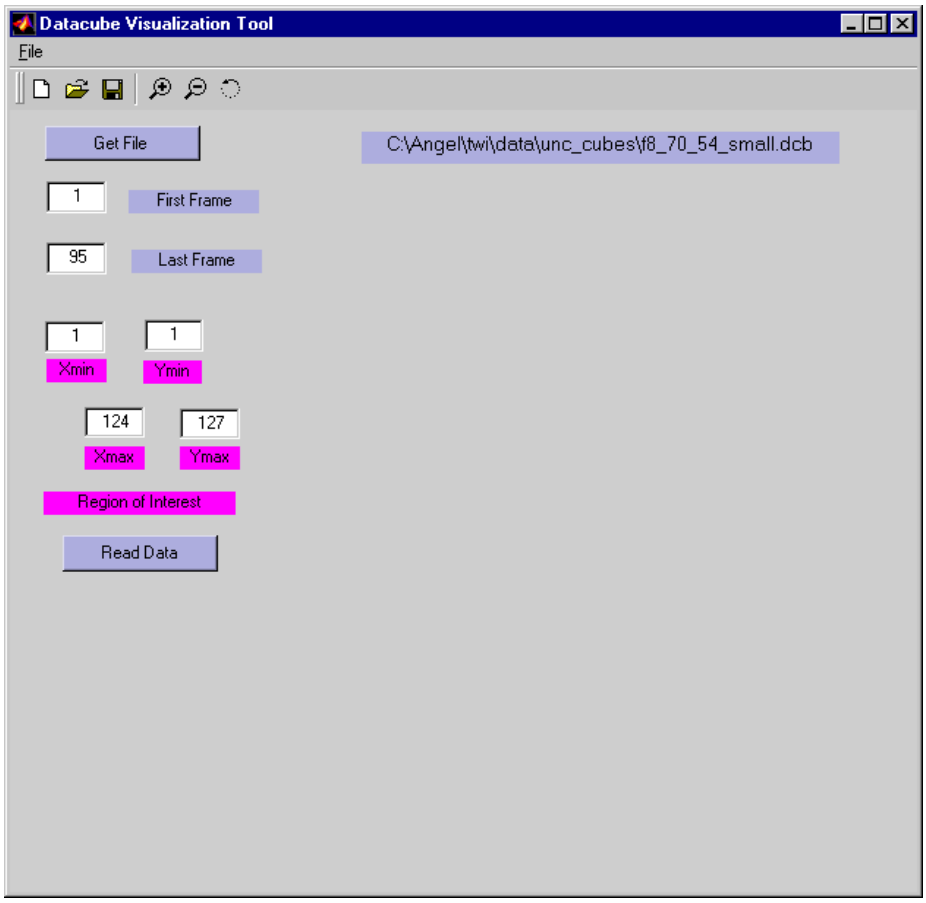

Figure A-5. Visualizer tool window.

The **Get File** button in the Visualizer window loads the datacube and read the inspection system parameters used in the data acquisition process. The user can then select the data spatial region and temporal layers to display. The data display is activated with the **Read Data** button. An example is displayed in Figure A-6.

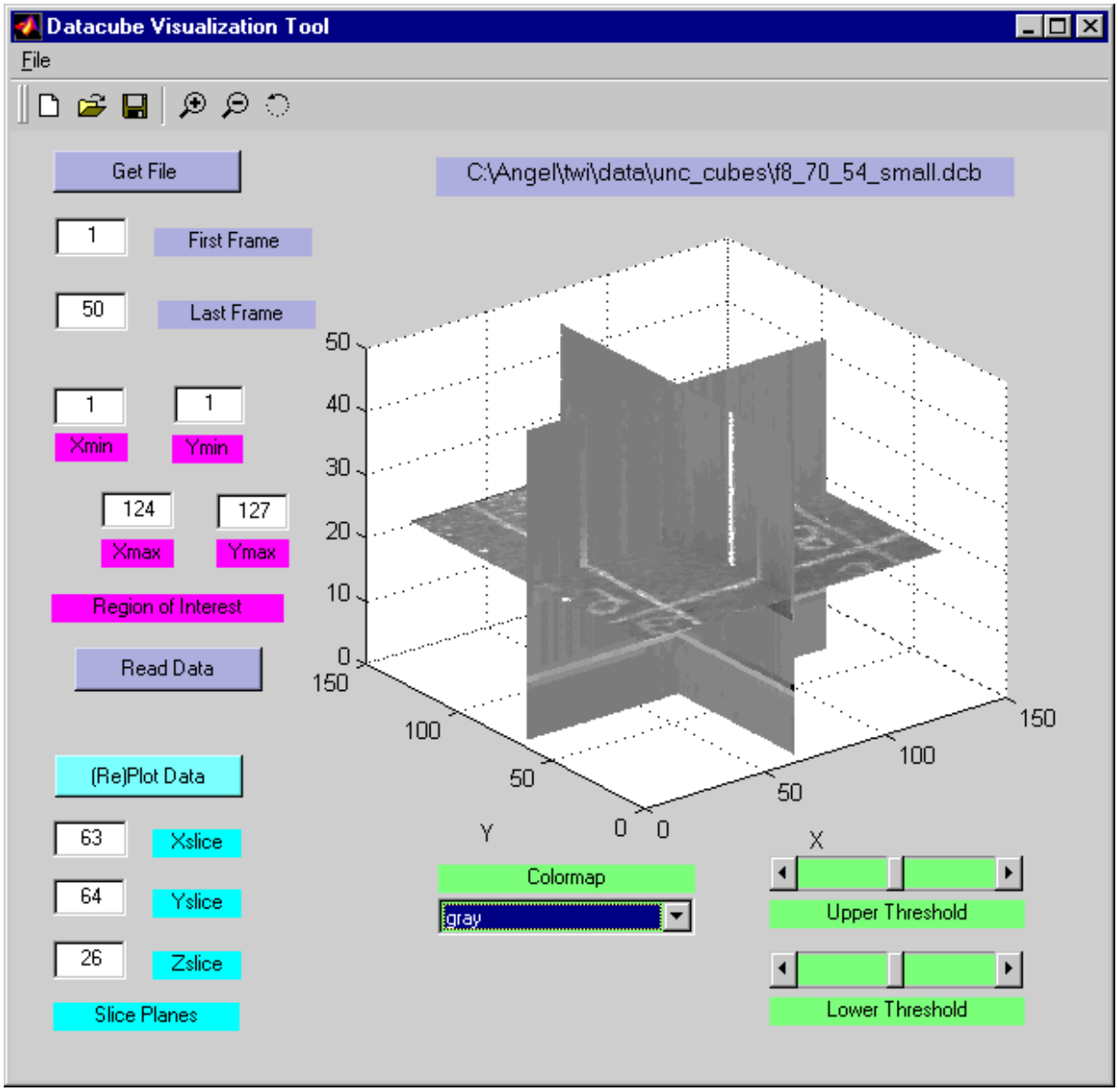

Figure A-6. Data visualization example.

The GUI tools let the user modify the **Colormap** and the **Lower** and **Upper thresholds** of the image intensity to enhance the image. Also, the user can reorient the 3-D display interactively. An additional feature provided by the visualization window is the slicing tool. This feature lets the user select specific X, Y, and Z planes to display as data slices. Figure A-6 is an example of a data slice display. As mentioned previously, this module runs on its own thread and therefore can be left active while other analysis operations are performed.

A.4 The Analyze Menu

This Analyze menu launches the primary software analysis. Figure A-7 displays the input parameter tab of the **Analyze** menu.

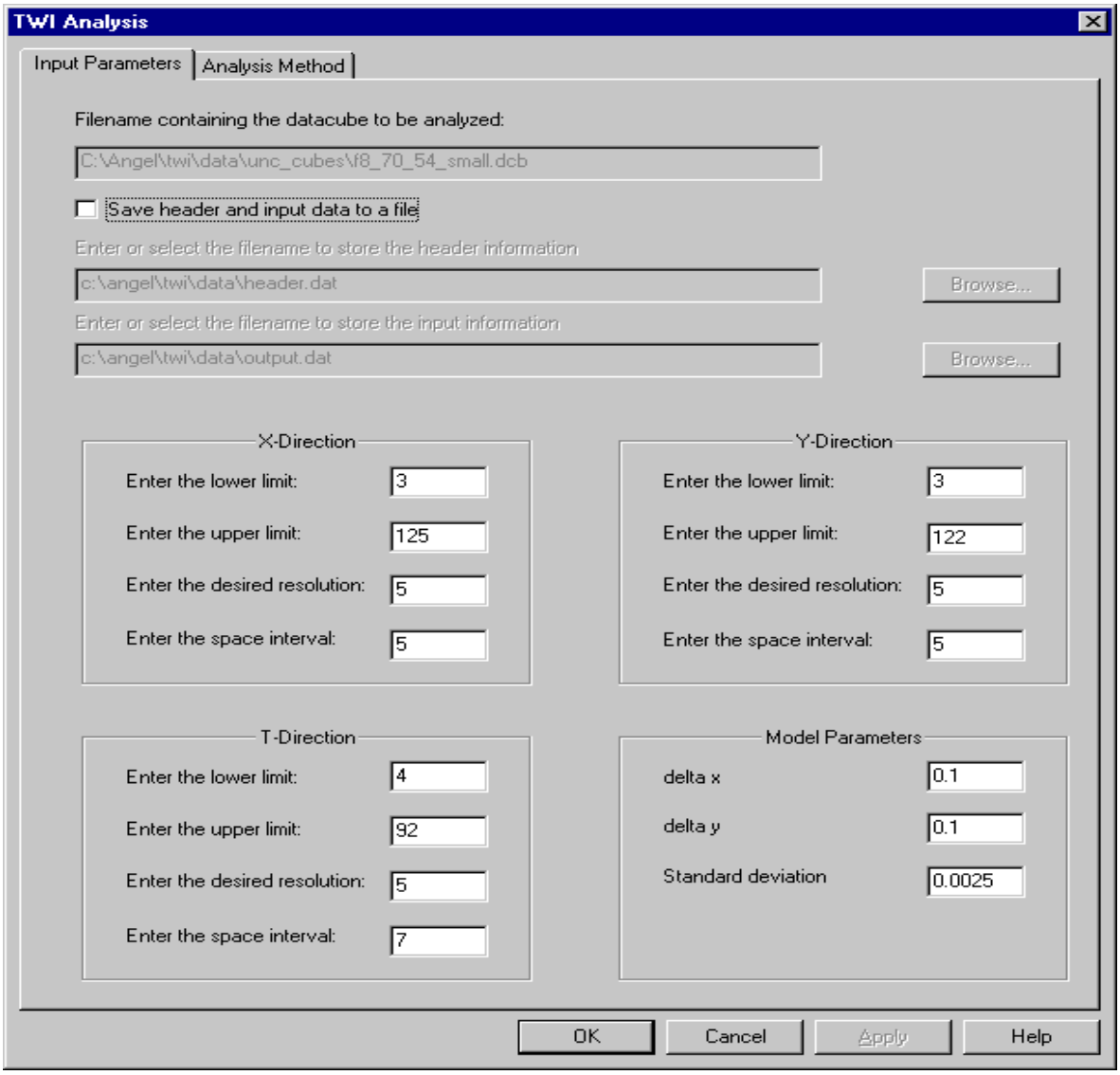

Figure A-7. Analyze Menu: Input Parameters Tab.

The first Analyze menu tab displays the analysis **Input Parameters**. These parameters define the analysis data region. All data within this region is smoothed using a nonlinear 18 parameter spatio-temporal polynomial model with temporal weighting. The following paragraphs describe each of the input parameters.

Filename containing the datacube to be analyzed: Shows the path and filename for the datacube that is will be analyzed (opened using the **Load Data** menu).

Save header and input data to a file: If the box is checked, the header information contained in the datacube will be stored in a file defined in the "*Enter or select the filename to store the header information*" box and the actual data will be stored in a text file defined in "*Enter or select the filename to store the input information*" box.

X-Direction Subwindow:

X-Direction: Defines the X-direction spatial analysis boundaries.

Enter the lower limit: Specifies the lower limit x coordinate that bounds the data analysis prism.

Enter the upper limit: Specifies the upper limit x coordinate that bounds the data analysis prism.

Enter the desired resolution: Specifies the size (in pixels) of the local analysis neighborhood window that surrounds each data point. For example, a value of 5 means that the data window used to fit the spatio-temporal smoothing polynomial for each data point has a width of 5 pixels (centered on the pixel of interest).

Enter the space interval: This parameter determines the spacing between analysis prisms. A value of one would analyze every data point within the defined image boundaries. A value of two would analyze every other data point. A value of three would evaluate every third data point.

Y-Direction Subwindow:

Y-Direction: Defines the Y-direction spatial analysis boundaries.

Enter the lower limit: Specifies the lower limit y coordinate that bounds the data analysis prism.

Enter the upper limit: Specifies the upper limit y coordinate that bounds the data analysis prism.

Enter the desired resolution: Specifies the size (in pixels) of the local analysis neighborhood window that surrounds each data point. For example, a value of 5 means that the data window used to fit the spatio-temporal smoothing polynomial for each data point has a length of 5 pixels (centered on the pixel of interest).

Enter the space interval: This parameter determines the spacing between analysis prisms. A value of one would analyze every data point within the defined image boundaries. A value of two would analyze every other data point. A value of three would evaluate every third data point.

T-Direction Subwindow:

T-Direction: Defines the temporal analysis boundaries. In other words, this specifies which image frames will be analyzed.

Enter the lower limit: Specifies the first image frame to be included in the data analysis prism.

Enter the upper limit: Specifies the last image frame to be included in the data analysis prism.

Enter the desired resolution: Specifies the size (in number of image frames) of the local analysis neighborhood window that surrounds each data point. For example, a value of 5 means that the data window used to fit the spatio-temporal smoothing polynomial for each data point has a length of 5 frames (centered on the frame of interest).

Enter the space interval: This parameter determines the spacing between analysis prisms. A value of one would analyze every image frame within the defined image boundaries. A value of two would analyze every other image frame. A value of three would evaluate every third image frame.

Model Parameters Subwindow:

Delta x: Defines the spatial increment between points along x-axis.

Delta y: Defines the spatial increment between points along y-axis.

Standard deviation: Defines the width parameter for the radial basis function (in time units).

Error messages will indicate when the parameters are not appropriate for the selected datacube.

The second analysis window tab, **Analysis Type**, displays the standard analysis options that can be applied to the datacube. Figure A-8 displays this window.

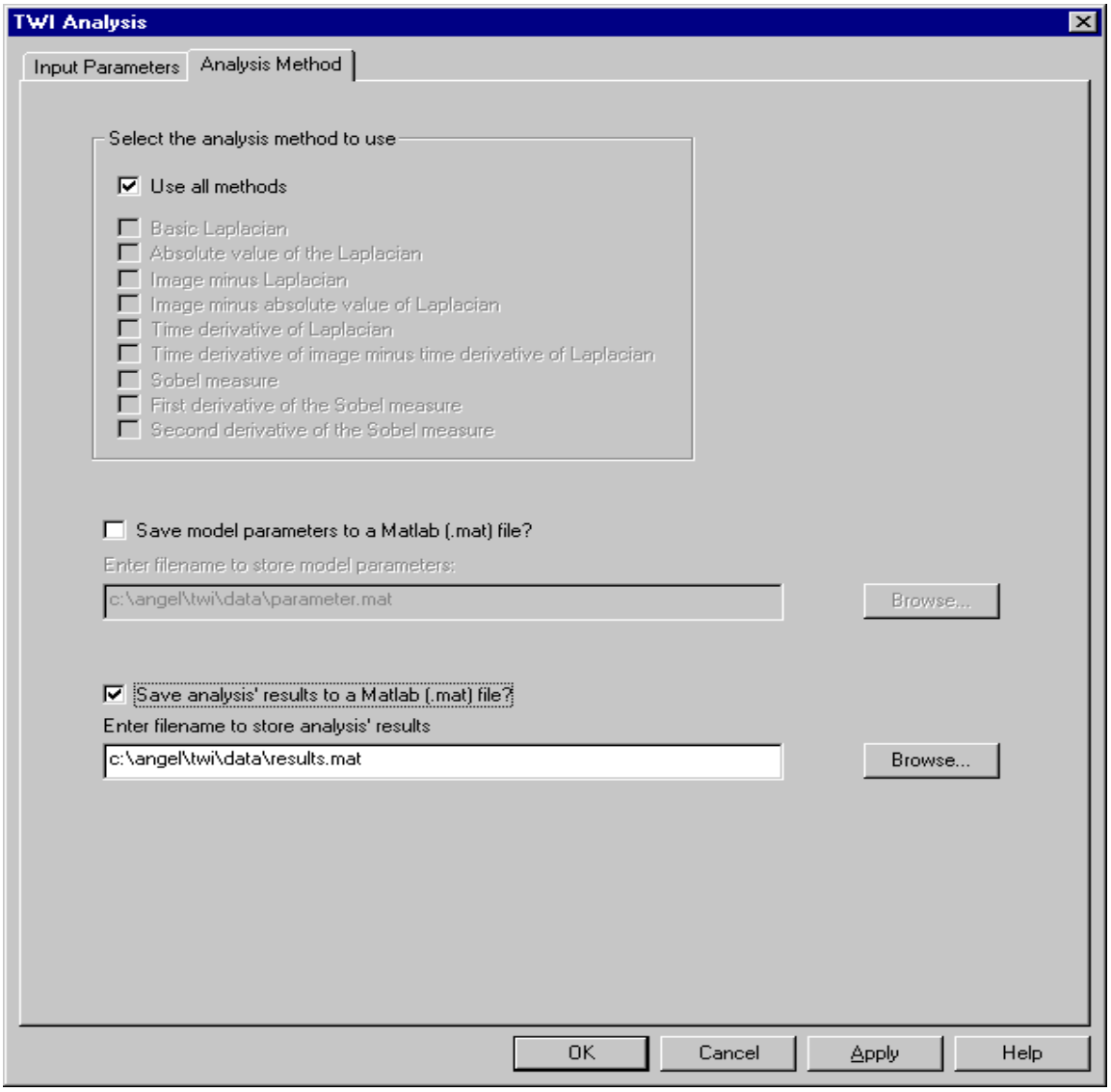

Figure A-8. Analyze Menu: Analysis Method Tab.

The basic analysis methods provided in the software are briefly described below:

Basic Laplacian: Calculates the image Laplacian.

Absolute Value of the Laplacian: Calculates the Absolute Value of the image Laplacian.

Time Derivative of the Laplacian: Calculates the temporal derivative of the image Laplacian.

Time derivative of image minus time derivative of Laplacian: Calculates the difference between the temporal derivative of the original image and the temporal derivative of the image Laplacian.

Image minus Laplacian: Calculates the difference between the original image and the image Laplacian.

Image minus absolute value of the Laplacian: Calculates the difference between the original image and the absolute value of the image Laplacian.

Sobel Measure: Calculates the Sobel measure for the image data.

First derivative of the Sobel measure: Calculates the first time derivative of the Sobel measure for the image data.

Second derivative of the Sobel measure: Calculates the second time derivative of the Sobel measure for the image data.

In addition to these basic image analysis metrics, the ATAC software has added the metrics presented in section 4.3.1.

The two check boxes in the lower portion of the Analysis Method window let the user save the computed model parameters and the analysis results to a specified file. The analysis results must be saved to use the **View Results** menu display features. The files saved by these checkboxes are .MAT files (Matlab® type files).

The progress of the analysis operation is displayed in an Analysis status window as shown in Figure A-9. When the analysis is complete, pressing the **OK** button returns the user to the analysis window. The user may then press **OK** or **Cancel** in the **Analysis Menu** to return to the main window.

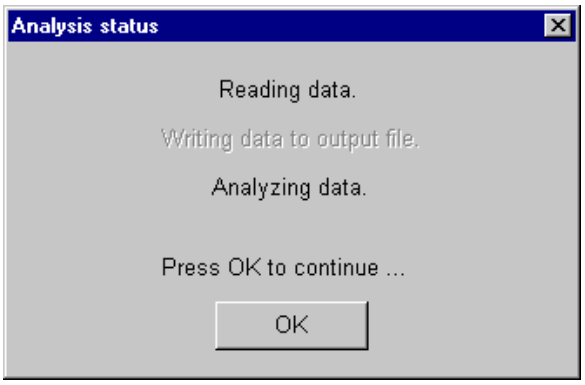

Figure A-9. Analysis status window.

A.5 The View Results Menu

After the image data analysis is complete the View Results menu can be used to visually display the processed results. If this menu is accessed before an analysis has been performed, the error message shown in Figure A-10 is displayed.

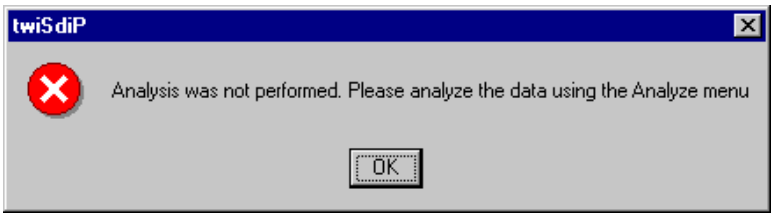

Figure A-10. Warning message when no data is available for display.

If an analysis was successfully performed and the analysis results are saved to a file, the view results tool shown in Figure A-11 is displayed. This is another Matlab® GUI program compiled into an executable and called as a separate thread from the main software. Since this program operates as a separate thread it can run independent from the main software. The display the processed results, the user must first use the **Open file** button to load the saved analysis results file. After the analysis data is loaded the user can select an analysis type from the scroll window. If the selected data analysis metric processed the image frames independently the results for individual frames can be selected using the frame slider tool. Once a frame and the analysis type are selected, the information is displayed by pushing the **Plot** button. As shown in figure A-11, the display provides a contour plot of the values of the desired measure with a colorbar that provides the metric values for each of the displayed colors. Alternately, if one of the metrics from section 4.3.1 is selected, a composite image result is displayed.

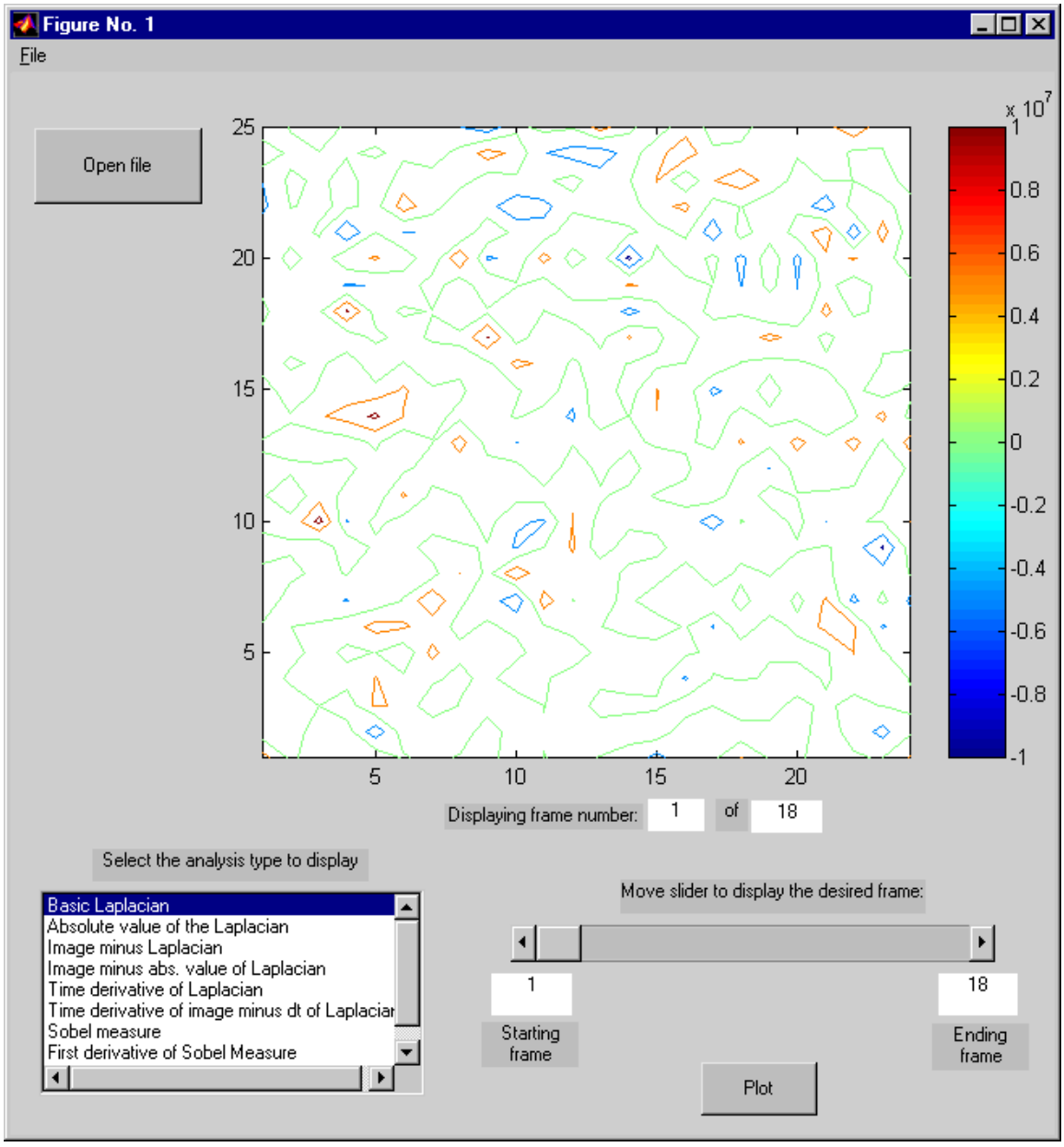

Figure A-11. View Results menu window with sample results.

DISTRIBUTION:

1 MS-0188 D. L. Chavez, 1030
1 MS-0453 H. Abeyta, 2101
1 MS-0482 R. Paulsen, 2109
1 MS-0555 M. Garrett, 9122
2 MS-0555 B. Hansche, 9122
5 MS-0555 M. Valley, 9122
1 MS-0557 T. Baca, 9125
1 MS-0615 R. Perry, 6252
2 MS-0615 D. Ashbaugh, 62521
1 MS-0633 G. Mayes, 2952
1 MS-0634 R. Hahn, 2951
1 MS-0824 J. Moya, 9130
1 MS-0824 A. Ratzel, 9110
1 MS-0825 W. Rutledge, 9115
1 MS-0826 W. Hermina, 9113
1 MS-0827 J. Zepper, 9143
1 MS-0828 M. Pilch, 9133
1 MS-0828 B. Blackwell, 9133
1 MS-0828 B. Oberkampf, 9133
2 MS-0828 T. Paez, 9133
2 MS-0828 A. Urbina, 9133
1 MS-0834 J. Johannes, 9114
1 MS-0834 M. Prairie, 9112
1 MS-0834 S. Beresh, 9112
1 MS-0834 S. Kearney, 9112
1 MS-0834 T. O'Hern, 9112
1 MS-0834 W. Trott, 9112
1 MS-0834 L. Mondy, 9112
1 MS-0835 J. M. M^{c}Glaun, 9140
1 MS-0835 S. Kempka, 9141
1 MS-0835 J. Peery, 9142
1 MS-0836 E. Hertel, 9116
1 MS-0836 B. Bainbridge, 9116
1 MS-0836 D. Dobranich, 9116
1 MS-0836 R. Hogan, 9116
1 MS-0836 C. Romero, 9116
1 MS-0836 R. Griffith, 9117
1 MS-0841 T. Bickel, 9100
1 MS-0847 H. Morgan, 9120
1 MS-0847 T. Carne, 9124
1 MS-0847 C. Nelson, 9124
1 MS-0847 J. Redmond, 9124
1 MS-0847 R. May, 9126
1 MS-0847 S. Burchett, 9126
1 MS-0847 J. Jung, 9126
1 MS-0847 R. Reese, 9126
1 MS-0886 N. Jackson, 1812
1 MS-0886 R. Goehner, 1822
1 MS-0889 M. F. Smith, 1833
1 MS-0893 R. Brannon, 9123
1 MS-1135 L. Gritzo, 9132
1 MS-1135 W. Gill, 9132
1 MS-1135 J. Nakos, 9132
1 MS-1135 J. Suo-Anttila, 9132
1 MS-1135 S. Tieszen, 9132
1 MS-1135 S. Heffelfinger, 9134
1 MS-1135 J. Cherry, 9134
1 MS-1135 N. Davie, 9134
1 MS-1135 M. Nissen, 9134
1 MS-1172 G. Hochrein, 15413
1 MS-1183 E. Schindwolf, 15425
1 MS-1185 E. Reece, 15401
1 MS-9042 M. Horstemeyer, 8728
1 MS-9401 J. Garcia, 8725
1 MS-9402 K. Wilson, 8724
1 MS-9951 D. Lindner, 8101
1 MS-9018 Central Technical Files, 8945-1
2 MS-0899 Technical Library, 4916
1 MS-0612 Review and Approval Desk, 9612 for DOE/OSTI